DEFORMATION MAPPING OF FIBRONECTIN FIBRILS USING DIGITAL IMAGE CORRELATION

A THESIS IN
Electrical Engineering

Presented to the Faculty of the University
of Missouri-Kansas City in partial fulfillment of
the requirements for the degree

MASTER OF SCIENCE

by
ADITYA ROSHAN

Bachelor of Technology, 2008

Kansas City, Missouri
2011

DEFORMATION MAPPING OF FIBRONECTIN FIBRILS USING

DIGITAL IMAGE CORRELATION

Aditya Roshan, Candidate for the Master of Science degree,

University of Missouri-Kansas City, 2011

ABSTRACT

Bone cells produce large amounts of extracellular matrix (ECM) proteins that form a fibrillar scaffold on which bone mineral is deposited. Prior work has shown that fibronectin fibrils are one of the earliest ECM proteins to be assembled. Time lapse imaging techniques show that the deposition of fibronectin by osteoblasts is a highly dynamic process, in which the forming fibronectin fibril network is continually stretched, contracted and moved via the activity of motile cells.

This study has developed an automated Digital Image Correlation based technique for determining the displacements and strains experienced by the fibrils during the assembly process. Fibril motion is tracked using a time lapse sequence of images and the motion kinematics are determined using an image cross-correlation method. The method is implemented in Matlab and compared to manual calculations. Furthermore, we have studied the motion of a set of 20 fibrils in order to predict fibril kinematics.

The faculty listed below, appointed by the Dean of the School of Computing and Engineering, have examined the thesis titled "Deformation Mapping of Fibronectin Fibrils Using Digital Image Correlation", presented by Aditya Roshan, candidate for the Master of Science degree, and hereby certify that in their opinion it is worthy of acceptance.

Supervisory Committee

Ganesh Thiagarajan, Ph.D., Committee Chair
Department of Civil and Mechanical Engineering

Sarah L Dallas, Ph.D.
Department of Oral Biology

Mark L Johnson, Ph.D.
Department of Oral Biology

Walter Daniel Leon-Salas, Ph.D.
Department of Computer Science and Electrical Engineering

CONTENTS

TABLES

Table Page

ILLUSTRATIONS

Figure Page

ACKNOWLEDGEMENTS

I would like to thank my thesis committee chair and main advisor for this research, Dr.Ganesh Thiagarajan, committee member and the main source of funding for this research, Dr.Sarah Dallas and committee member Dr.Mark Johnson for their constant support, guidance and encouragement that provided the motivation to bring this work to its conclusion. I would also like to thank my committee member, Dr.Walter Leon-Salas, for his valuable suggestions and his push to constantly improve the work.

I would wish to express my gratitude towards Maitree Banerjee who first worked on this project and introduced me to this research. I would also wish to thank Melony Chakrabarty for all her help, input and encouragement at various stages of the project and Anusha Mannava for offering support and guidance every time I needed it.

Lastly I would wish to thank all my family members and friends who have been a constant source of support through this entire research. Their faith and belief in me helped take this research to a level I would not have otherwise achieved.

CHAPTER 1

INTRODUCTION

The extracellular matrix (ECM) in bone serves as a scaffold to support cells and tissue and is composed primarily of the fibrillar extracellular matrix protein, type I collagen, as well as many non-collagenous proteins, which together form a scaffold onto which the mineral component of bone is deposited. Of the non-collagenous proteins, fibronectin is a critical component, as it is one of the earliest ECM proteins to be assembled and has been shown to be required for assembly of other ECM proteins, including type I collagen (McDonald *et al.,* 1982). Growth factors can also be stored in the ECM and can have potent effects on cell function, thereby regulating the pattern, morphology and growth of cells into tissues. Our understanding of extracellular matrix (ECM) has therefore expanded from what was a simple static structural framework to an intricate and dynamic system for signaling, movement, and growth (reviewed in Dallas *et al.,* 2006 and Sivakumar *et al*., 2006).

Previous work has shown that fibronectin plays a key role in facilitating the deposition of several bone ECM components into the matrix (Velling *et al.,* 2005; Sottile and Hocking, 2002; Periera *et al.,* 2002). Therefore, understanding how fibronectin fibrils are assembled by osteoblasts is important to understanding how bone ECM is formed. To better understand the function of fibronectin, it is imperative to analyze the physical and functional aspects of ECM (Pereira, Rybarczyk, Odrljin, Hocking, Sottile, & Simpson-Haidaris, 2002). The ECM is a storage site for growth factors such as transforming growth factor-beta (TGF-β) (Dallas et al., 1995; Oreffo et al., 1989; Seyedin et al., 1986; Taipale et al., 1994) and fibroblast growth factors (reviewed in Taipale and Keski‐Oja, 1997) and provides an

environment for the release of these growth factors, consequently regulating their availability and function. Secondly, the ECM provides an integral mode of communication between the extracellular and intracellular environments. A key component to regulate these cell-matrix interactions is integrins. They are a family of transmembrane proteins that act as cell surface receptors for different ECM proteins (Peltonen, et al., 1989). Components of the ECM bind to these cell surface integrins, which subsequently activate the actin cytoskeleton, initiating a cascade of events that enables signals to travel within the cell. Lastly, the ECM's structural organization provides unique physical and mechanical properties for individual tissues. The dynamic components and structure of ECM also provides the flexibility for tissues to grow or adapt to various external stimuli.

Bone is a highly specialized ECM because it is mineralized. The mineral consists of calcium phosphate (in the form of hydroxyapatite). Of the organic component of bone, approximately 90% is type I collagen, with the other 10% made up of non-collagenous proteins, including fibronectin. Previous work has shown that fibronectin plays a key role in controlling the assembly of other ECM proteins such as collagen types I and III, latent transforming growth factor beta binding protein-1 (LTBP1), fibrillin and the proteoglycans, decorin and biglycan (Dallas *et al*., 2005). Fibronectin is required not only to initiate ECM formation, but it also is continually required to maintain the stability of the matrix (Sottile and Hocking, 2002).

Thus, to better understand construction of the bone matrix, it is important to understand how fibronectin itself is assembled into the ECM. Fibronectin is a large extracellular glycoprotein that is composed of disulfide linked dimers. The dimeric fibronectin is secreted as a globular protein that does not spontaneously assemble into

polymeric fibrils. The assembly is controlled at the cell surface (Pankov et al., 2000). Fibronectin first binds to the cell surface via interactions with cell surface integrins (predominantly a5b1 in the case of fibronectin). This binding to the cell surface integrin ($\alpha 5\beta 1$) then activates the intracellular actin cytoskeleton and generates a mechanical force. This mechanical force stretches fibronectin and further exposes sites of self-association that allows fibronectin dimers to interact with one other and aggregate to form fibrils. These fibronectin fibril networks are integral to maintain communications between cells and ECM components, in order to form a dynamic and adaptive tissue.

Considerable research has been done in developing methodologies to study and analyze the structure and function of mineralized tissue. Most of what is currently known has come from the use of static imaging approaches, such as light or electron microscopy in combination with chemical and bio-chemical analysis and more recently molecular approaches such as overexpression, deletion or mutation of genes thought to regulate bone cell function However, due to their dynamic nature, researching certain events, such as bone formation, re-modeling and fracture healing, requires observing the tissue over a period of time. In such cases the use of static imaging techniques has limitations and approaches such as live-cell imaging, in which the behavior of cells and tissues are studied over a period of time, can provide additional insight into the dynamics processes that control these events (Sivakumar *et al*., 2006 and reviewed in Dallas *et al*., 2006).

Live-cell imaging has proven effective in studying the morphogenetic processes during embryonic development (Czirok *et al.*, 2004; Czirok *et al.*, 2002; Jones *et al.*, 2005; Sakai, 2003 and reviewed in Dallas *et al.,* 2006) along with providing vital information about various other cellular processes (Eils and Athale, 2003 and .reviewed in

Dallas *et al.,* 2006*)*. Extensive research has lead to the development of a variety of pH-sensitive dyes and recombinant fluorescent proteins that can be used to label almost any intra-cellular or extra-cellular protein or structure. Once labeled, these structures can then be observed using powerful imaging techniques like FRET (fluorescent resonance energy transfer), FRAP (fluorescence recovery after photo bleaching) and laser confocal microscopy. These observations have led to a deeper understanding of the cells and sub-cellar components. Research continues in the field of live-cell imaging yielding better techniques, which can be used to gather more information about the behavior and characteristics of mineralized tissues.

Analysis using live-cell imaging techniques has provided vital biochemical, biophysical, spatio-temporal and kinetic information on cells, sub-cellular components and proteins. This type of live cell imaging analysis was extended into studying the kinetics of assembly of ECM in cell cultures and developing embryos. As a result it was observed (Sivakumar *et al*., 2006; Ohashi et al., 1999; Petroll et al., 2004; Petroll and Ma, 2003; Petroll et al., 2003; Kozel et al., 2006; Czirok et al., 2006) that the components of ECM were highly elastic and constantly in motion due the underlying cellular motion.

Upon further research (Sivakumar *et al*., 2006) it was observed that the cells actively participate in the fibril assembly and that they are also capable of reorganizing the ECM by shunting the fibrillar material from one location to the other. Analyzing these cell motions and the forces exerted by the cells on the extracellular matrix fibrils during matrix assembly and reorganization would provide further insight into the cellular and biophysical mechanisms by which the ECM is assembled. The study performed in this research project is

aimed at developing a method for the analysis of fibril motion by using computational approaches such as image processing and digital image correlation.

The ability to recognize features, colors, shapes, faces or any desirable attribute within the image is a functionality that is very much in demand and has myriad possible applications. The study of how cells, nuclei, intracellular organelles and extracellular components, such as ECM proteins move and react to various conditions and stimuli can be enhanced by applying image processing techniques to time lapse image stacks. This approach enables quantitation of the underlying biology and measurement of the magnitude of effect of various stimuli. This also provides a basis for the development of computer models and simulations, based on empirical data that can be used to make predictions about the effects of untested stimuli and other manipulations.

Many different methodologies for processing of images have been developed by different researchers. Digital image Correlation (DIC) is one such method that has proven to be very effective in applications associated with the calculation of various kinematic measures. Many models of calculation have been developed using the concept of DIC over the years. A few of them are listed below.

A method has been developed by (Zamir, Czirók, Rongish, & Little, 2005) to measure the deformation mappings observed in tissue material points in various layers of the avian embryo and subsequently calculate the strain maps. These investigators have developed their method using well established concepts of Particle Image Velocimetry (PIV), which is a digital image correlation technique best used in cases where deformations or flow patterns need to be measured. As a part of their analysis, they have also used this method to study the

dynamic motions of ECM during the early stage of vertebral development in chick embryos. Their application of PIV to study ECM was very useful in the development of this study.

Another such method has been developed by KC Kim et al (Kim, Yoon, Kim, Chun, & Lee, 2006) to study the three-dimensional topology of the turbulence velocity field by using the concepts of PIV. They developed PIV based algorithms to detect certain features of some specific vortices. While this was developed for a non-biological application, the aim of this study was to calculate the kinematics of the velocity field.

H.Lu and P.D.Cary (Lu & Cary, 2000) have introduced a method to refine the Digital Image Correlation method by using second order approximations of displacement gradients. These approximations are useful in measurements where large deformations, which are unaccounted for by first order gradients, are present. This method was tested and validated on a non-biological system, but the method discusses a new way of tracking smaller displacements that are difficult to track with the first order approximations.

Bruck et al (Bruck, McNeill, Suttons, & Peters, 1989) have, in the field of mechanics, discussed the drawbacks of the current usage of the coarse-fine search method used by DIC and have proposed a new method to calculate the displacement gradients. This new method uses the concept of Newton – Raphson method of partial correction to calculate the displacement gradients accurately while utilizing lesser processor time than the coarse-fine search method.

These are just a few of the many other methodologies that have been developed. Each of these methods is suitable to a specific category of images based on their resolution, format, quality and the type of attribute being studied.

This research is an attempt to develop one such image processing application that can be used to calculate the displacement vectors and strains being experienced by fibronectin fibrils during their assembly by osteoblasts. The image processing method has been applied to image stacks generated from time lapse imaging of fibronectin assembly in living osteoblast cultures. A fluorescent probe was used to monitor the assembly of fibronectin and a series of consecutive images were taken at 15-20 minute intervals in fluorescence mode (to visualize the fibronectin fibrils) and in differential interference contrast mode (to visualize the cells). The algorithm uses the concept of two-dimensional Digital Image Correlation (2D DIC), which involves identifying the geometrical location of the fibril feature from the previous images and applying this data to a mathematical, normalized cross correlation formula to identify the position of the same feature in the current image. All of this data obtained is then used to calculate the displacement and strain vectors between successive image frames and as a function of time. The key advantages of this open source application are (i) Ease of usage, (ii) Mathematical precision, (iii) Ease of modification.

The computer program for this application was developed in Matlab and the results obtained were then compared to the data generated from the DIC application with data calculated from manual positioning of markers on the fibril features to determine the displacement vectors.

The remainder of this chapter describes the biology based computational objectives, a brief description of the experimental procedure from which the images are extracted (the experiments themselves were not performed as a part of the thesis) and the preprocessing procedure adopted for the images. Chapter 2 explains in more detail the algorithm used for the DIC correlation analysis and Chapter 3 reports the results of the testing and discusses

various observations based on these results. Based on the process developed, a set of twenty fibrils from the images have been analyzed and the kinematic characteristics of the fibril motion have been quantified. Chapter 4 discusses proposed future work and conclusions of the study.

1.1 Biological Significance and Rationale for the Study:

The project was developed for potential applications where features and motions of cells and subcellular or extracellular components captured during live imaging experiments are challenging to quantify manually, because of the large datasets and large number of images generated. In these experiments, a series of images (e.g. fifty or more images) containing features of interest such as cell, organelle and ECM protein etc., are captured at specified time intervals from multiple imaging fields over a defined period of time and used for evaluation later on. The specific requirement for which this project was developed is described below.

Previous studies (Czirok et al., 2004, 2005; Filla et al., 2004; Kozel et al., 2006; Ohashi et al., 1999, 2002; Sivakumar et al., 2006; Zamir et al., 2005) examining the dynamic process of fibronectin assembly in primary osteoblasts (osteoblasts isolated directly from mouse bone tissues and cultured) or in osteoblastic cell lines, such as the 2T3 mouse osteoblast cell line (Ghosh-Choudhury et al .,1996) have shown that the assembly of fibronectin is a highly dynamic process that appears to be driven by cell motility. Fibronectin first assembles on the cell surface in small fibrillar patches and larger fibrils appear to be built by cells pooling their surface assembled fibronectin to form increasingly larger fibrils

(see figure 1.1). The fibrils are continually stretched and contracted during the assembly process as a result of the cell motion.

The duration of the imaging experiment can be as long as 48 hours and the resulting time lapse movies (taken at twenty minute intervals) can depict fibronectin assembly from an essentially zero baseline to the formation of a well-organized fibril network. Therefore, there is considerable change represented throughout the imaging period.

Quantitation of the fibril motions and strains is therefore challenging as new fibrils and cells can be formed during the imaging period, particularly early on in the assembly process. The cells are constantly in motion and this in-turn causes the fibrils to move. Since the fibrils are largely interconnected at their ends, any motion along their body would exert an equivalent amount of strain on it. The only way to calculate these strains is to determine the lengths of the fibrils at regular intervals of time and to compare it with the previous lengths, hence giving an estimate of the displacement undergone which can be used to obtain the strains**.**

1.1.1 Experimental Process:

As stated earlier, the imaging experiments to analyze the dynamic process by which fibronectin fibrils are formed in osteoblasts were performed by researchers in the Dallas Lab prior to the work described in this study. The current study used image stacks generated from these prior experiments as the data source for developing the DIC analysis methods. The imaging experiments were performed using 2T3 osteoblast-like cells, which is a clonal osteoblast cell line. This cell line was obtained from osteoblasts isolated from transgenic mice expressing the immortalizing SV40 T-antigen under control of the bone morphogenetic

protein-2 (BMP2) promoter. The 2T3 cell line is a good substitute for primary osteoblasts because of its similarity to primary osteoblasts, its production of a bone-like ECM and due to the fact that it mineralizes in culture.

To monitor the assembly of fibronectin, a fluorescence-labeled purified fibronectin probe was used that was prepared using an Alexa 555 protein labeling kit from Molecular Probes (Invitrogen Corporation, Carlsbad, CA). This kit was used to attach an alexa555 Alexa 555 (red fluorescent) tag onto purified fibronectin isolated from human plasma. For live imaging of fibronectin assembly in 2T3 osteoblast cells, the cells were plated into glass coverslip bottomed 2-well lab-tek chamber slides (Nalge Nunc, Rochester NY) at a density of 2 x 104 cells/cm2 in culture media consisting of α-Minimal Essential Medium (a-MEM) supplemented with 10% Fetal Bovine Serum, 2 mM L-glutamine and 100U/ml penicillin/streptomycin. After the cells were allowed to adhere overnight, Alexa 555-labeled fibronectin (5ug/ml) and unlabeled fibronectin (5ug/ml) were added in a thin agarose layer (300ul of 0.5% agarose per well), and allowed to set. Then 2ml of fresh a-MEM with supplements as described above plus 10ug/ml unlabeled plasma fibronectin was added. The slide was placed onto the microscope stage for one hour for equilibration prior to imaging.

Time lapse imaging was performed using a Nikon TE 2000E microscope equipped with widefield epifluorescence and differential interference contrast illumination. The temperature was maintained at 37°C using the "Cube & Box" Temperature Control System from Life Imaging Services, (Reinach, Switzerland), in conjunction with a custom plexiglass incubation chamber that enclosed the microscope and specimen stage. A humidified 5% CO2 atmosphere was maintained using an automated gas mixer system ("The Brick" Life Imaging Services, Reinach, Switzerland). The microscope system is fully automated, with a

precision motorized x, y and z stage. The microscope hardware, image acquisition, processing and analysis were controlled by the "Metamorph" software (Universal Imaging Corporation, PA). Z-stack images were acquired for each time point under 20X magnification in fluorescence mode and also under differential interference contrast illumination. The images were acquired using a Roper Scientific Coolsnap HQ cooled CCD camera with 12-bit grey scale resolution. Fields of 448 x 335mm were imaged at a spatial resolution of 696 x 520 pixels (2x2 binned mode) every 20 minutes for 48 hours from 5 optical planes (1.5um separation between planes). Image stacks were processed in Metamorph using the "best focus" or Z-projection algorithms and exported as 8 bit image stack (.stk) files.

When acquiring images from multiple imaging fields, the motorized stage on which the specimen is mounted moves to bring the appropriate imaging field into the camera field of view. While this provides the user the freedom to choose more data fields to process, it also introduces rigid body motion (analogous to "camera shake") into the image stacks, which means that the boundaries of the image do not necessarily remain constant through all the images but may vary slightly from image to image. This introduces false motion into the cells and thus needs to be corrected. This was done using an open-source software called Image J using the "stackreg" plugin, which registers/aligns the stack of image slices to correct for rigid body motion [Thevenaz et al., 1998]. As a result of this processing step, cropping of the edges of the registered movie and reducing the image size, the resolution of the images changed from 520x696 to 296x396 pixels. To better observe and analyze the fibronectin fibril images, they were subjected to brightness and contrast adjustments. These corrected image stacks provided the input data for the current studies to develop methods to

determine the displacements and changes in lengths of fibrils, which can be used to calculate the strains acting on them.

Since there was a considerable amount of change throughout the entire movie, which goes from essentially no fibrils at the beginning of the movie to a well formed fibronectin fibril network by 48 hours (see figure 1.1), it was decided to divide the image stack into 4 segments of 12 hours each, based on the rate of formation of new fibrils. This means that the first segment representing the first 12 hours of the experiment would have the highest rate of formation of fibrils with new features and fibrils forming in almost every image and would be the most challenging to analyze using automated methods. The next segment consisting of images taken during hours 12-24 has a lower rate of formation of new fibrils. The third segment has an even lower rate of formation of new fibrils with continued fibril motion while the rate of formation of new fibrils in the last segment is virtually zero but there is still fibril motion. Since the interval between two consecutive images is 20 minutes, the experiment ranging over a period of 48 hours would give a total 144 images with each segment containing 36 images each. Figure 1.1 shows a set of images taken at 0h, 6h and 12h and thereafter every 12 hours of the experiment. Note that the number, density, lengths and interconnectivity of the fibrils increases rapidly from hours 0 to 24, after which there is less change in the patterning of the fibrillar network. This means that in the early stages of the experiment many new fibrils and interconnections are formed as compared to the later stages.

Since in the initial hours of the experiment the fibrils are still in the process of being formed, only images 108 to 144 (the last 12 hours of the experiment), where the fibrils are well developed, was used for the initial analysis. However, once the technique demonstrated an effective tracking ability and the results from this analysis was compared to the results

from a manual analysis, similar quantitative analyses were performed on the images 73 to 108 (representing the period from 24 to 36h) as well.

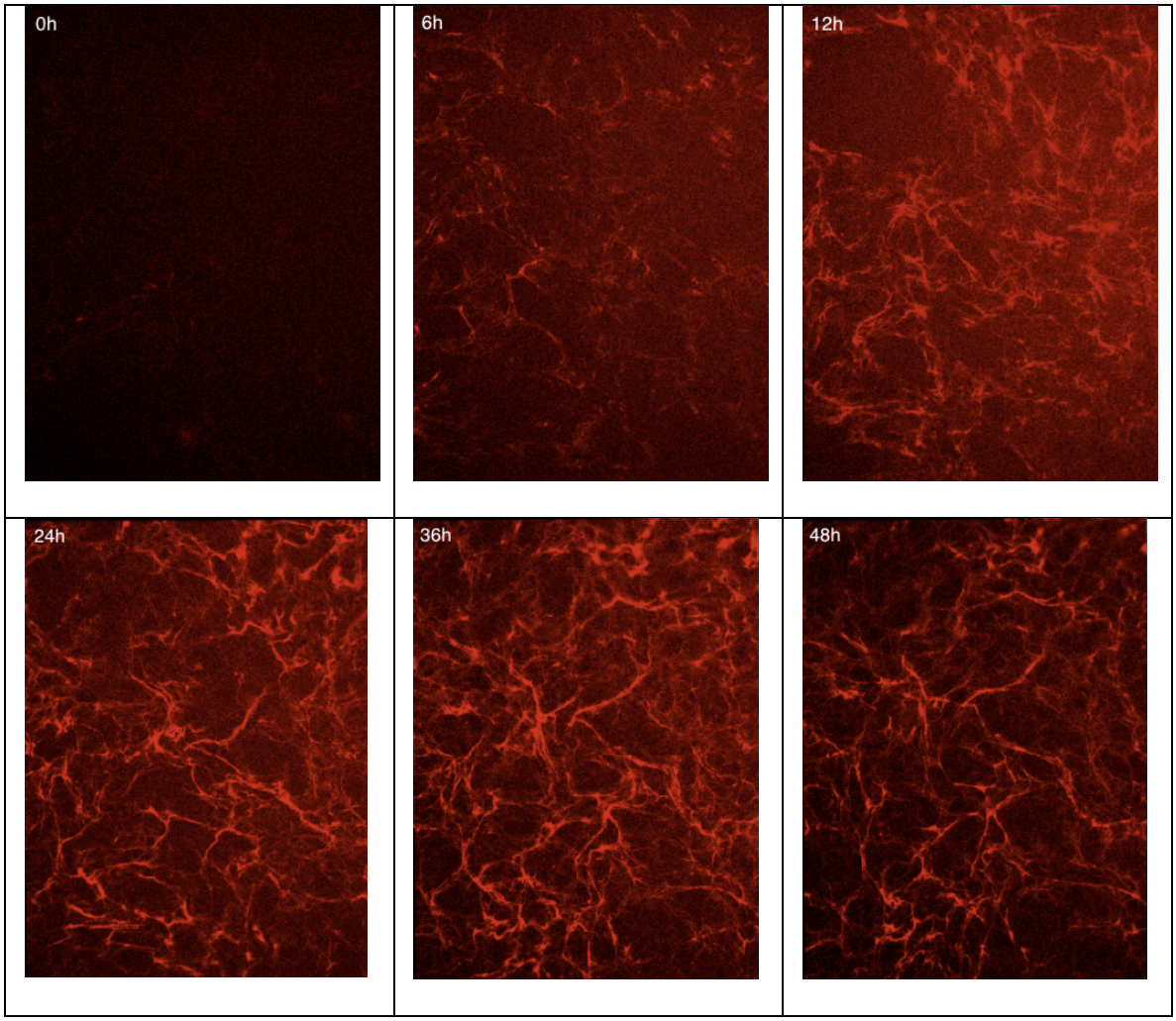

Figure 1.1: Showing the difference in the position and density of the fibrils at various times during the time lapse imaging experiment.

1.1.2 Modified 2D Digital Image Correlation Methodology

There are various methods of processing images and tracking any feature in it. Each method uses a different algorithm and has different specifications that are suitable for a certain group of applications. For this application the technique of 2-D Digital Image Correlation has been used, as it is best suited to process images where sub pixel resolution is required. This technique involves processing of a stack of consecutive images to obtain the displacement vector acting on them. Eberl et al (Eberl, Thompson, & Gianola, 2006) first developed a Program based on this method and since the program is open sourced, individual programmers have the flexibility to make modifications to the program. We have communicated with the original developers of the program and obtained their consent to continue further development of the software they have developed.

The program was developed using Matlabâ and requires Matlabâ version 7 or higher to run efficiently. The program is made up of a series of individual programs that need to be executed in a specific order to obtain the desired results and the steps required to do this task are outlined below:

a) The first step in the algorithm involves selecting the list of images that need to be considered from the experiment, which for our initial analysis is the last 12h of the movie, represented by images 108-144. These are saved in a file that can be accessed by other functions located in the same folder.

b) The next part of the process involves defining the features on the image that need to be observed and tracked through the entire image set. The features, individual fibronectin fibrils in this case, within that region are marked by points called raster points which can be distanced and shaped in various ways based on the options selected. All of this is done over

an image that is considered the base image (in the initial analysis, this was image #108). The base image is considered such that it can be used to compare against the subsequent image (image #109 in the initial analysis) and/or the rest of the images.

c) After the features of interest are defined, the other images are compared with the base image and the motion of the feature within that region is tracked using a Matlabâ function 'cpcorr', which uses normalized cross correlation to determine the new locations for the raster points and repositions them.

d) Finally, these raster locations are stored as pixel values and can be used to calculate the displacement of the raster points from image to image. These displacement values are calculated and input into various strain formulae, all of which are described in detail in the following chapters.

The original program was not optimal for our application, as it was not designed to track the motion of a shape that was as random and varying as a fibronectin fibril. Also the program lacked certain features such as;

- the option to save the images that were tracked so that they could be used later for validation and comparison
- the ability to accommodate multiple regions of interest or the ability to automatically select the base image from a set of images
- the flexibility to accept multiple image formats with a better algorithm to process the file names and many other such functionalities.

For all these reasons, and others not described, the original program was used as a platform for developing the quantitative analysis of fibronectin fibril motions, displacements and

strains, but has been extensively modified to overcome its limitations for this biological application.

CHAPTER 2

DESCRIPTION OF THE PROGRAM

The program for the application developed here is based on an already existing program (Eberl, Thompson, & Gianola, 2006) that was written with a similar intent, namely to calculate strains on images by observing the displacement of image features in consecutive images. Extensive modifications have been made to this program to suit our application. This chapter provides a detailed description of the program along with the changes and the reasons for the changes.

Many components in the working of this 2-D Digital Image Correlation are similar to the working of the Particle Image Velocimetry (PIV) technique. The PIV method is also a form of Digital Image Correlation since it uses consecutive images to calculate its displacement vectors. Like most other 2-D Digital Image Correlation techniques, PIV uses one image pair at a time, with the first image acting as a reference image and the second as the input image, and calculates the correlation between them. Once the spatial mappings of transformation between the two images are deduced, their displacement values are calculated.

The method used by PIV to calculate the spatial mapping transformations between the images is a two-step predictor – corrector approach. A search window is created around the sub-window that defines a feature and normalized cross-correlation (Matlab® function normxcorr2) is applied to it. The algorithm for the corresponding normalized cross correlation is given by the following equation

$$\gamma(u,v) = \frac{\sum_{x,y}\left[f(x,y) - \bar{f}_{u,v}\right]\left[t(x-u,y-v) - \bar{t}\right]}{\left\{\sum_{x,y}\left[f(x,y) - \bar{f}_{u,v}\right]^2 \sum_{x,y}\left[t(x-u,y-v) - \bar{t}\right]^2\right\}^{0.5}}$$

where

- f is the image.
- $\bar{t}$ is the mean of the template
- $\bar{f}_{u,v}$ is the mean of $f(x,y)$ in the region under the template.

This search window and the result of the normalized cross-correlation help pinpoint the location of the feature in the target image and a set of predictor displacement values are obtained.

To eliminate spurious displacement values and to obtain a continuous interpolating function, the displacement values are fitted by a spline approximation function. The thin plate spline approximation function (Matlab® function tpaps) is used in PIV since they provide accuracy and smoothness to the graphs. Tpaps is the scattered translates form (stform) of a thin-plate smoothing spline *f* for the given data sites x(:,j) and the given data values y(:,j).

These predictor displacement values, once obtained, are then used to offset the sub-window, whose size is reduced to half, in the target image and a normalized cross-correlation is carried out for a second time. After the correlation peak values are obtained, they are fitted by thin plate spline approximation again and the final displacement values are obtained. These displacement values are then applied to determine the Green-Lagrange strain tensors.

The results of the PIV technique are quite accurate and the PIV technique was thus used as a background for the Matlab® application developed here.

2.1 Description of the Original Program

The original program was developed for the purpose of measuring strains in samples that are difficult to handle and hence require non-contact methods of measurement. The authors (Eberl, Thompson, & Gianola, 2006) have used the method of Digital Image Correlation where a series of consecutive images can be used to calculate the strain with sub-pixel resolution. The primary contents of the original program are

a) A file list generator (filelistgenerator.m): This function generates a file that contains the names of all the consecutive images to be used for calculation of displacement.

b) Grid Generator (grid_generator.m): This function helps specify the points on the image that need to be observed. These points are all placed on or around a feature whose motion is to be measured. A reference image specified by the user is used as the base image on which the grid points are mapped.

c) Automate Image (automate_image.m): This function tracks the motion of the grid points generated in the grid_generator file. This file recognizes the new position of the feature being tracked by the grid points by using normalized cross correlation to verify the pixels around the grid point in the current image to the grid point around the base or reference image. As per the results of this correlation the algorithm pinpoints the location of the feature and relocates the grid point on it.

Displacement (displacement.m): This function uses the values of the new grid locations and calculates the magnitude of displacement undergone in each image with respect to the base

image. These values are then used to calculate a variety of strains, any of which can be selected from a pop-up list that appears during the execution of the file, one at a time.

2.2 Modifications to the Original Program

The original program was developed for a general purpose of calculating strains from a series of images. However, several parts of the program are not suitable for our application because of various factors like the shape of the fibrils, the file names, the number of fibrils to be observed, the magnitude of displacements and stresses between two consecutive images and the total displacement and stress per fibril. Hence, this required extensive changes to be made in the original program and also to develop a new program

This section describes in detail the changes made to the original program in order to suit the current application. All the files, except the displacement.m file were modified in this work. The original file to calculate displacement was not used at all and a new file – workspline.m – was developed for this purpose. Below is an in-depth explanation of each file and the changes made along with the reasons for the changes.

2.2.1 Filelistgenerator

The main function of this program is to generate a list of all the images that the user wishes to process. This list is then saved so that the other three files can continuously refer to it while processing the images. The entire function is written with the assumption that the filenames of the images are in the form ‘Xx.extension’, where X denotes a string of characters that could be a combination of alphabets, numbers and punctuations, which remain constant for all the images, and x denotes a particular number that is unique to each image. It

is also assumed that the set of images being processed are in an ascending sequence that is x (current image) – x (previous image)=1 for all concurrent images. The '.extension' could consist of a variety of file types like tiff, jpeg, png, gif and all other file formats accepted by Matlab .

The function has two major ways of selecting images- Automatic and Manual as shown in figure 2.1.

Figure 2.1: Creating the filenamelist

1. If the 'Automatic' function for selecting the images is chosen then the user is required to select the first image (the image with the lowest value of x in it) and the function automatically assigns the names to the next images by incrementing the number in the name of the image until the last available image is selected. This part of the function is taken from the original function and has not been changed.
2. In the 'Manual" section of the function several changes have been made so that the function accepts any filename irrespective of its length and the number of characters present in it. Originally the user was required to specify the x values of the first and

last image. But the value of x could not exceed 9999 because the format of the function did not support any value that had more than 4 digits in it. After the x values were entered the user was required to enter the X string. Again even with the X string the length of the string was limited to 4 characters. This would require the filename to have exactly 4 characters in it or the function would reject the file name. Hence, to make the function user-friendly and to ensure that the function accepted all filenames without any constraints on the number of characters or digits in it, the function has been modified to accept the filenames differently. As per the updated function, the user can select the first image and the last image from a selection window. These strings are stored in 2 different variables and subjected to a letter test where all the characters in the entire string are denoted by a 1 if the character is an alphabet and a 0 if the character is a non-alphabet. The function then searches for the '.' character in the entire string, since according to our assumption the x value is located just before '.extension', and a counter verifies the value of each character backwards from that point until an alphabet (i.e. a value of 1) is reached. This gives the x values of the first and the last image and these values are used to generate all the image names that are located in between these two values. The image names are then stored, in a single column, in a file called 'filenamelist.mat'. The other functions that need to refer to the image list can load this file into their workspace and work on these images.

2.2.2 Grid_generator

The main function of this algorithm is to specify the region of interest (ROI) in the images that the user wishes to focus on. The user has an option to choose from a variety of

shapes to define their ROI as shown in figure 2.2. But since this process deals mainly with fibronectin fibrils, which have no definite shape, the function has been modified to give the user an added option of selecting a specified number of points along an individual fibril. This functionality has been executed by adding the feature 'Manually select markers' visible in Figure 2.2. All these points, if placed accurately and strategically, would help provide accurate displacement and strain values for the fibril. In the original function after the required shape was selected, the user was also required to select the base image. In this process the base image always is the first image and so to avoid redundancies and to save the extra steps, the first image from filenamelist.mat is loaded as the base image by default.

While manually selecting the raster points, the user is required to specify the number of fibrils he/she wishes to work on and also specify the number of raster points he/she wishes to select per fibril. These values are stored in a file called 'number_s.dat' and used in later functions to differentiate between the displacement and strain values of individual fibrils. Since this is a new addition to the function and since all the other functions have been modified to process images using the data in number_s.dat, the older shapes in grid_generator also needed modifications so they would also store data in number_s.dat every time they are run. After the number of fibrils and the number of raster points per fibril have been specified, the base image opens up and the user can then click on the fibril to place the raster points.

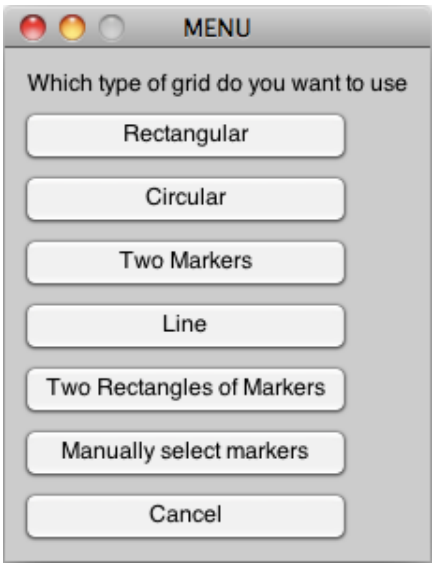

Figure 2.2: The different shapes of ROI that the user can choose

Every time the user selects a point it is highlighted on the image by a blue '+' sign and the x and y coordinates of the point are stored in 2 different variables called gridx and gridy respectively. The title of the image has also been modified to constantly show the user the current fibril and the number of raster points selected on the fibril along with the total fibrils and the total number of raster points per fibril the user is required to select. After all the points along a fibril are selected a line joins up all those chosen points and helps the user estimate the accuracy of placement of the raster points as shown in Figure 2.3. After all the fibrils are processed the user has an option to save the points or try again to place the points more accurately. The user is still restricted to choosing the same number of raster points for all fibrils irrespective of their lengths.

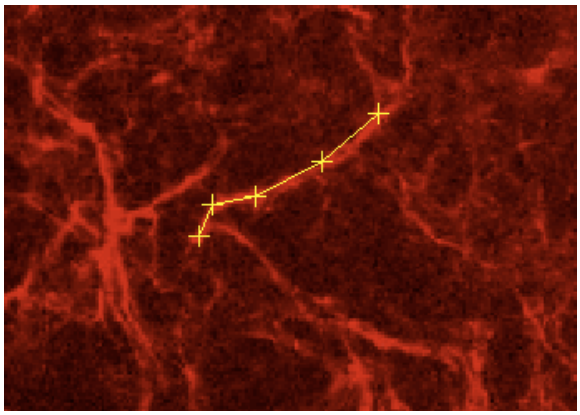

Figure 2.3: A close-up of the placement of raster points.

2.2.3 Automate_image

The main function on this algorithm is to track the motion of the region of interest through the set of images and record the new pixel values of the raster points based on the motion of the features. The inputs to the function are the files filenamelist.mat, which is generated from the function filelistgenerator, and gridx.dat and gridy.dat, which are generated from the function grid_generator.

a) The original function uses the first file in filenamelist.mat as the base image and loads the raster points from gridx and gridy onto it.

b) It goes into a loop where all the images, starting from the second, are loaded and the raster points from gridx and gridy are loaded onto them and the pixel values are compared with the base image using the function *cpcorr*. *Cpcorr* uses normalized cross correlation to compare the RGB values of the pixels around each raster point of the base image and the current image being processed (also known as the input image) thus locating the new position of the raster point.

c) These new values are then stored in two files ‘validx.dat’ and ‘validy.dat’.

For this algorithm to work accurately, it requires that the lighting conditions remain constant throughout the entire series of images. This would ensure that the RGB values for any feature remain constant throughout and is hence easily traceable to its new location.

The search window for cpcorr is an 11x11 matrix for the base image and a 22x22 matrix for the input image, by default. This means that when *cpcorr* is executed, it reads the RGB values of all the pixels in a 11x11 matrix around the raster point in the base image and a 22x22 matrix around the current image and subjects them to a normalized cross correlation to determine the motion of the features. This helps pinpoint the updated location of the feature under consideration.

The width of the search window is determined by a variable called *corrsize* in the function *cpcorr*. This value is 5 by default which means that *cpcorr* is going to consider up to 5 pixels in all four directions around the current pixel in the base image for the normalized cross correlation, thus forming a square matrix with a total pixel count of 11 in any given row or column. Although 5 is the default value for the *corrsize*, it can be changed to any value as per the biology and the interval between the images. If the features experience very little motion in-spite of having a reasonable time period between consecutive images, it is recommended to have a small *corrsize* so as to reduce noise from the neighboring features and to increase the sensitivity of the tracking. Similarly if the features experience an amount of motion larger than the size of the search window, it is recommended to have a larger *corrsize* proportionate to the amount of motion. The selection of *corrsize* also depends on the proximity of the features being observed. If more than one feature falls in the same search window, there is a possibility of both the features being overlapped into one. All these factors

need to be considered before choosing the right *corrsize* for the process. Further studies have been done to understand the behavior of the function with different values for *corrsize* and these are explained in detail in Chapter 3.

Further modifications have been made to Automate_image and they are described below:

1) To ensure the effectiveness of the function even if the light conditions vary and if new features, such a new fibril or a new cell, emerge during the course of the experiment, the base image has been configured to change dynamically every time a new input image is selected. Three such functions have resulted from it
   a) automate_image_1 where the base image is updated to the current image after every image instead of the first image.
   b) automate_image_3 where the base image is updated to the current image after every set of 3 input images.
   c) automate_image_5 where the base image is updated to the current image after every set of 5 input images.

   The reason the base images have been updated from a fixed first image is to accommodate large motions that may occur through the duration of the biological experiment that may lead to a considerable change in the image features from the beginning to the end of the image sequence. The results of the three functions have been compared and based on this comparison it was observed that automate_image_1 provided the most effective tracking of the fibrils. Hence automate_image_1 was chosen to be best suited for this application.
2) To manually observe the tracking of the raster points the function has been modified to save the images in a file 'displacement_tracking'. These images can be used to

observe the effectiveness of *cpcorr* to track the motion of any particular fibril or raster point.

3) Since displacement.m is not being used, automate_image_1 has been configured to calculate the displacement values of each raster point with respect to its value in the previous/base image and a *quiver* function has been added to graphically represent the amount of displacement per raster point. The *quiver* function takes its inputs from the raster locations of the base image and the displacement values of the current image and generates an arrow depicting the direction and magnitude of displacement. Figure 2.4 depicts the output of the quiver function.

2.2.4 Workspline

The main function of this algorithm is to calculate the Green Lagrange's strain tensor of the raster points using a set of mathematical equations. This also includes calculation of sub-pixel resolution values of the raster points using the spline function.

The main components of Green Lagrange's strain tensor depend on the calculation of the displacement and deformation gradient both of which are explained in greater detail below.

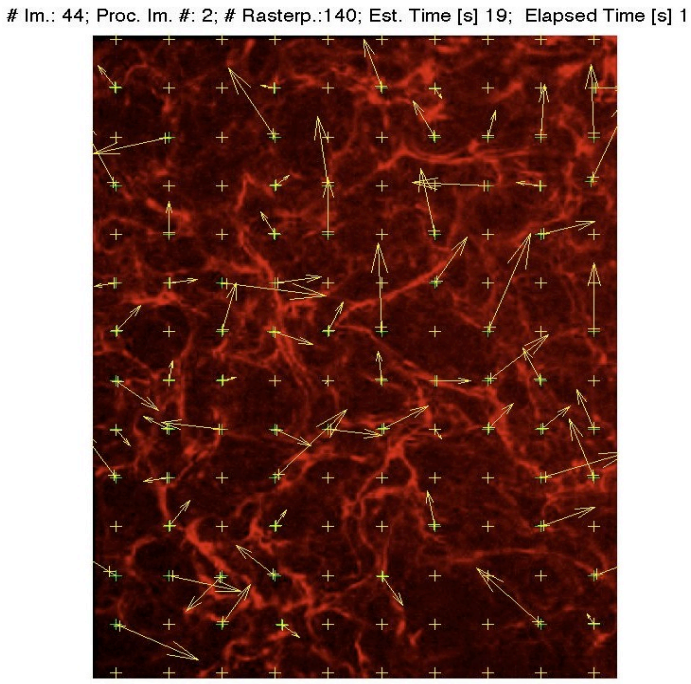

Figure 2.4: Output of the *quiver* function where the direction of the arrow depicts the direction of the displacement and the length of the arrow depicts the relative magnitude of displacement.

2.2.4.1 Calculation of displacement and deformation gradient in 1-D and 2-D

Consider a fibril of length dx whose end points, denoted by A and B, are stretched to new positions a and b. If the point A is denoted by u(x) then B can be denoted as u(x+dx).

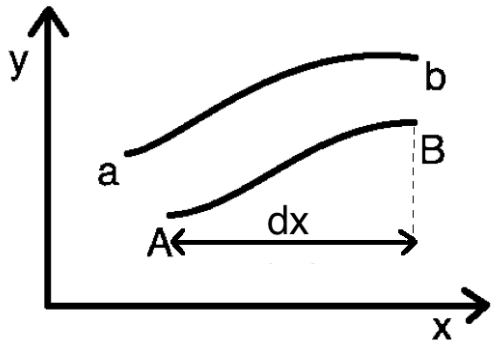

Figure 2.5: the coordinates of the ends of the fibril on a 2-D graph.

For a 1 dimensional analyses if $\partial u = u(x + dx) - u(x)$, then

Displacement = $\frac{\partial u}{dx}$, and ----(2.1)

Deformation Gradient = $\left(1 + \frac{\partial u}{dx}\right)$ ----(2.2)

For a 2 dimensional analysis, points A and B are denoted in 2 dimensions as

A= $(u_A, v_A) = (x, y)$ and B= $(u_B, v_B) = (x + dx, y + dy)$.

Thus if $\partial u = u_B - u_A$ & $\partial v = v_B - v_A$, then the Green Lagrange's strain matrix is denoted by

$$\begin{bmatrix} 1 + \frac{\partial u}{dx} & \frac{\partial u}{dy} & 0 \\ \frac{\partial v}{dx} & 1 + \frac{\partial v}{dy} & 0 \\ 0 & 0 & 0 \end{bmatrix} \quad \text{----(2.3)}$$

2.2.4.2 Calculation of the matrix values for the current experiment

The displacements are similar to the procedure described above. There is a fibril with two points along it called A and B denoted by (x_A, y_A) and (x_B, y_B). This fibril has moved to a new position a and b denoted by (x_a, y_a) and (x_b, y_b).

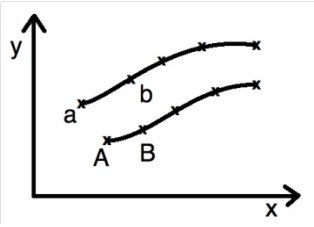

Then

The displacement is given by

$$dx = x_B - x_A$$

$$dy = y_B - y_A \qquad \text{----(2.4)}$$

and the deformation is given by

$$\partial u_A = x_a - x_A \qquad \partial u_B = x_b - x_B$$

$$\partial v_A = y_a - y_A \qquad \partial v_B = y_b - y_B \qquad \text{----(2.5)}$$

thus the Green Lagrange's strain matrix is given by

$$\begin{matrix} F_{11} & F_{12} & 0 \\ F_{21} & F_{22} & 0 \\ 0 & 0 & 0 \end{matrix} \qquad \text{----(2.6)}$$

where,

$$F_{11} = 1 + \frac{\partial u_A}{dx}, \qquad F_{12} = \frac{\partial u_B}{dy}$$

$$F_{21} = \frac{\partial v_A}{dx}, \qquad F_{22} = 1 + \frac{\partial v_B}{dy} \qquad \text{----(2.7)}$$

Hence according to Green Lagrange's strain tensor calculations, for a matrix of dimensions (i,j)the 4 strain values can be obtained by using the equation

$$E_{ij} = \frac{1}{2}(F_{ki}F_{kj} - \delta_{ij}) \qquad \text{----(2.8)}$$

where δ_{ij} is a unit matrix of dimensions (i,j).

Since we have a 3x3 matrix here, i=j=k=3 and

$$\delta = \begin{matrix} 1 & 0 & 0 \\ 0 & 1 & 0. \\ 0 & 0 & 1 \end{matrix} \qquad \text{----(2.9)}$$

Substituting eq (2.9) in eq (2.8), we get the following 4 equations.

$$E_{11} = \frac{1}{2}(F_{11}F_{11} + F_{21}F_{21} + F_{31}F_{31} - 1)$$

$$E_{12} = \frac{1}{2}(F_{11}F_{12} + F_{21}F_{22} + F_{31}F_{32})$$

$$E_{21} = \frac{1}{2}(F_{12}F_{11} + F_{22}F_{21} + F_{32}F_{31})$$

$$E_{22} = \frac{1}{2}(F_{12}F_{12} + F_{22}F_{22} + F_{32}F_{32} - 1) \quad \text{----(2.10)}$$

where,

E_{11} represents the axial elongation,

E_{22} represents the transverse strain &

E_{12} and E_{21} represent the shear strain

Thus we obtain all the 4 strain vectors for the length of the fibril between A and B. This process is continued for every set of two raster points on the fibril until all the individual strains are obtained.

This chapter has presented the entire methodology of processing the images and obtaining their strain values. The next chapter describes how this methodology was applied to the images obtained from the biological experiment and discusses the results of the analysis.

CHAPTER 3

RESULTS AND OBSERVATIONS

3.1 Introduction

This chapter describes the comparison and analysis of the strain values obtained after the images have been processed and the displacement values are run through the algorithm for calculation of strain tensors. The process of comparison is divided into two parts -

- Manually calculating the length of each fibril for every image in a test image stack
- Calculating the length of the same fibrils from the strain tensors obtained using the modified DIC algorithm

The accuracy of the strain vectors would determine the precision of the two lengths obtained. The methods are explained below in detail along with the calculation algorithms.

3.2 Manual calculation of lengths

The first part of calculating the strain values is to manually calculate the length of the fibril for each image. The easiest way to do this is to sequentially go through all the images and calculate the distances between two adjacent raster points along the fibril. By adding up these individual lengths we can obtain the total length of the fibril. To calculate the length between two raster points a digital imaging software called GraphClick® is used. The advantage of this software is that when any image is selected and its resolution is specified as the x and y coordinate limits of the image then all the pixels in the image are represented

along the x–y coordinate axis. Thus whenever a pixel is selected, its value can be obtained and, subsequently, its distance from any other point can be determined.

To follow the tracking efficacy of Matlab the images that were saved during the execution of automate_image are used as the image set for GraphClick. This has the advantage of providing a visual verification of whether the raster points were correctly relocated onto the fibril by Automate_image.

Since the images used for the comparison have a resolution of 296x396 pixels, these are specified as the x and y coordinate limits respectively on GraphClick. All the images starting from the initial base image are loaded onto GraphClick and the locations of the raster points are recorded onto an Excel Sheet where the distance between two consecutive raster points and the total lengths of the fibril for each image is obtained. Figure 3.1 shows the GraphClick window after the image is loaded and its X and Y axes are determined. The smaller window on the right side of the image is where the pixel values that are selected are recorded.

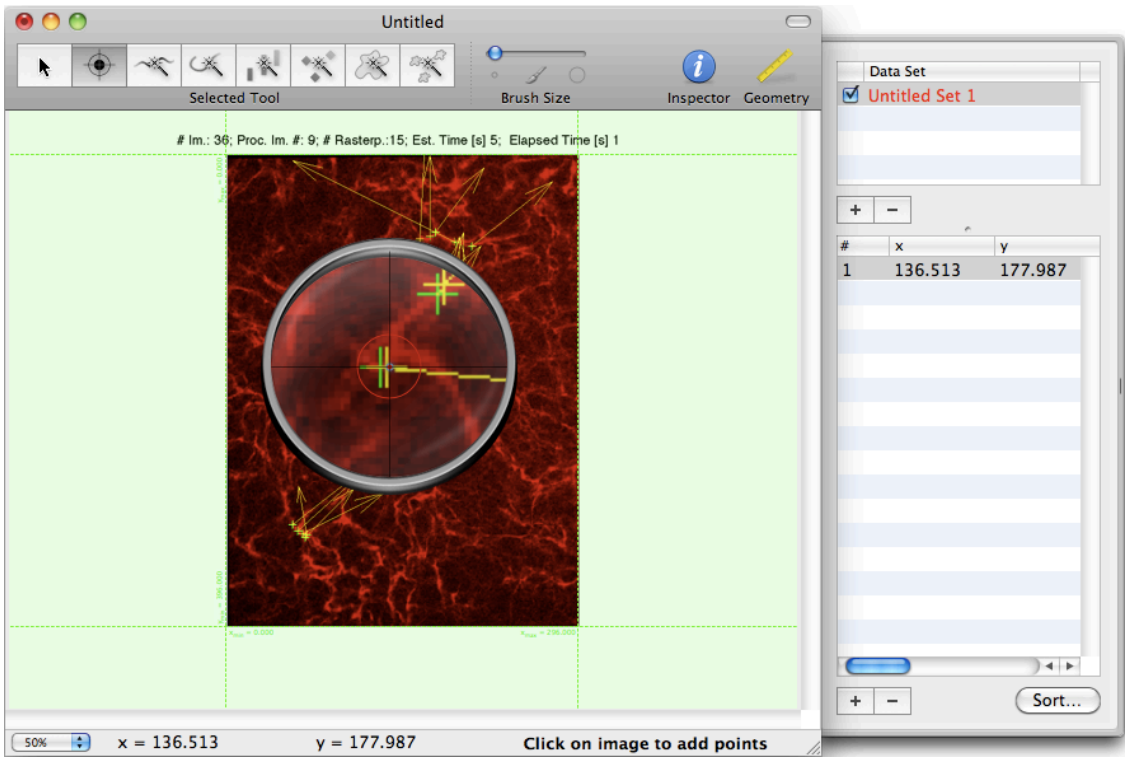

Figure 3.1: GraphClick window showing an image that is being used for the manual calculation. The x and y coordinate limits are visible as being 296 and 396.

3.3 Calculating lengths from the strain vectors

The second part of the comparison process involves calculating the length of the fibril from the strain values of that fibril. This is done using Matlab . The function for calculating the lengths is written down as a part of the function workspline. The formula the x and y coordinates of the pixel locations of the raster points from validx and validy. These are obtained during the execution of the function automate_image and loaded into workspline at the beginning of the function.

The first step in this process is to take the x and y coordinates of raster points of the previous image from validx and validy and calculate the lengths between two consecutive raster points. This is done using equation 3.1.

$$L_0 = \sqrt{[x(i+1) - x(i)]^2 + [y(i+1) - y(i)]^2} \qquad \text{---- (3.1)}$$

where i = current raster point and x and y are the values from validx and validy and L_0 denotes the length between the raster points of the previous image.

This length is used to calculate the x and y intercepts of the raster points of the previous image by using the formula

$$\text{x intercept } \xi_1 = [x(i+1) - x(i)] + length] \qquad \text{----(3.2)}$$

$$\text{y intercept } \xi_2 = [y(i+1) - y(i)] + length] \qquad \text{----(3.3)}$$

where i = current raster point and x and y are the values from validx and validy.

The strain values that have already been calculated have values of $E_{11}, E_{12}, E_{21} \& E_{22}$ for the current experiment.

The x and y intercepts along with the strain values are then used to calculate the lengths between raster points of the current image by using equation 3.4.

$$L_1 = L_0\sqrt{1 + 2\xi_i E_{ij} \xi_j} \qquad \text{----(3.4)}$$

where L_1 is the length between the two raster points of the current image.

Using this formula the individual lengths between all the raster points can be calculated. The sum of all these lengths would give the total length of the fibril. All these calculations are included within the function '*workspline*' and the results of this function are saved in a file called *lname*. The values from *lname* can be compared with the lengths

obtained from the manual calculation of lengths and if they are similar then the strain values are accurate.

3.4 Comparison Steps:

A comparison study was carried out using a time-lapse image series of fibronectin assembly in 2T3 osteoblast-like cells. The entire process of comparing the automated results and the manual results, starting from selecting the files to getting the final results, is explained in detail below.

3.4.1 Step 1 - Filelistgenerator

As mentioned in the earlier chapters, the original experiment lasted a period of 48 hours and a set of 144 time lapse images was obtained of fibronectin assembly in 2T3 osteoblast-like cells with a 20 minute interval between image acquisitions. For the purposes of this comparison, the set of images from the last 12-hour segment of the time lapse movie was selected, as the fibril network was well formed by that time. Although there was considerable fibril motion, the fibril features themselves were relatively stable in this later segment of the movie, and therefore the analysis is not complicated by the formation of new fibrils. This is in contrast to the first 12 hour segment of the movie in which a large number of new fibrils are formed. Thus image numbers 108-144 were entered as the input to the function filelistgenerator. Filelistgenerator then saved these image names into a file filenamelist.mat that can be accessed by any other function present in the same directory.

3.4.2 Step 2 – Grid_generator

Three fibrils were chosen from image number 108, which was selected as the base image by default, such that the fibrils were of varied lengths, shapes, orientation and had well defined ends. These fibrils were chosen during the execution of the function grid_generator. Each fibril was defined and tracked with the help of 5 raster points placed along it. The raster values from this selection were stored in files gridx and gridy. Figure 3.2 below indicates the 3 different fibrils and the placement of the raster points along their length. The strategic placement of the raster points is essential so that it can take the curves along the fibril into consideration while calculating its total length.

3.4.3 Step 3 – Automate_image

When the automate_image function was executed, the grid values from gridx and gridy were assigned to the base image. The function then selected the images one by one and updated the positions of the raster points based on the pixel values from the base image while subsequently assigning the current image to be the base image for the next cycle. So for the first cycle figure 108 acted as the base image and figure 109 acted as the current image. The raster point locations of both images were considered to be gridx and gridy initially. All these values were input to the function *cpcorr* that used a search window of a 11x11 pixel matrix around the raster point locations of the base image and a 22x22 pixel matrix around the raster point locations of the current image. The matrix from the base image was then subjected to a normalized cross correlation and its results were used to determine the new positions of the raster points in the current image.

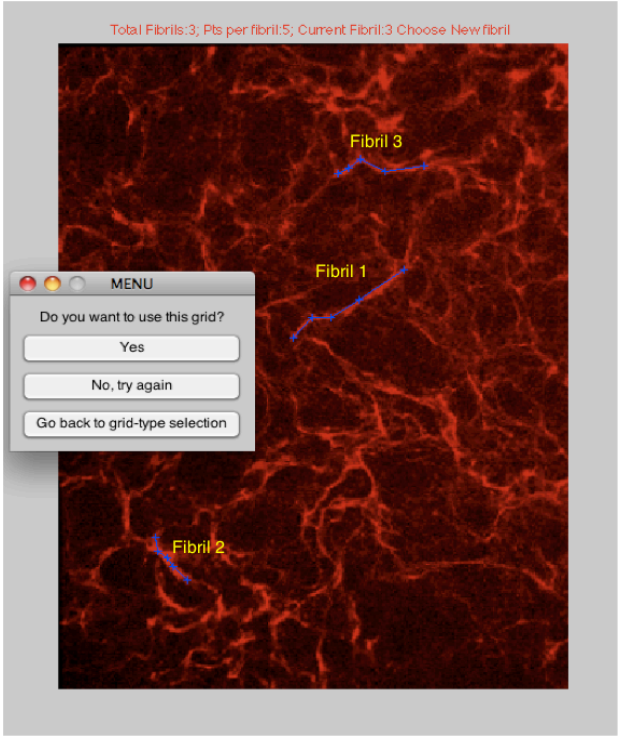

Figure 3.2: The 3 fibrils chosen for the comparison. Note the difference in their shapes, lengths and orientation. The image also shows the option of changing the raster point locations if their placement seems unsatisfactory.

Once the new location of the raster points was obtained the raster points were moved to those locations and the values were saved in the files validx and validy. A copy of the image with the updated raster point locations was saved in the file displacement_tracking. During the next cycle figure 109 became the base image and its raster point locations were used as the initial raster point locations for both the base and current images and the algorithm was reapplied.

Due to the fact that the search window in the *cpcorr* function is an 11x11 matrix for the base image and a 22x22 matrix for the current image if the initial placement of raster points during the execution of grid_generator was too close the raster points run a risk of overlapping. This means that if two adjacent raster points ended up within the same search

window then both the raster points might have a similar result to the normalized cross correlation algorithm used in *cpcorr*. This would result in the new locations for both the raster points being the same thus causing them to overlap.

To graphically view the motion of the fibril a *quiver* function was also used during the execution of the automate_image function. To serve as inputs to the *quiver* function the displacement values of the fibrils were calculated by subtracting the values of the raster points of the base image from the raster point values of the current image. Using these inputs the *quiver* function drew arrows from the raster point location such that the direction of the arrow denotes the direction of the displacement and the length of the arrow denotes the relative amount of displacement. It is important to understand that the length of the arrow is not a representation of the amount of actual displacement a raster point experiences. The displacements are too small to be seen if depicted accurately by arrows. These arrows, more accurately, depict the amount of displacement undergone by the features with respect to each other. The lengths of the arrows have been multiplied by a factor of 2 to make even the smaller deviations visible.

The automate_image function was further modified so that the initial raster point positions are also visible on the images. These initial raster points were colored differently than the updated raster points. This arrangement made it easier to gage the efficiency of *cpcorr* in tracking the motion of the raster points. When the images were being saved, they had 3 distinct features on them

a) The initial raster points before being processed by *cpcorr* - denoted by green '+' signs.
b) The updated raster points denoted by the yellow '+' signs

c) The yellow arrows as a result of the quiver function to denote the displacement vectors.

All of these features are seen in figure 3.3

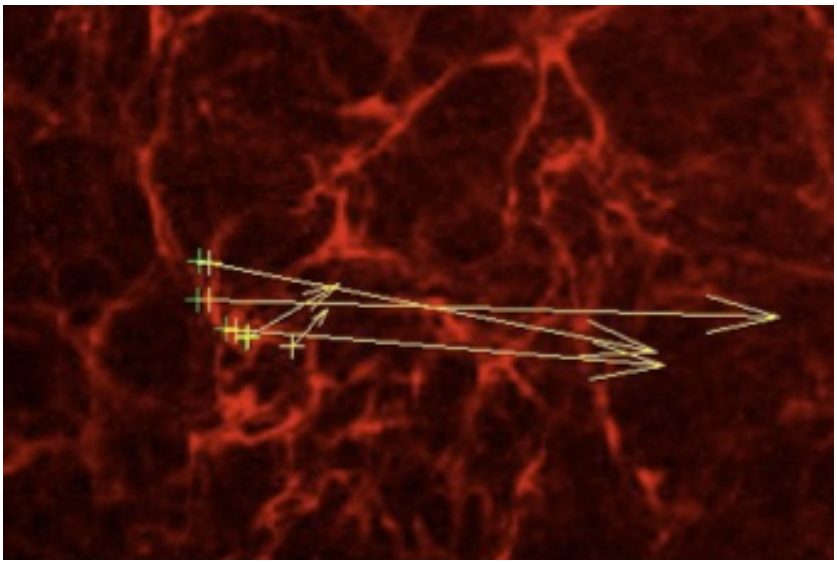

Figure 3.3: The displacement of the fibrils being denoted by the quiver function.

3.4.4 Step 4 – Calculations using GraphClick

After all the images were processed and their values stored in validx and validy, the process of manually calculating the lengths of fibrils in term of pixels was started. For this the images from displacement_tracking were used. The images were loaded into GraphClick sequentially and the raster locations of the fibrils recorded onto an excel sheet. These values were then used to calculate the distances between the raster points, which in turn were used to calculate the total lengths of the fibrils.

3.4.5 Step 5 – Comparison of manual and workspline values

To compare the strain values obtained through the workspline function with the strain values obtained from the manual calculations, the entire workspline function was executed again. The first part of the function deals with the Green Lagrange strain calculations. The second part of the function however deals with the comparison process as explained in the initial part of this chapter. The results of this part of the function were collected and pasted alongside the results of the manual calculation on the excel worksheet and a graph was drawn to compare the two results. This graph comparing the results is shown below in figure 3.4.

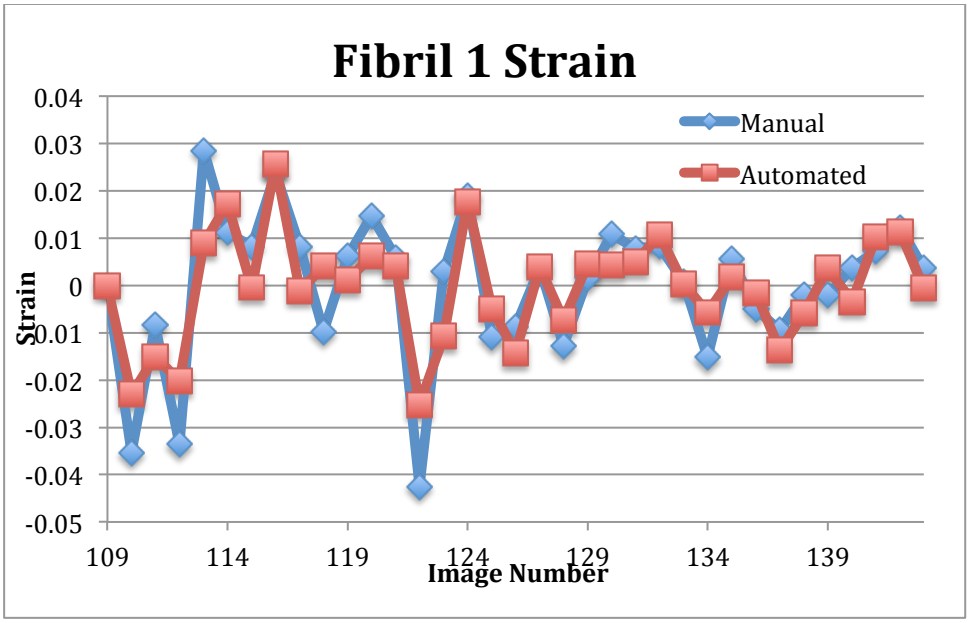

Figure 3.4: The line graph showing the comparison between the results of the manual calculations and Matlab calculations.

3.4.6 Reasons for the difference in the two results

As observed from figure 3.4 the results of the two calculations were quite close to each other. Even though the results followed a similar pattern of rise and fall they did not overlap completely. One of the major reasons for this is that the original images have a resolution of 296x396 pixels. During the execution of automate_image Matlab displays these images and then saves them with the raster points displayed on them to show which points were being considered in its calculations. The problem arises due to fact that when Matlab saves these images it changes their resolution to 1200x900 pixels. So even though we use GraphClick and recalibrate the pixel values, the selection of the appropriate pixel by hand becomes very difficult and hence imprecise. However the pixels fall within a range of -3 to 3 pixels from the original pixel locations. Though this error seems small for an individual raster point, this error accumulates for every raster point along the fibril and eventually creates a bigger difference in the total lengths than initially estimated, sometimes going up to 10 pixels away. These differences can be seen clearly by comparing the pixel values from GraphClick with the values in validx and validy as both the values point to the same raster point. Based on this comparison it was observed that the automated analysis has provided more effective tracking than the manual analysis.

3.5 Observations:

While the comparison process serves its purpose of analyzing and identifying the tracking efficacy and precision of Matlab and the algorithm in general, the algorithm can also be configured to observe various other features included in the Matlab application. One

such feature is the rectangular grid, which can be used to observe the movement of the entire collection of fibrils and view the displacements along various points in the entire image. Any general pattern of motion, if it existed, would be easier to track using this option.

The selection of a rectangular grid can be very easily done using the Rectangular Grid type selection during the execution of grid_generator. When the rectangular grid type is selected, the user has to choose an x and y resolution for the grid. This resolution is the measure of the number of pixels between two adjacent raster points. This number has to be chosen carefully so as to be able to view the motion of the fibrils accurately. If the distance between two adjacent raster points were too big then it would not cover all the motions of the fibrils. On the other hand too small a distance would cause the search windows of the raster points to overlap and lead to erroneous results. Once this resolution is selected, the grid appears on the base image and the user has the option to go ahead with the selection or to change his/her selection. This helps the user pinpoint a good resolution that is required for the observation. Once the user is satisfied with the selection, the pixel locations of the raster points are saved in gridx and gridy. The execution of grid_generator is the only main difference in the steps involved. All the rest of the steps are similar to the comparison process.

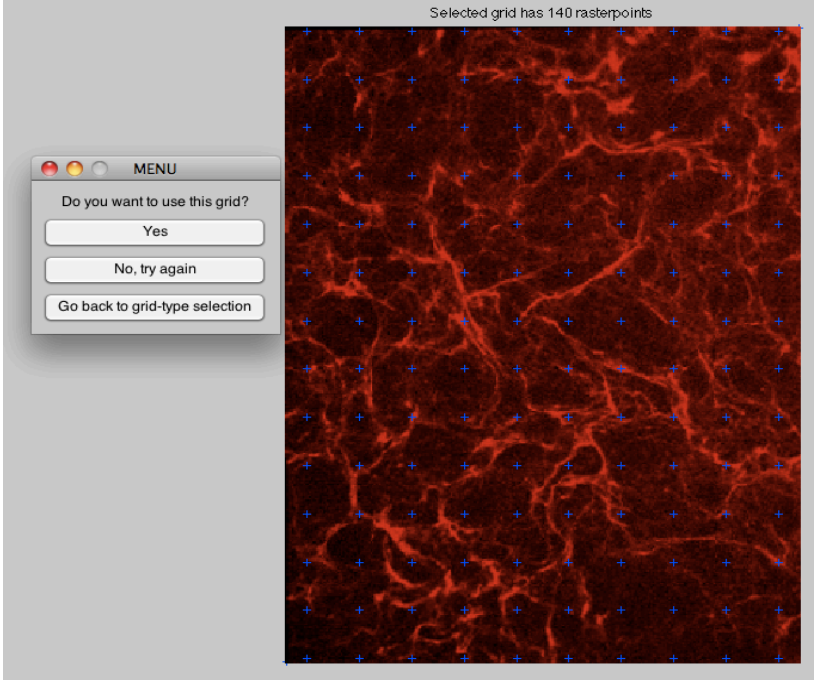

Figure 3.5: the grid_generator with a resolution of 30 pixels.

a) The first step involved the execution of filelistgenerator to ascertain the group of images or the time period of images to be observed. For this observation we used the time period similar to the comparison process, thereby selecting images 108-144.

b) The execution of grid_generator entailed the filelistgenerator where the grid type was selected to be a rectangular grid. The resolution of the grid was selected to be 30 pixels for both the x and y axes. This resolution was based on a visual determination of the closeness of the raster points and the area under them.

c) The automate_image function was then executed on the raster points to track their motion and measure their displacements. The quiver function helped to make the observations simpler by adding arrows to any raster point that showed displacement.

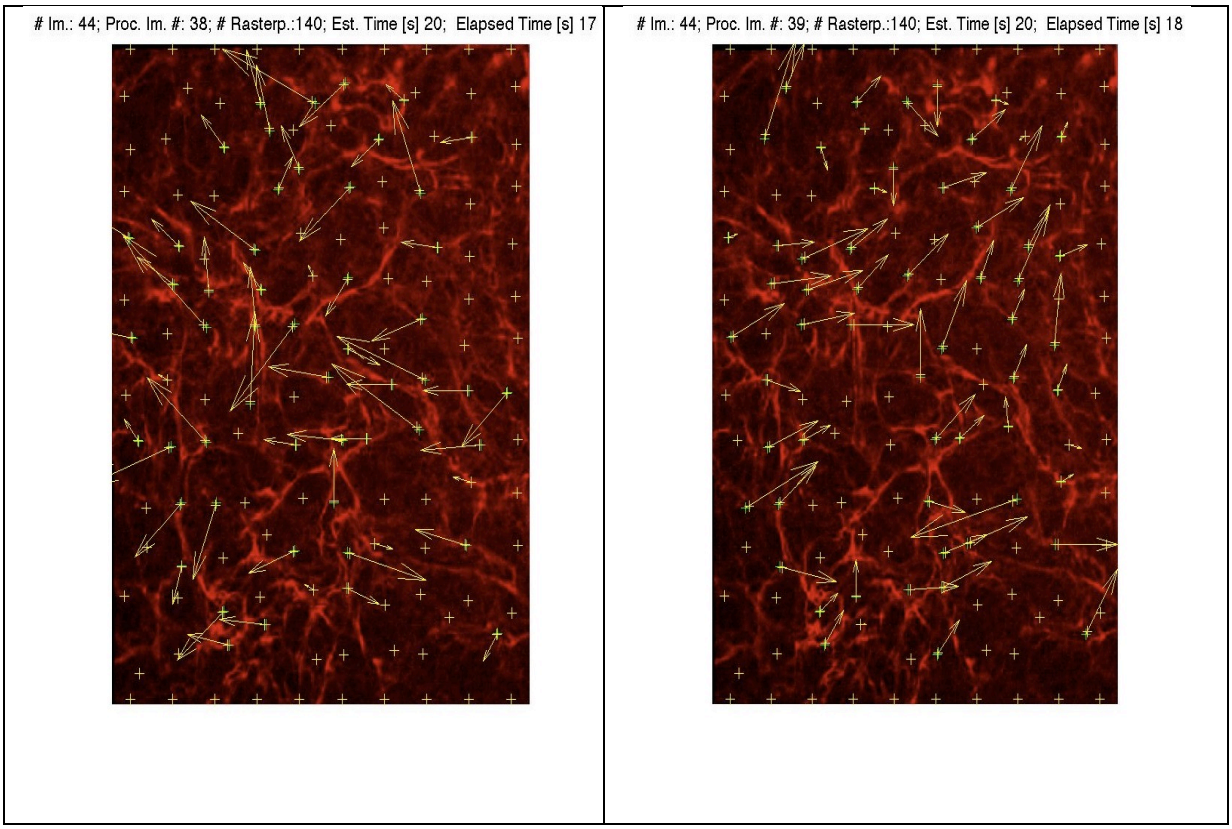

Figure 3.6: two consecutive images showing a general pattern of displacement of the fibrils. The image on the left seems to have a general leftward motion while the image on he right seems to be having a general rightward motion.

3.6 Results of the Analysis

This section presents the data obtained from different types of analysis performed on the images and discusses observations and results based on each of these analyses. Below are the sequences of images that were obtained after the execution of automate_image while. These images show the tracking efficacy of the function.

3.6.1 Images from 108-144

These are the set of images obtained while analyzing the motion of three fibrils in the image set 108-144.

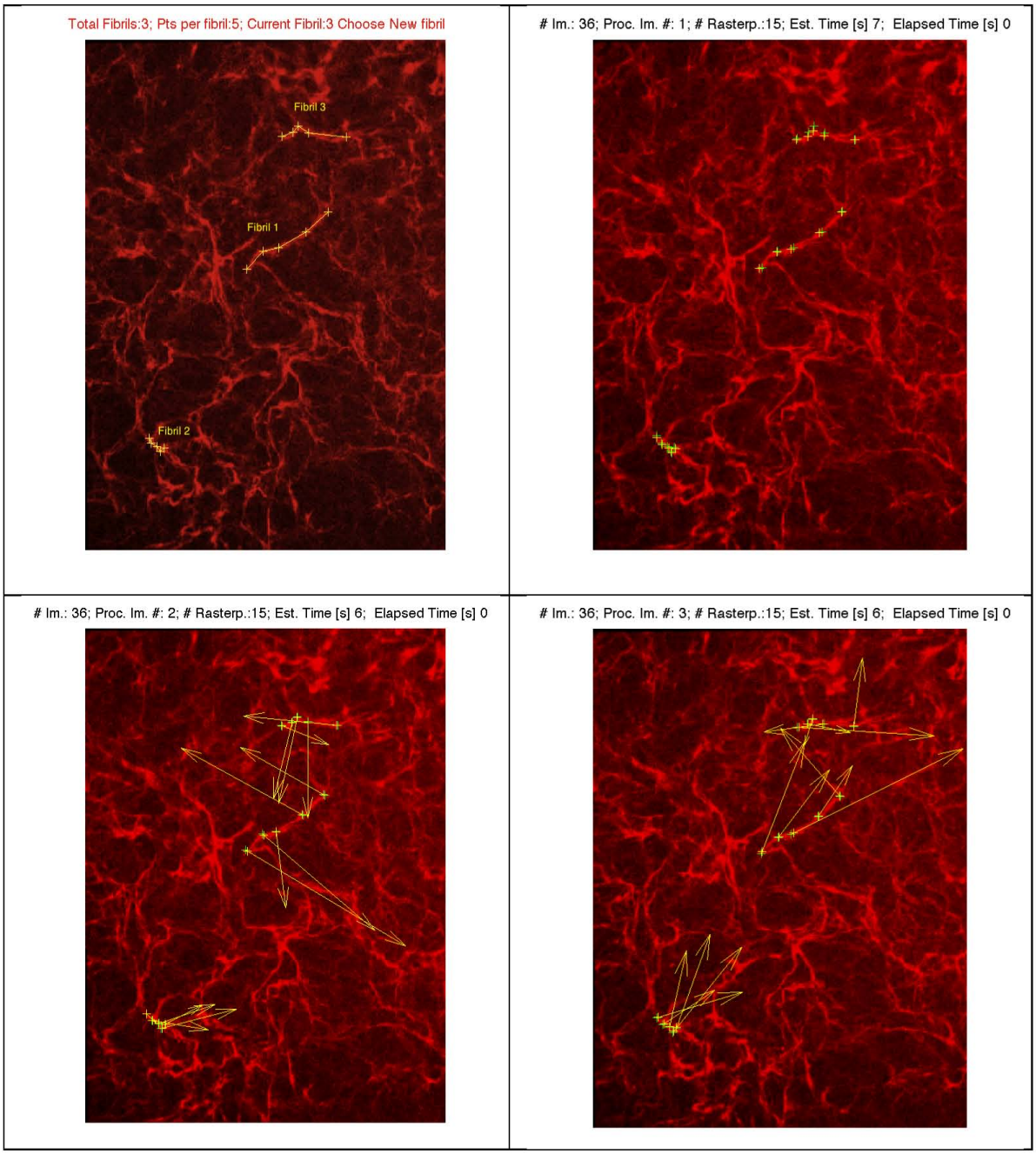
Total Fibrils:3; Pts per fibril:5; Current Fibril:3 Choose New fibril
Fibril 3
Fibril 1
Fibril 2
Im.: 36; Proc. Im. #: 1; # Rasterp.:15; Est. Time [s] 7; Elapsed Time [s] 0
Im.: 36; Proc. Im. #: 2; # Rasterp.:15; Est. Time [s] 6; Elapsed Time [s] 0
Im.: 36; Proc. Im. #: 3; # Rasterp.:15; Est. Time [s] 6; Elapsed Time [s] 0

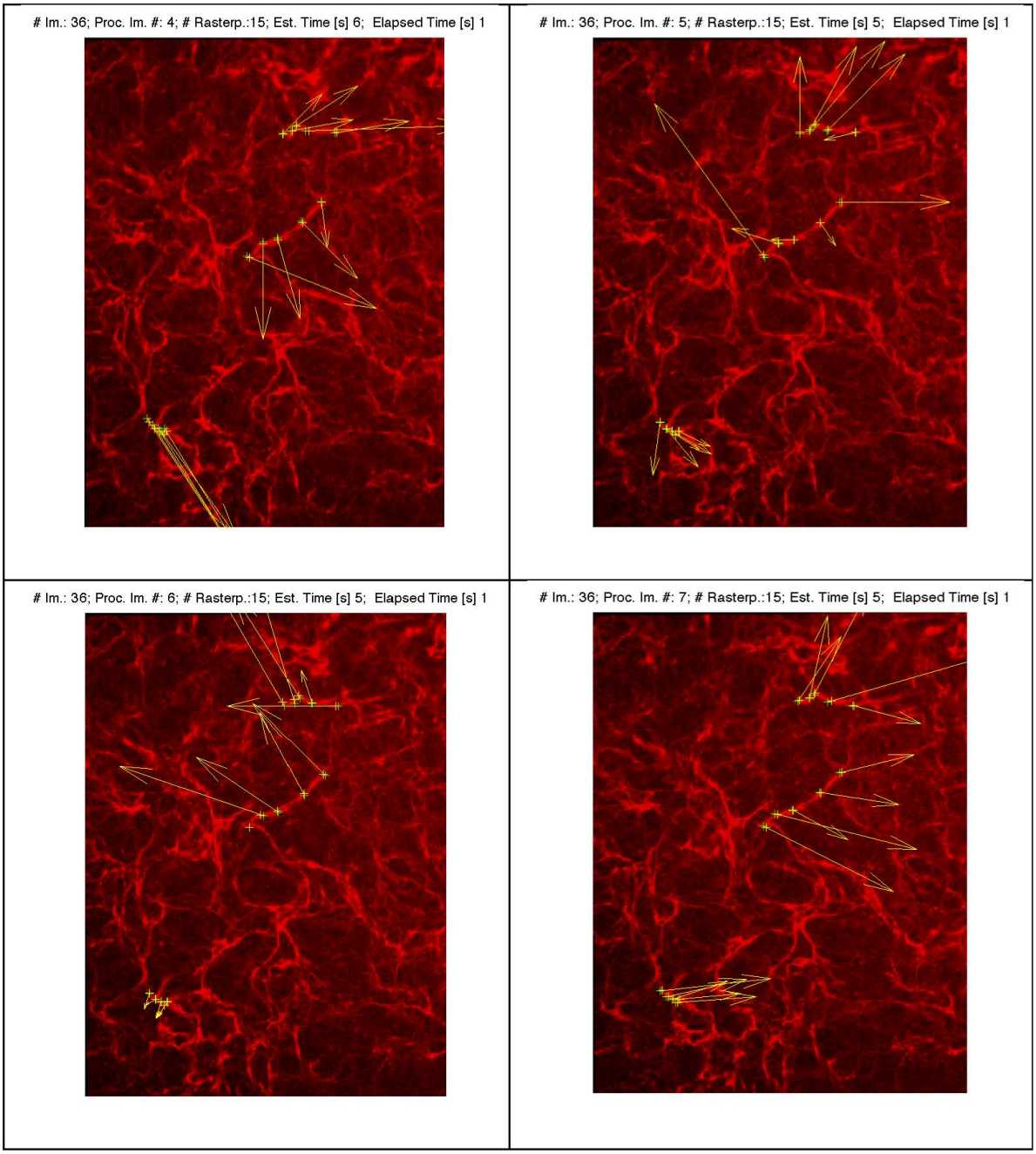
Im.: 36; Proc. Im. #: 4; # Rasterp.:15; Est. Time [s] 6; Elapsed Time [s] 1
Im.: 36; Proc. Im. #: 5; # Rasterp.:15; Est. Time [s] 5; Elapsed Time [s] 1
Im.: 36; Proc. Im. #: 6; # Rasterp.:15; Est. Time [s] 5; Elapsed Time [s] 1
Im.: 36; Proc. Im. #: 7; # Rasterp.:15; Est. Time [s] 5; Elapsed Time [s] 1

Im.: 36; Proc. Im. #: 8; # Rasterp.:15; Est. Time [s] 5; Elapsed Time [s] 1

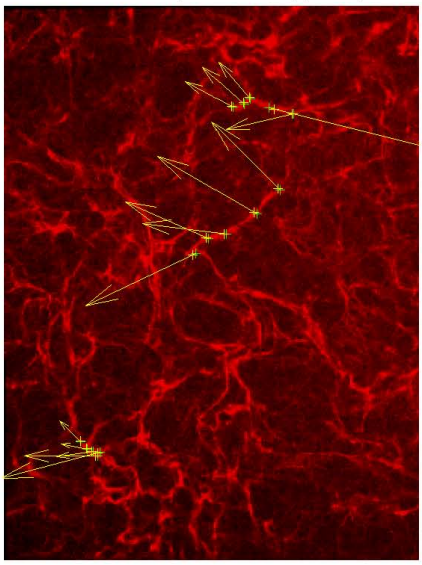

Im.: 36; Proc. Im. #: 9; # Rasterp.:15; Est. Time [s] 5; Elapsed Time [s] 1

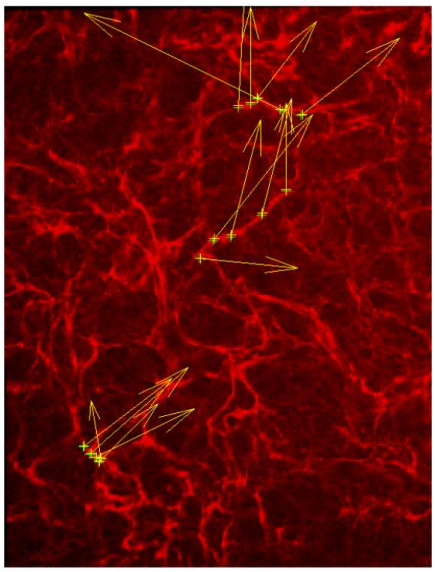

Im.: 36; Proc. Im. #: 10; # Rasterp.:15; Est. Time [s] 5; Elapsed Time [s] 1

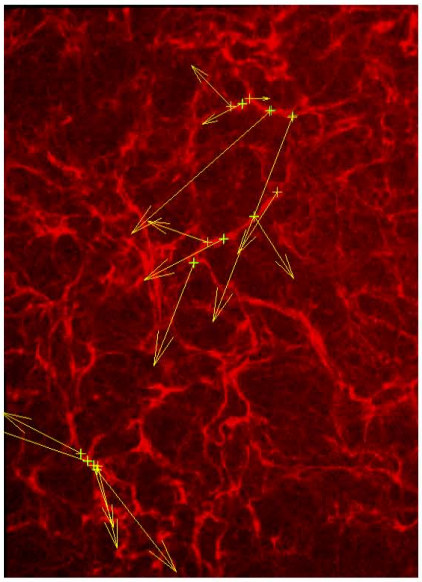

Im.: 36; Proc. Im. #: 11; # Rasterp.:15; Est. Time [s] 5; Elapsed Time [s] 2

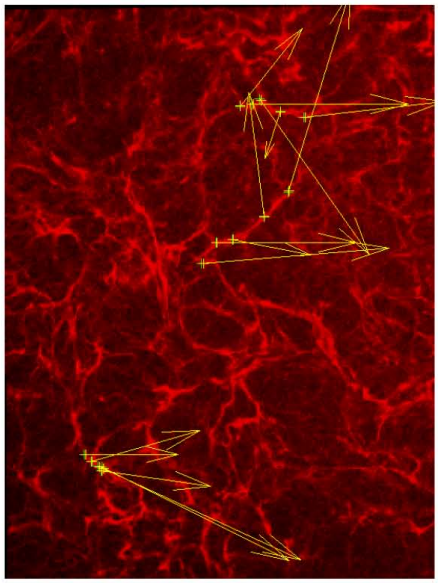

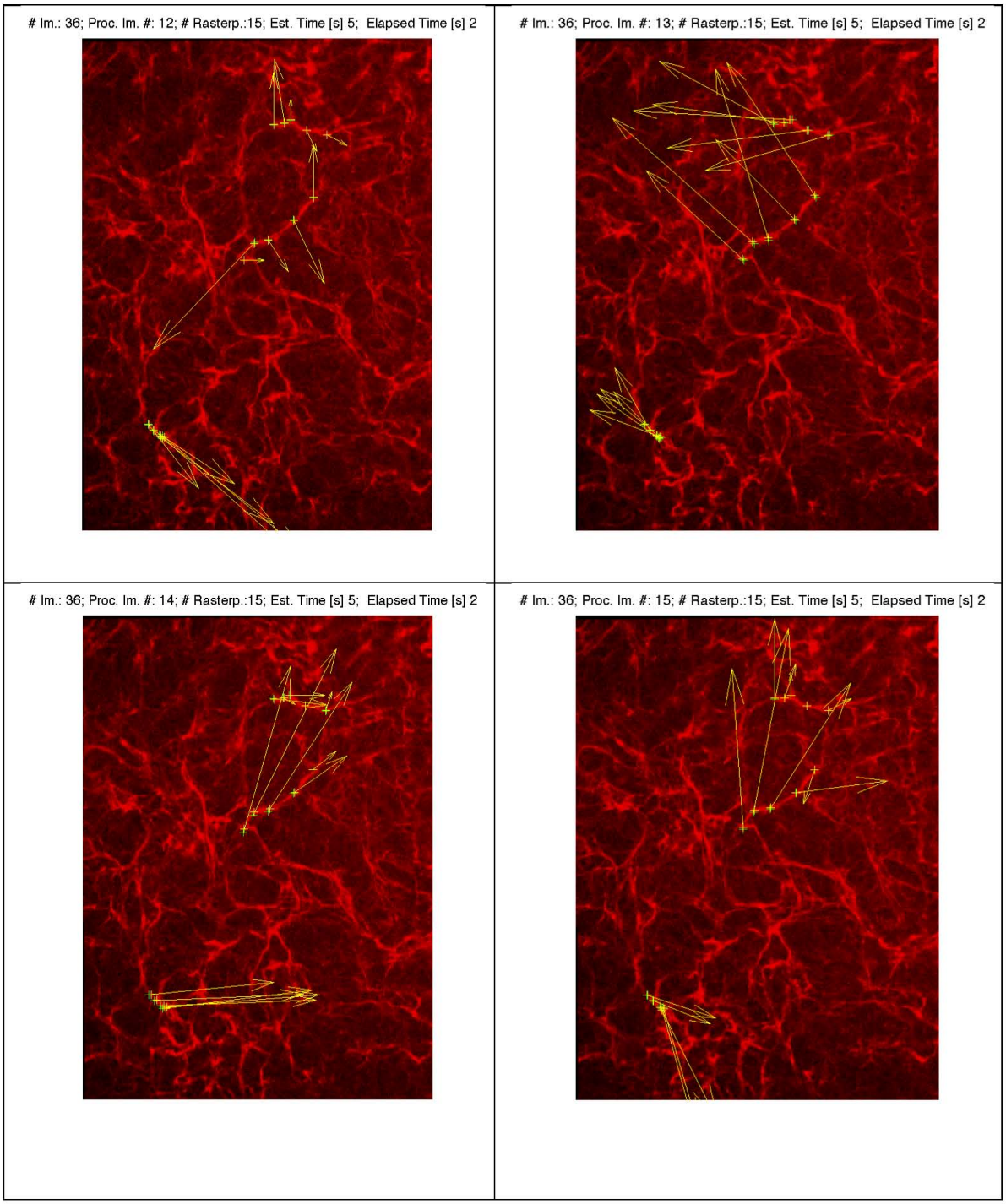
Im.: 36; Proc. Im. #: 12; # Rasterp.:15; Est. Time [s] 5; Elapsed Time [s] 2
Im.: 36; Proc. Im. #: 13; # Rasterp.:15; Est. Time [s] 5; Elapsed Time [s] 2
Im.: 36; Proc. Im. #: 14; # Rasterp.:15; Est. Time [s] 5; Elapsed Time [s] 2
Im.: 36; Proc. Im. #: 15; # Rasterp.:15; Est. Time [s] 5; Elapsed Time [s] 2

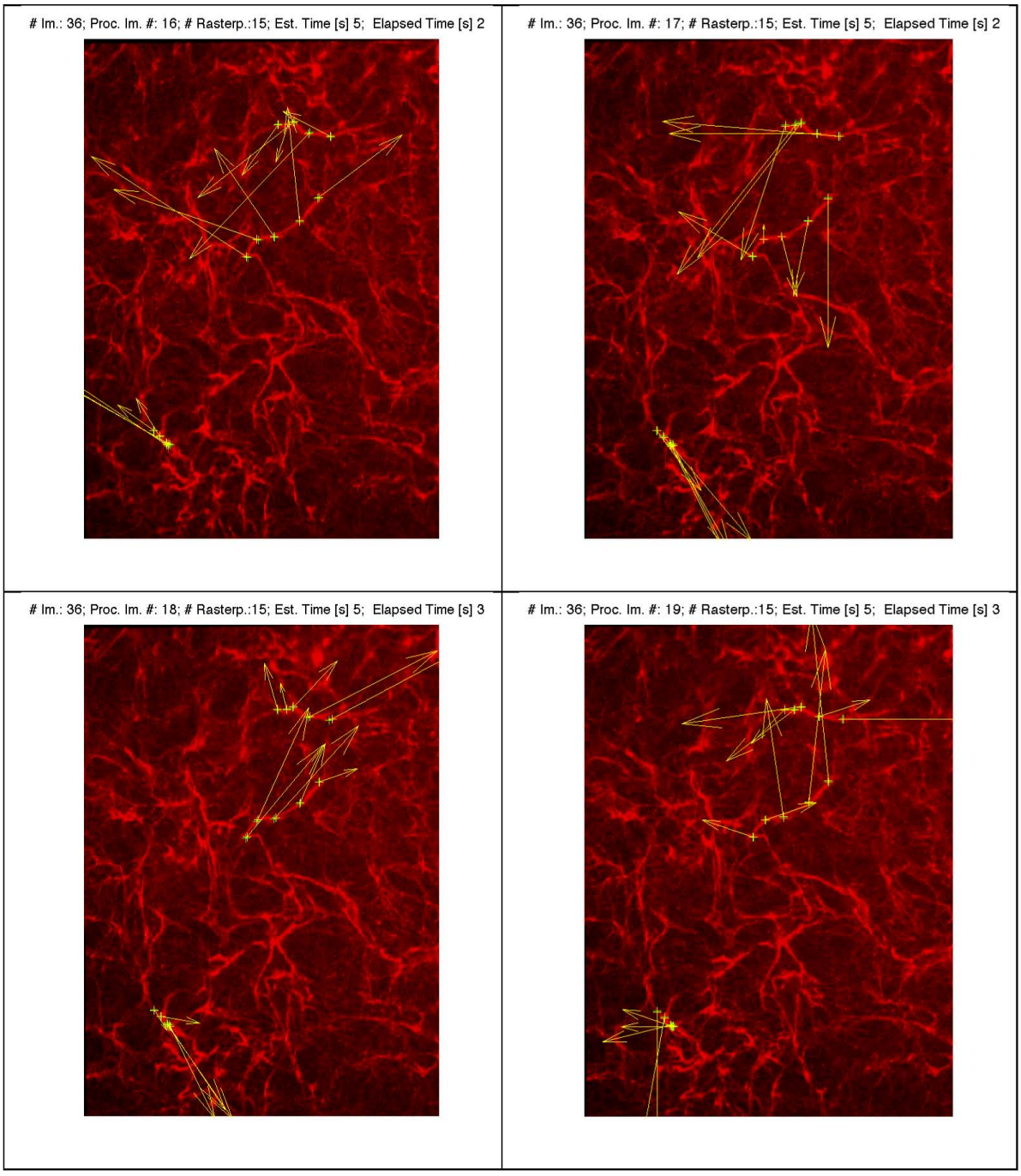
Im.: 36; Proc. Im. #: 16; # Rasterp.:15; Est. Time [s] 5; Elapsed Time [s] 2
Im.: 36; Proc. Im. #: 17; # Rasterp.:15; Est. Time [s] 5; Elapsed Time [s] 2
Im.: 36; Proc. Im. #: 18; # Rasterp.:15; Est. Time [s] 5; Elapsed Time [s] 3
Im.: 36; Proc. Im. #: 19; # Rasterp.:15; Est. Time [s] 5; Elapsed Time [s] 3

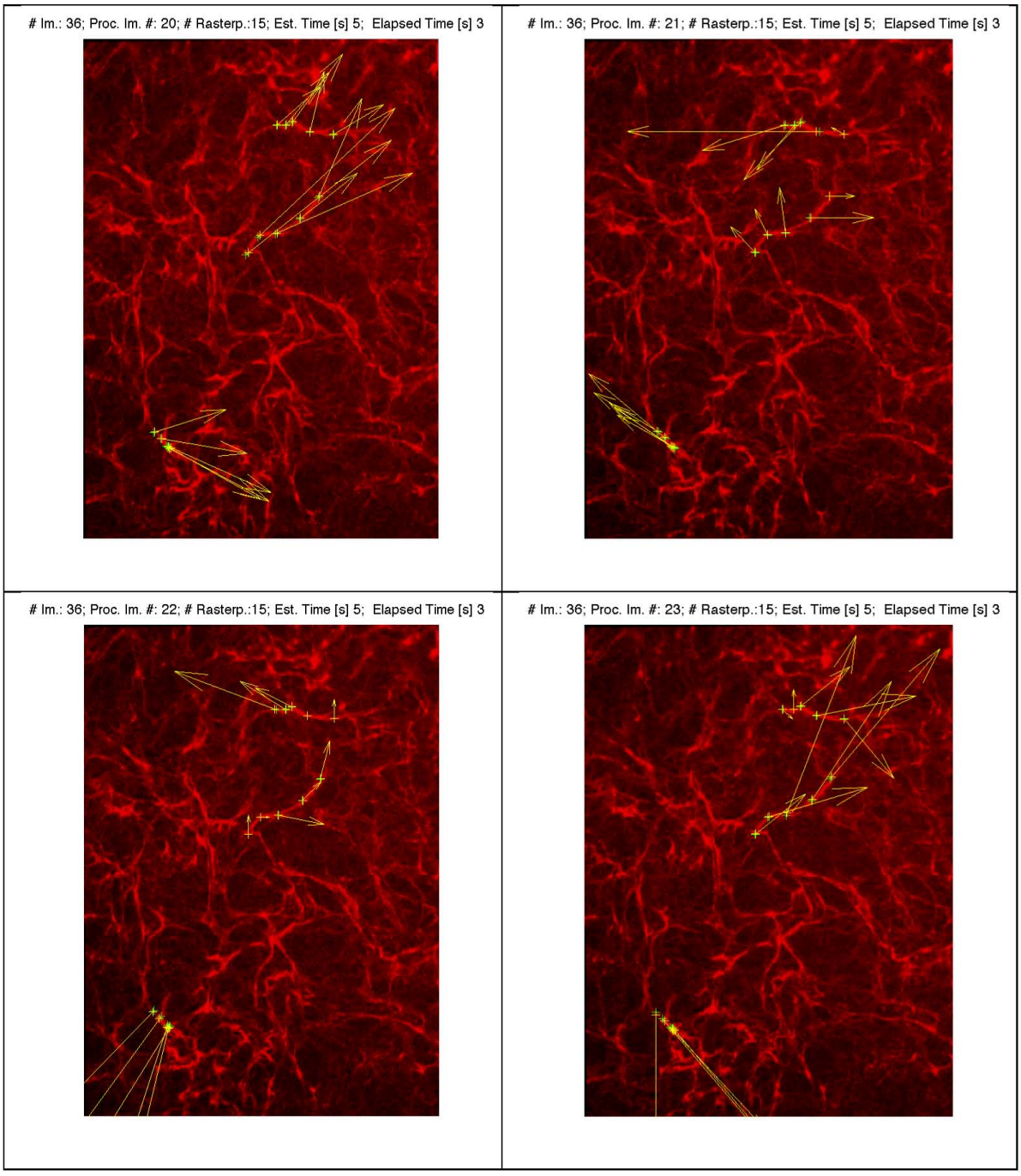
Im.: 36; Proc. Im. #: 20; # Rasterp.:15; Est. Time [s] 5; Elapsed Time [s] 3
Im.: 36; Proc. Im. #: 21; # Rasterp.:15; Est. Time [s] 5; Elapsed Time [s] 3
Im.: 36; Proc. Im. #: 22; # Rasterp.:15; Est. Time [s] 5; Elapsed Time [s] 3
Im.: 36; Proc. Im. #: 23; # Rasterp.:15; Est. Time [s] 5; Elapsed Time [s] 3

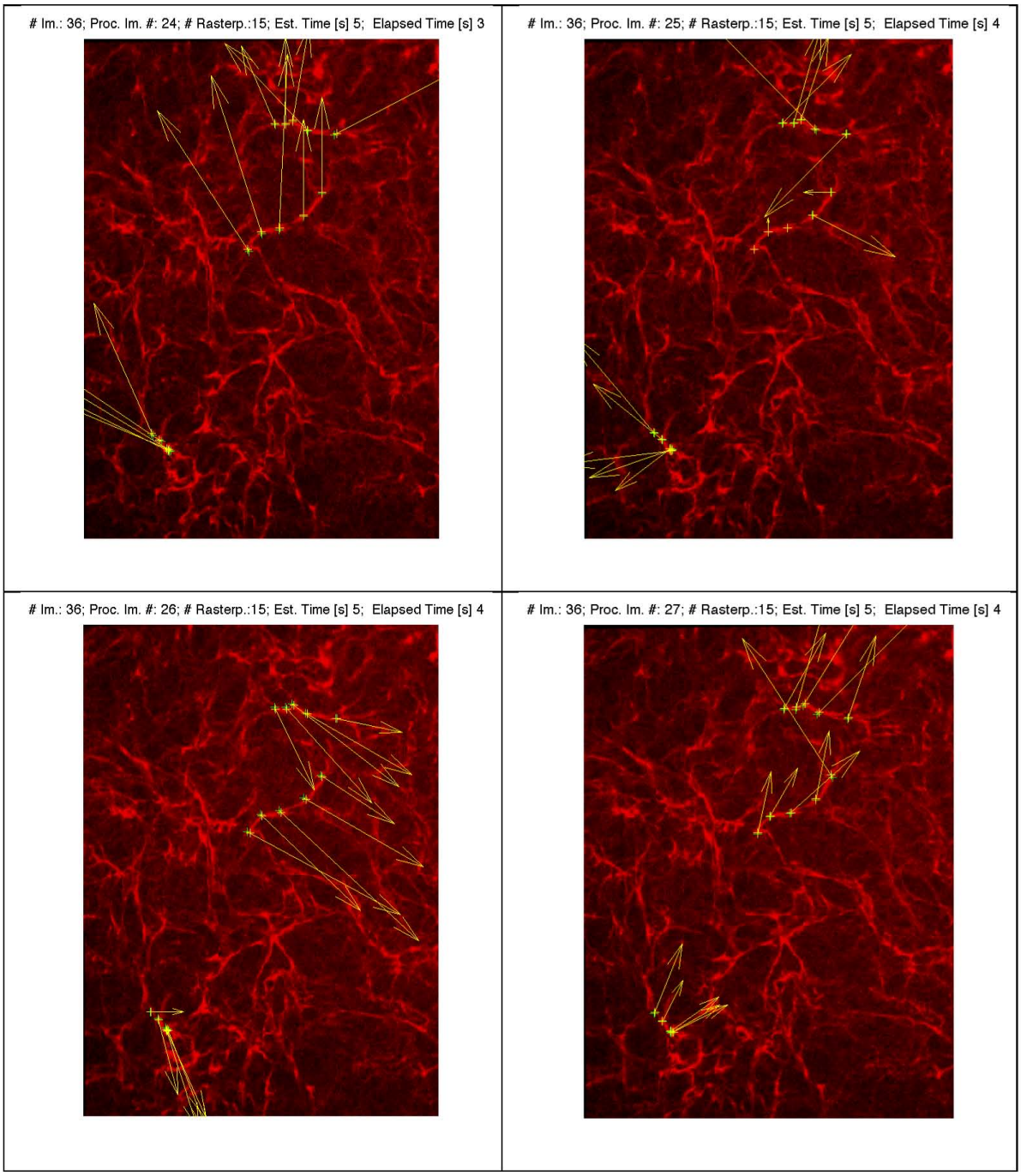
Im.: 36; Proc. Im. #: 24; # Rasterp.:15; Est. Time [s] 5; Elapsed Time [s] 3
Im.: 36; Proc. Im. #: 25; # Rasterp.:15; Est. Time [s] 5; Elapsed Time [s] 4
Im.: 36; Proc. Im. #: 26; # Rasterp.:15; Est. Time [s] 5; Elapsed Time [s] 4
Im.: 36; Proc. Im. #: 27; # Rasterp.:15; Est. Time [s] 5; Elapsed Time [s] 4

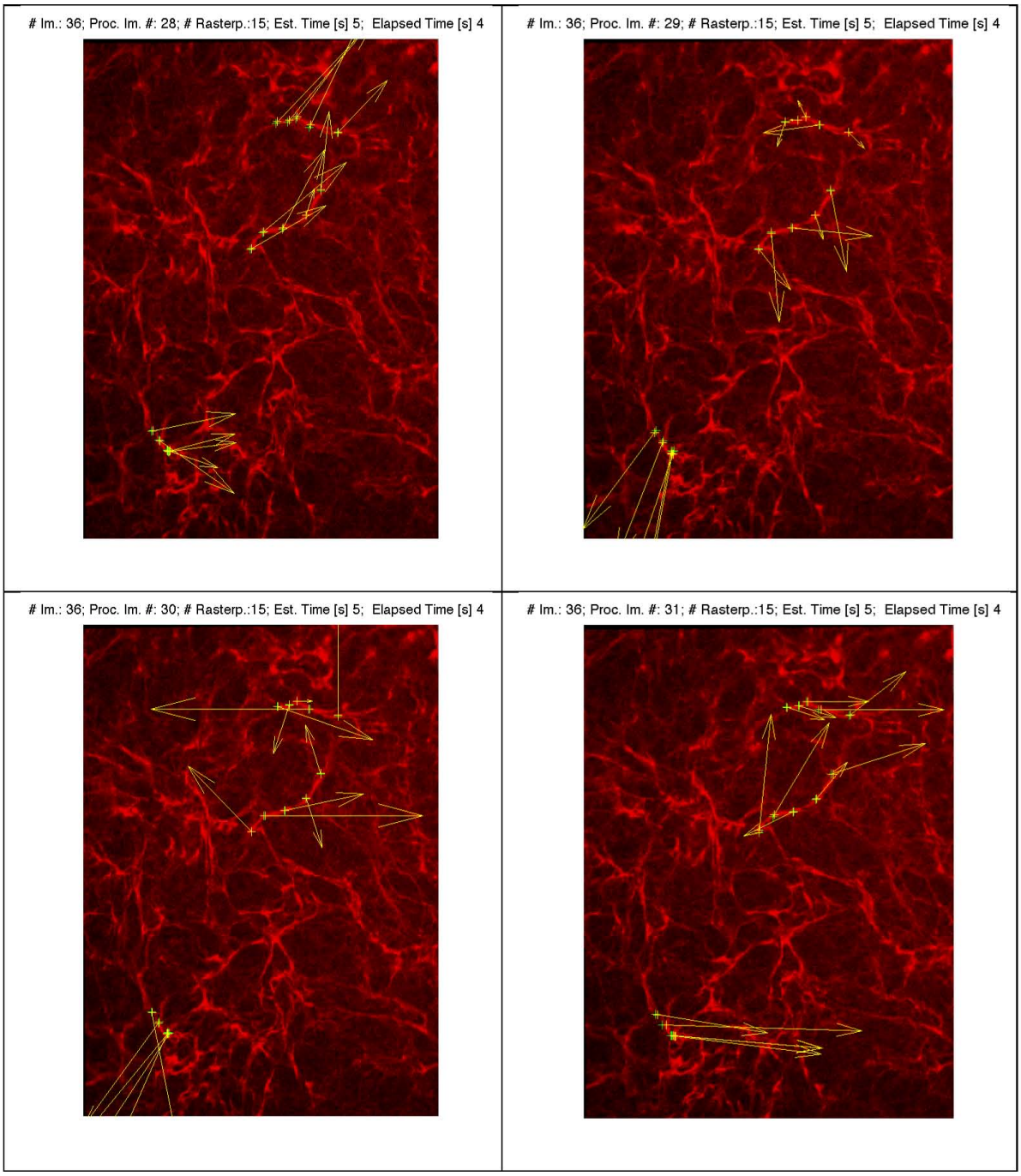
Im.: 36; Proc. Im. #: 28; # Rasterp.:15; Est. Time [s] 5; Elapsed Time [s] 4
Im.: 36; Proc. Im. #: 29; # Rasterp.:15; Est. Time [s] 5; Elapsed Time [s] 4
Im.: 36; Proc. Im. #: 30; # Rasterp.:15; Est. Time [s] 5; Elapsed Time [s] 4
Im.: 36; Proc. Im. #: 31; # Rasterp.:15; Est. Time [s] 5; Elapsed Time [s] 4

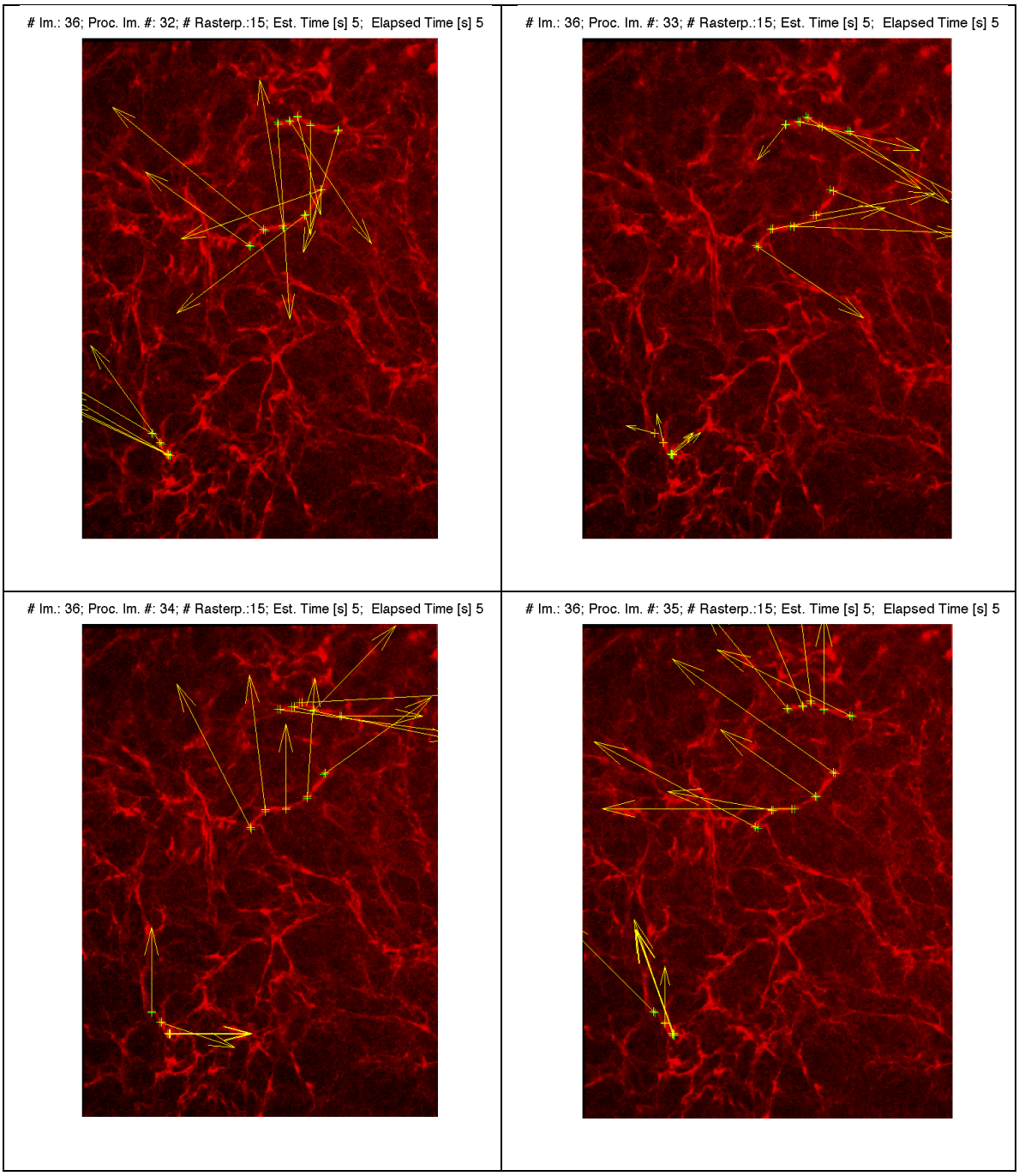

Figure 3.7: The image stack obtained after the execution of automate_image_1.m

3.6.2 Comparison Graphs for images 108-144

After these images were obtained and saved, manual verification of the tracking and manual calculation of the lengths was done using GraphClick. These lengths

were tabulated into an excel sheet and verified with the lengths obtained from Matlab. Below are the graphs showing the differences in the manual and workspline lengths and strains.

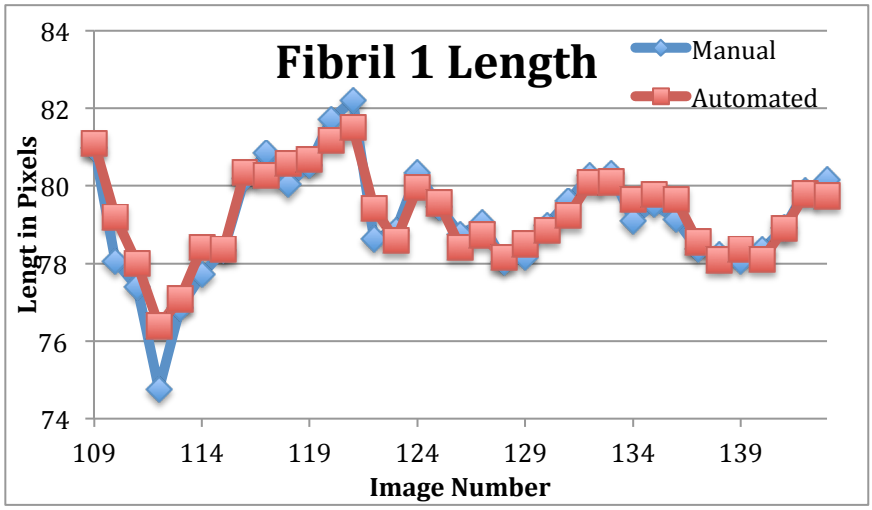

Figure 3.8: A comparison of the manual and automated lengths for Fibril 1

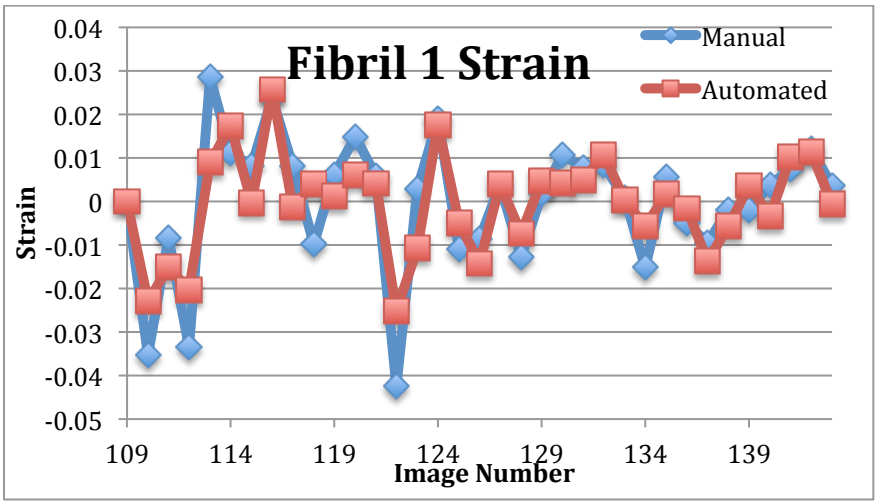

Figure 3.9: A comparison of the manual and automated strains for Fibril 1

The data from the automated measurement gives the maximal tensile strain value experienced by fibril 1 to be 0.0257 at image 116 and the maximal compressive strain value to be -0.0252 at image 122. The average strain experienced by the fibril through all the images in the last 12-hour segment was -0.00036.

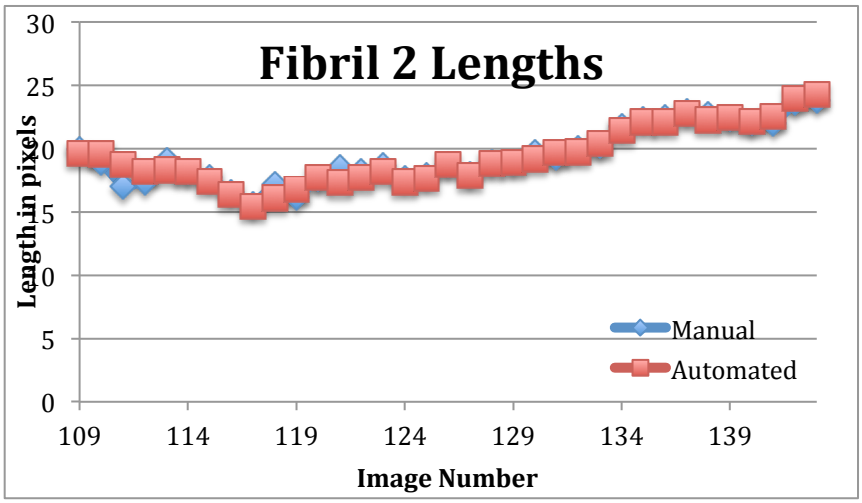

Figure 3.10: A comparison of the manual and automated lengths for Fibril 2

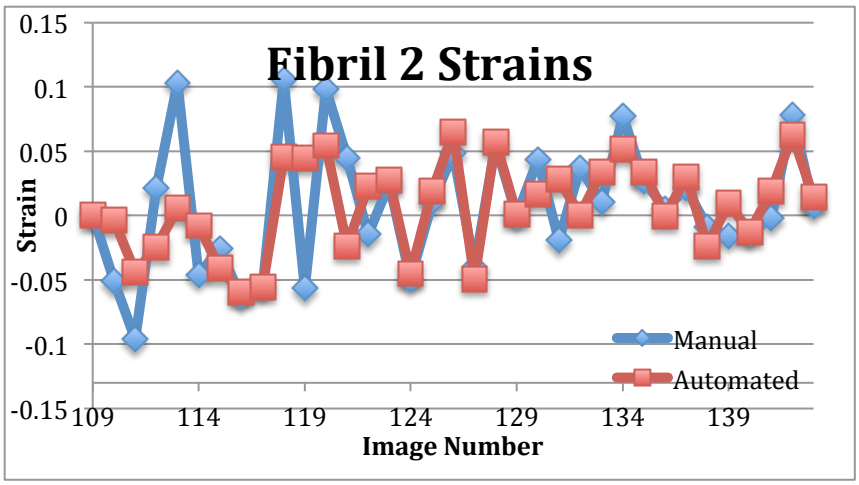

Figure 3.11: A comparison of the manual and automated strains for Fibril 2

This data obtained from the automated analysis of fibril 2 shows that the maximal tensile strain value experienced by the fibril was 0.065 at image number 126 and the maximal compressive strain value was -0.0597 at image number 116. The average strain experienced by the fibril through all the images was calculated to be 0.00753.

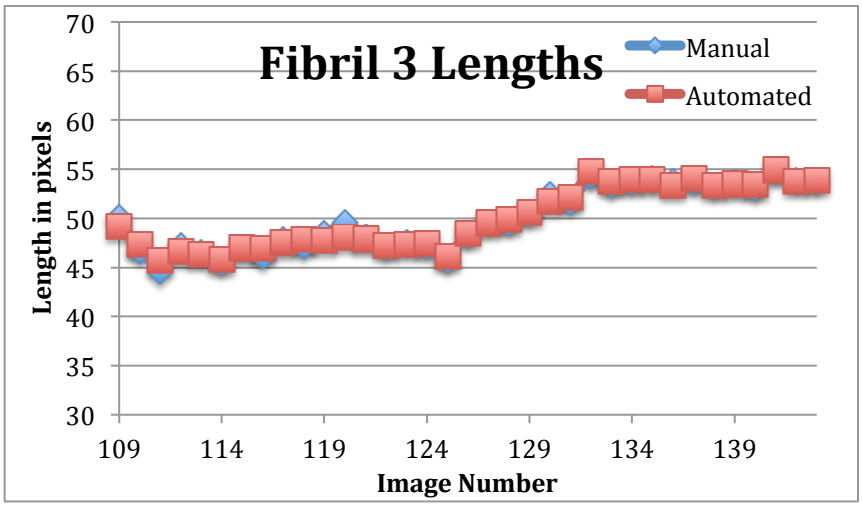

Figure 3.12: A comparison of the manual and automated lengths for Fibril 3

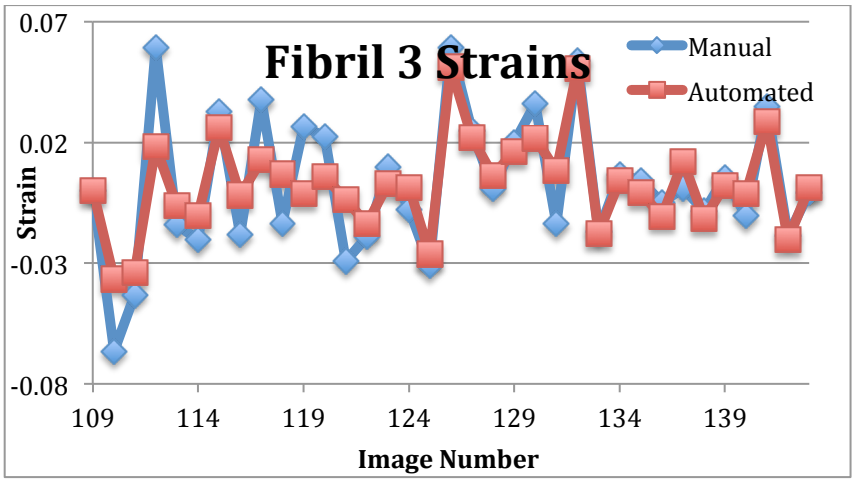

Figure 3.13: A comparison of the manual and automated strains for Fibril 3

From the data obtained from the analysis of fibril 3 it is observed that the maximal tensile strain experienced by the fibril was 0.051 at image number 126 and the maximal compressive strain experienced was -0.036 at image number 110. The average strain experienced has been calculated to be 0.003.

Comparing the average strains of all the three fibrils gives an idea of the amount of cell motion taking place at any given point. A negative strain value suggests the fibrils are experiencing a compressive strain and a positive strain value would suggest a

tensile strain. Overall, the data suggest that the three fibrils each showed their own unique patterns of deformation over time – i.e. all three fibrils experienced different motions and they also differed in the amount of strains experienced due to these motions. Even in a particular fibril all the raster points do not move in the same direction. This further suggests that the underlying cell motion is not uniform and every fibril is constantly subjected to deformations, involving both compressive and tensile strains, in multiple directions due to this motion. As observed the automated tracking of the raster points appeared to faithfully track with the fibril (i.e. the raster points were never observed to be "off fibril") and the lengths measured with the automated tracking were close to the manually calculated lengths. The reasons for the small difference between the lengths are due to the fact that it is harder to manually place a marker on a raster point especially if the motions are very small. This could lead to a difference of a few pixels per raster point which over a sum of 5 raster points may cause a bigger difference. Another interesting observation was that while the manual strain values seemed to be following a similar pattern as the strain values from the automated process, the values themselves seemed to somewhat magnified. This can also be attributed to the errors incurred during the manual analysis. The formula used to calculate strain is sensitive to small variations in the lengths of the fibrils. Thus small differences in the length of the fibril, determined from manual vs. automated positioning of raster points could lead to a larger difference in strain values. Since most raster points move only by a few pixels in every image even a difference of about 2-5 pixels is sufficiently large to create a difference.

3.6.3 Precision Analysis using images 108-144

Since the placement of the raster points plays a vital role in the accuracy of the final result, analyzing the variations in results based on a change in the position of the raster points would provide a better idea of the precision of the DIC algorithm. This analysis was done in 2 parts

1) Comparing the results of the algorithm by running it three times without changing the positions of the raster points.
2) Comparing the results of the algorithm by running it three times while changing all but the two end-most raster points on each side.

These are described in detail below.

For the first part, the algorithm was run on a fixed set of points three times to verify the consistency of the results. Any variations in the results would mean that the algorithm provided multiple solutions to a same set of variables thus raising doubts over its accuracy.

This analysis was performed over images 108-144 using length and strain data from the same 3 fibrils of varying lengths that was used in the manual versus automated comparison analysis described in the above section. Figures 3.14 through 3.19 show the comparison graphs obtained at the end of this analysis.

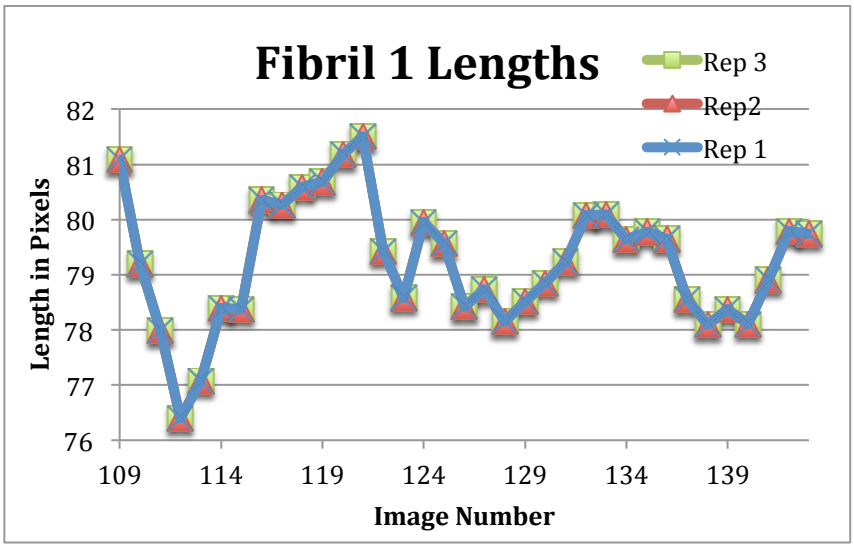

Figure 3.14: A comparison of three repetitions of length calculations for Fibril 1

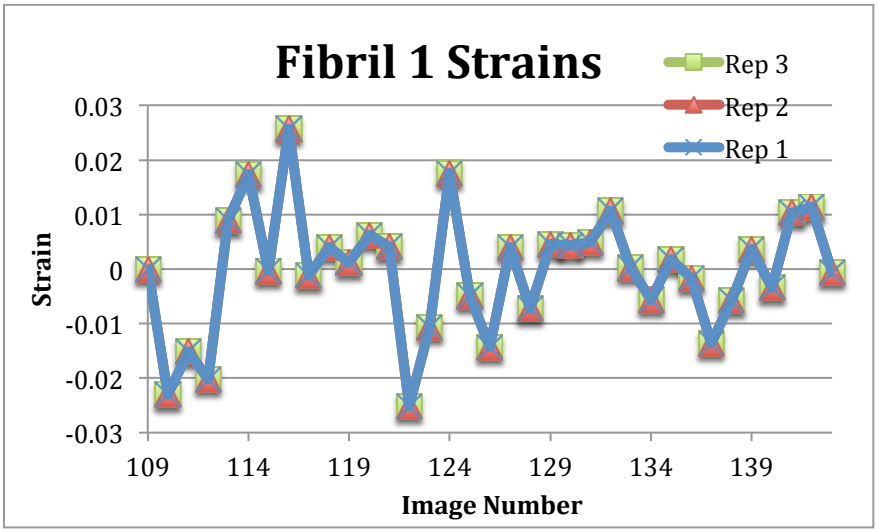

Figure 3.15: A comparison of three repetitions of strain calculations for Fibril 1

The results from Figure 3.14 and 3.15 show that the length and strain values are completely overlapping with an error of 0%, thus suggesting that the values remained constant on all three repetitions of fibril 1.

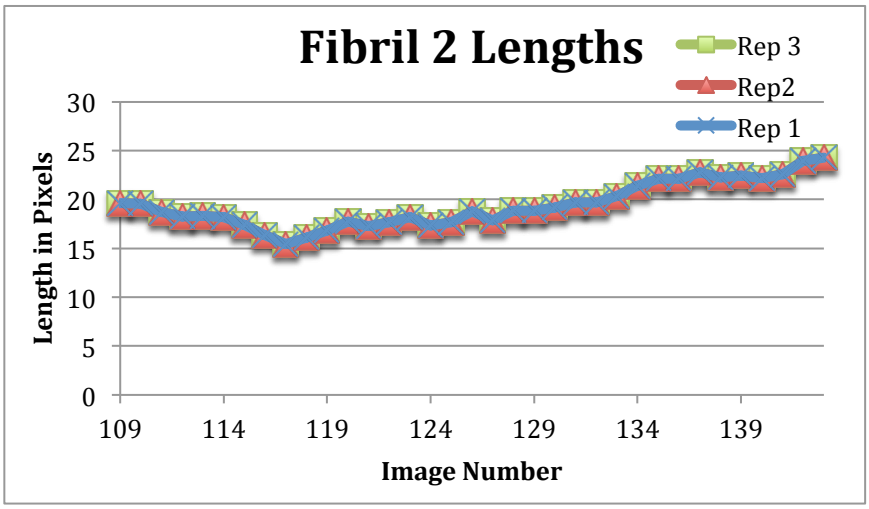

Figure 3.16: A comparison of three repetitions of length calculations for Fibril 2

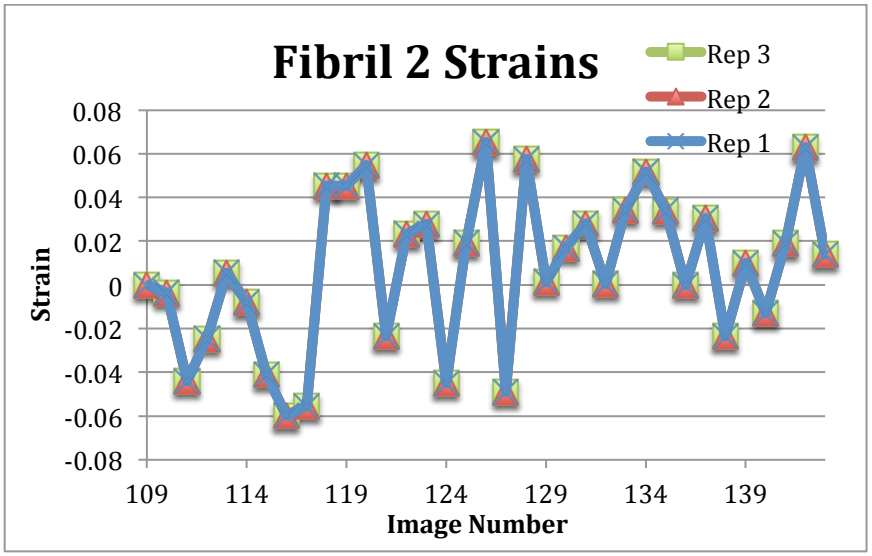

Figure 3.17: A comparison of three repetitions of strain calculations for Fibril 2

The results obtained from the analysis of fibril 2 also show an error of 0% thus suggesting that a constant value for the length and strain is obtained for a constant set of the raster points.

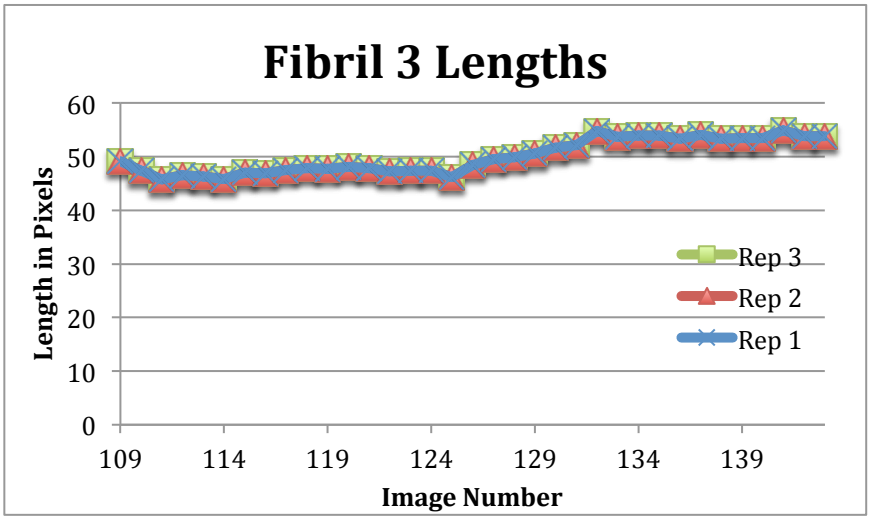

Figure 3.18: A comparison of three repetitions of length calculations for Fibril 3

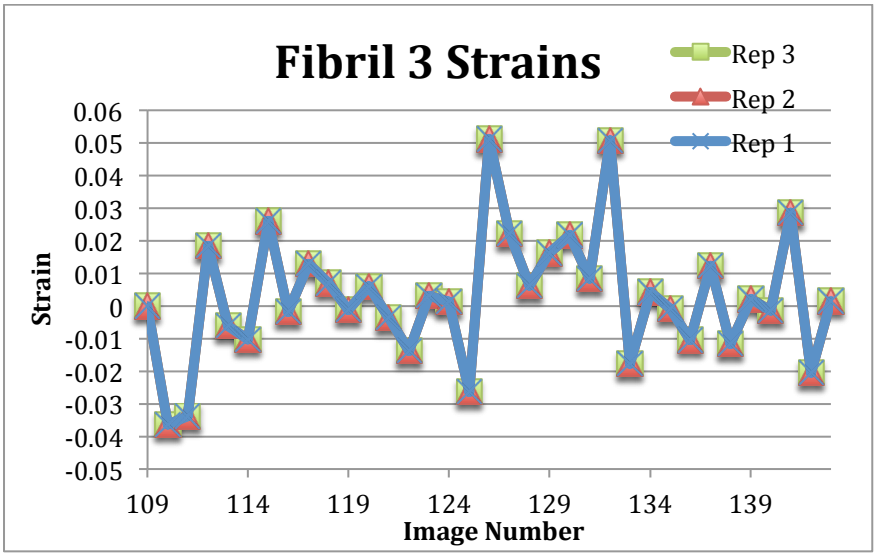

Figure 3.19: A comparison of three repetitions of strain calculations for Fibril 3

The third fibril also showed an overlap in the length and strain values through all the images with an error of 0%, thus suggesting that a unique result is obtained for a fixed set of raster points.

These results suggest a high precision when the raster points are unchanged. This means that for any given set of raster points, the DIC analysis of the displacements and strains always gives the same result, suggesting that there is no variation in the way the algorithm runs.

After a high precision was suggested by the above analysis, a second analysis was done to further estimate the precision of the algorithm if the raster points were changed. To do this the algorithm was run on the same set of fibrils while keeping the end-most raster points at each end constant and varying the positions of the raster points in the middle of the fibril. This was done three times and the length and strain values obtained were then compared. The results of this comparison are shown in Figures 3.20 through 3.25.

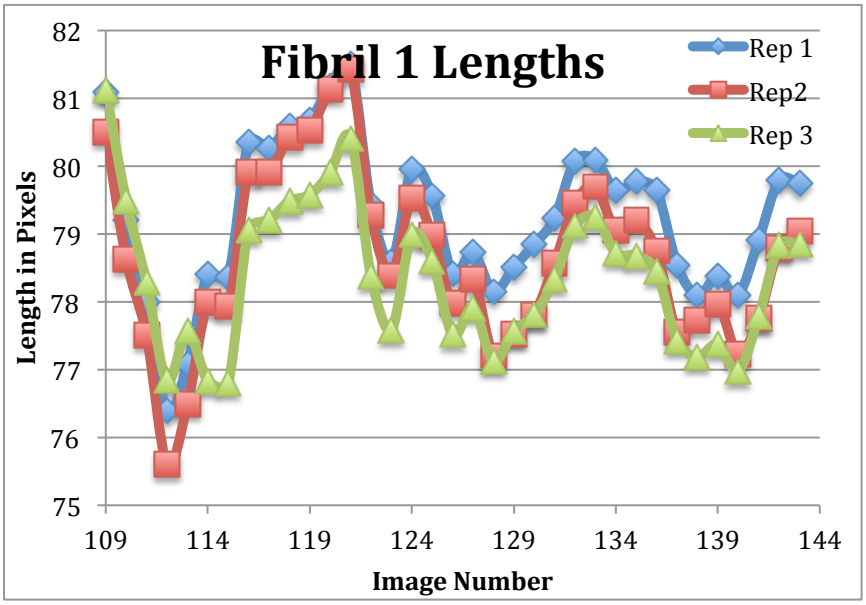

Figure 3.20: A comparison of three repetitions of length calculations for Fibril 1

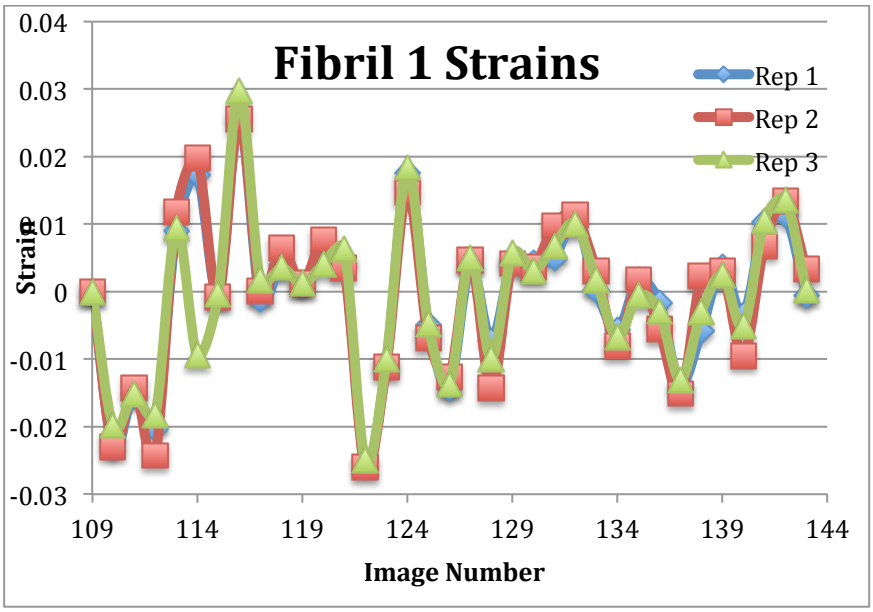

Figure 3.21: A comparison of three repetitions of strain calculations for Fibril 1

The results from the analysis of fibril 1 show some deviations in the actual lengths of the fibril in all the three repetitions but the pattern of the changes in length as a function of time (i.e. the relative change in the length of the fibril between image pairs) appears very similar. The average maximum error in the lengths of the fibril obtained during the three repetitions was calculated to be 1.69%. The maximum standard deviation was calculated to be 0.815 pixels. The strain values of the fibril also appear very similar between the three repeat runs, confirming that the relative changes in length of the fibril between image pairs is preserved, even though there are differences in the absolute values.

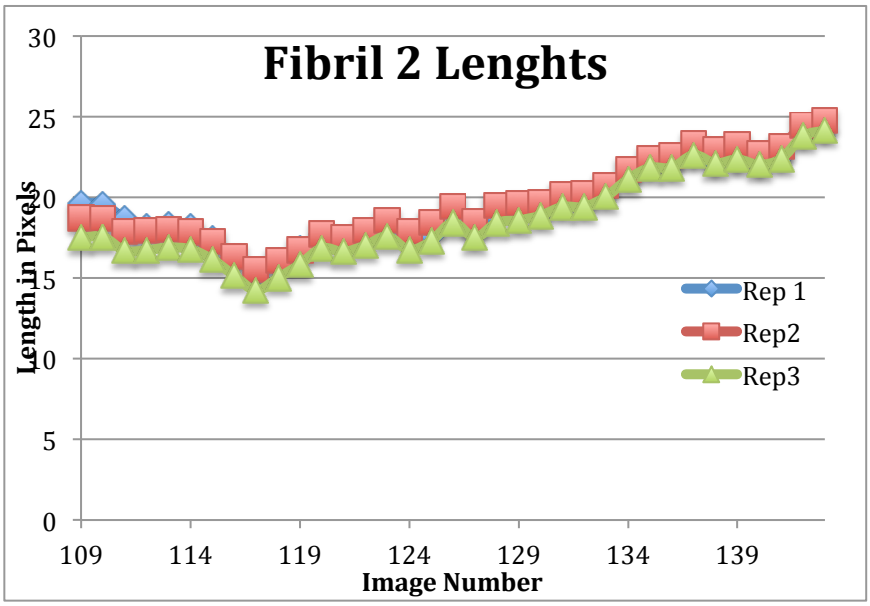

Figure 3.22: A comparison of three repetitions of length calculations for Fibril 2

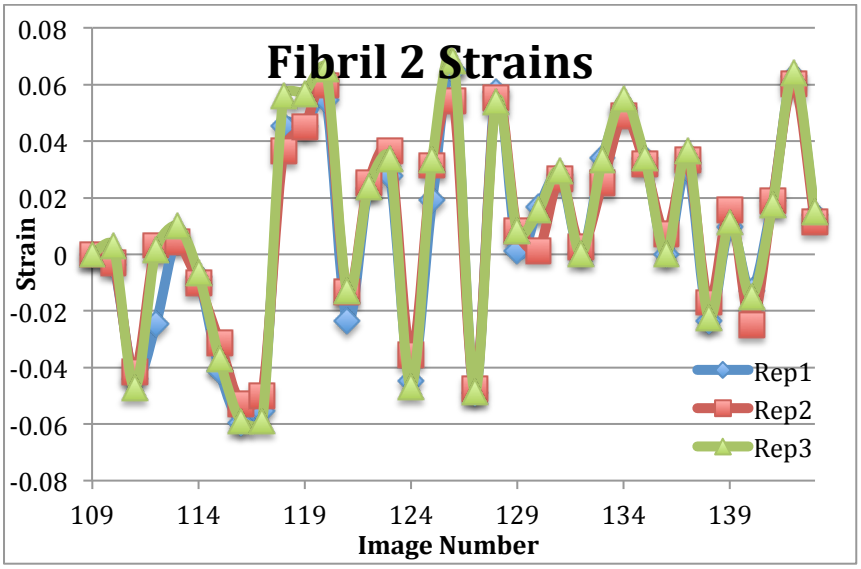

Figure 3.23: A comparison of three repetitions of strain calculations for Fibril 2

As, with fibril 1, the results from the analysis of fibril 2 also show a small variation in the lengths of the fibril but the strain values seem to be very close and overlapping most of the time. The average maximum error between the lengths obtained during all three trials was calculated as 7.89%. The maximum standard deviation was calculated to be 1.08 pixels.

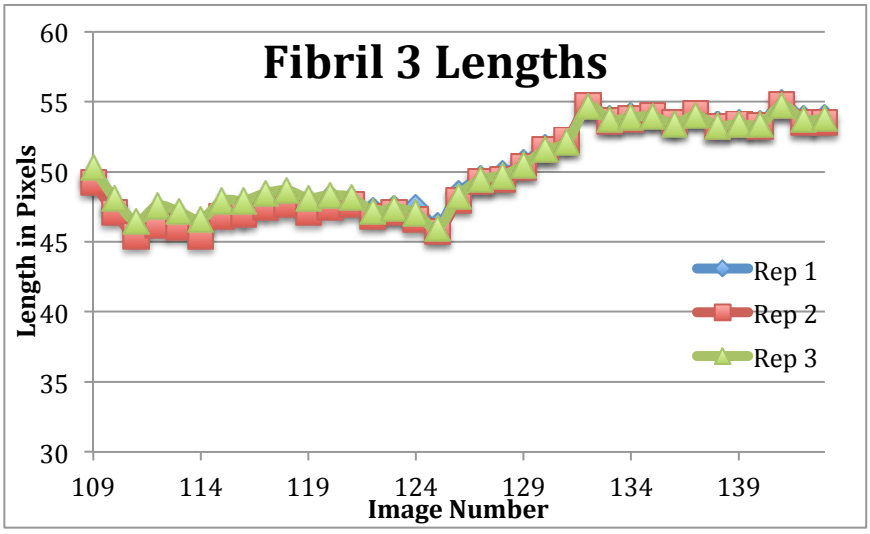

Figure 3.24: A comparison of three repetitions of length calculations for Fibril 3

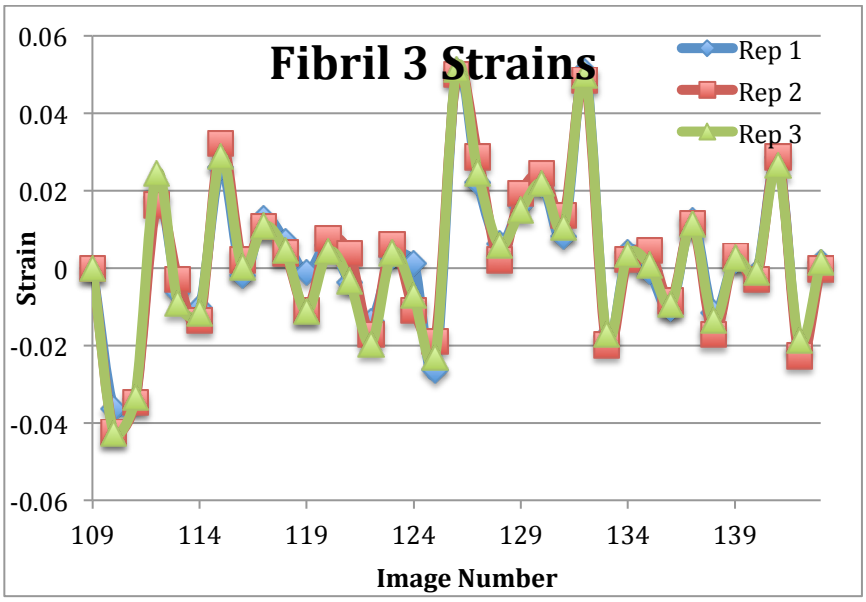

Figure 3.25: A comparison of three repetitions of strain calculations for Fibril 3

The third fibril showed very little variation in the lengths between the three repetitions and the strain values seemed to be overlapping through almost all the images. The average maximum error between the lengths of all three trials was calculated as 2.27%. The maximum standard deviation was calculated to be 0.72 pixels.

The results from this analysis suggest that a change in the positions of the internal raster points leads to some variation in the absolute length of the fibril. The reason for this it that since the length of a fibril is calculated by adding up the sum of the shortest distances (i.e. a straight line path) between two consecutive raster points, inefficient placement of the raster points leads to some portions of the fibril (which maybe curved) to be ignored.

Another interesting observation that can be made from this analysis is that while a slight variation exists in the lengths of the fibrils, the strain values tend to follow more or less the same pattern. Since a strain is an indication of the pattern of deformation of the fibril, this would suggest that even though the lengths may differ the algorithm continues to recognize a fixed pattern of deformation when executed all the three times. In each of the fibrils the maximum error stayed at an average of 3.95%. This further suggests a high level of precision from the algorithm.

3.6.4 Raster Point Density Analysis

To further understand the effectiveness of the code, another analysis was performed on the same set of three fibrils, from the image segment 108-144, that have been used in all the earlier analyses. As a part of this analysis the number of raster point used to define the length and, hence, its motion was varied between 3,5,7 and 10 raster points and their results were compared. This comparison is aimed at determining the effect of varying the raster points on the tracking efficacy. Such an analysis would provide valuable information about the optimum number of rasterpoints required per fibril and also help understand the machine errors, if any, that would affect the final result.

The analysis started off with running the algorithm with 3 raster points on each fibril followed by 5,7and then finally 10 raster points. The three fibrils that were analyzed varied in their lengths and, thus, each iteration affected every fibril differently. Once the algorithm was run and all the length and strain values were obtained, they were organized in an excel sheet and the comparison graphs were generated. Figures 3.26 to 3.31 depict these comparison graphs.

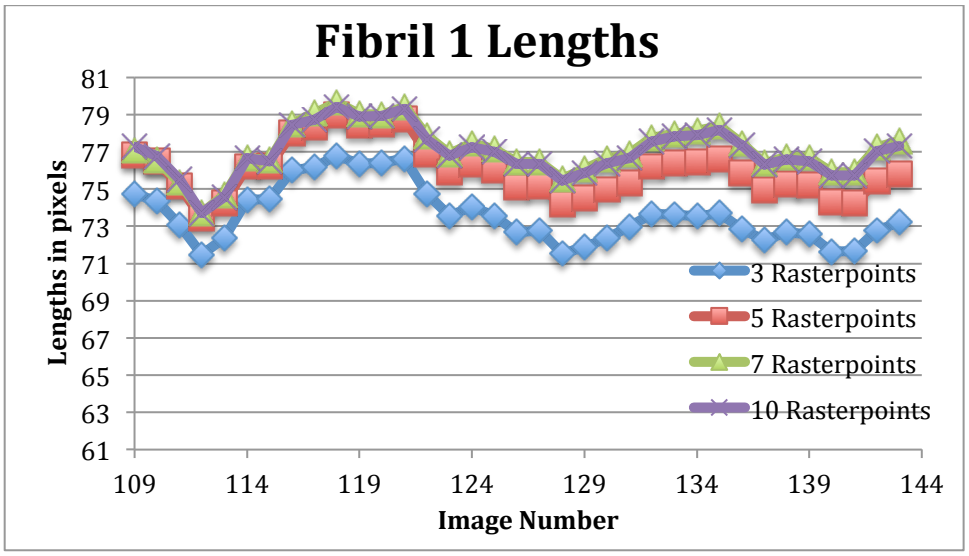

Figure 3.26: A comparison of the lengths of four different raster point density analyses on fibril 1

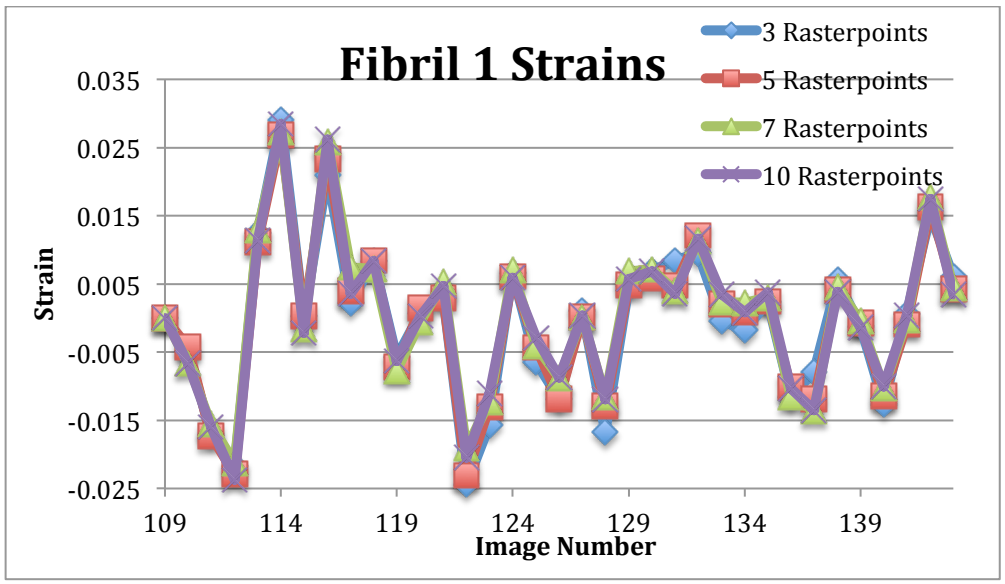

Figure 3.27: A comparison of the strains of four different raster point density analyses on fibril 1

The graphs above depict the length and strain comparisons of different raster point densities on fibril 1. Fibril 1 was the longest of the three fibrils and while the results of all the iterations seemed to be in close correlation to each other, it is noteworthy that the results of the analysis using 3 raster points seems to be the most distant from the other three analysis. The reason for this could be that since only 3 raster points were used to define this fibril, more portions of the fibril tended to be ignored and hence the effective length of the fibril was subsequently lesser than any of the other three analyses. The lengths of the fibril also seemed to be increasing, , albeit slightly, as the number of raster points increased. This could also be attributed to more nonlinearities in the fibril being accounted for as the density of the raster points increased. The results of the iteration with 7 raster points and 10 raster points seems to almost completely coincide, which would suggest that the iteration with 7 raster points seemed to have covered all the nonlinearities along the fibril and so the iteration with 10 raster points failed to provide any more resolution to the analysis. In each of the analysis the amount of change in length in the fibril seemed to be the same and this is the reason the strains, shown in figure 3.27, were almost the same in every case.

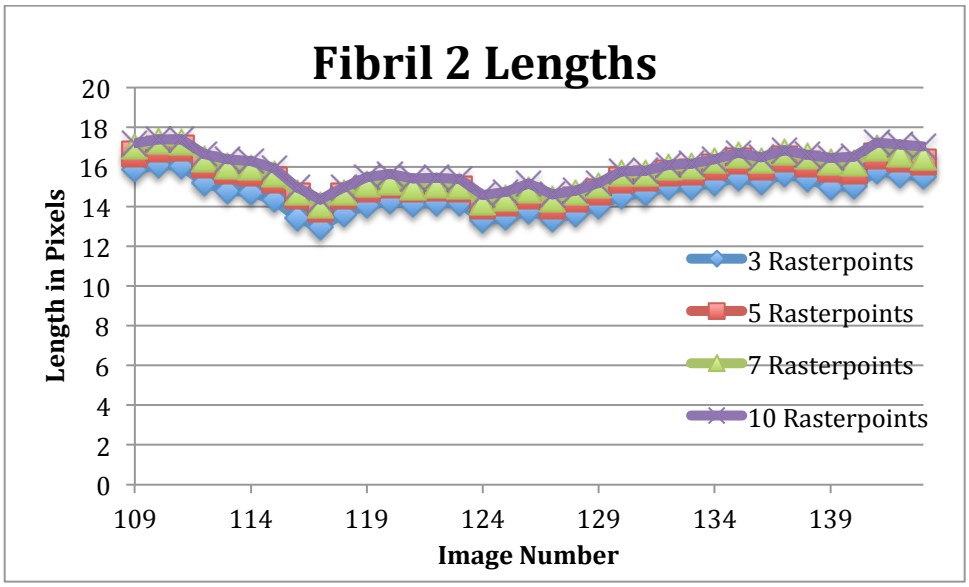

Figure 3.28: A comparison of the lengths of four different raster point density analyses on fibril 2

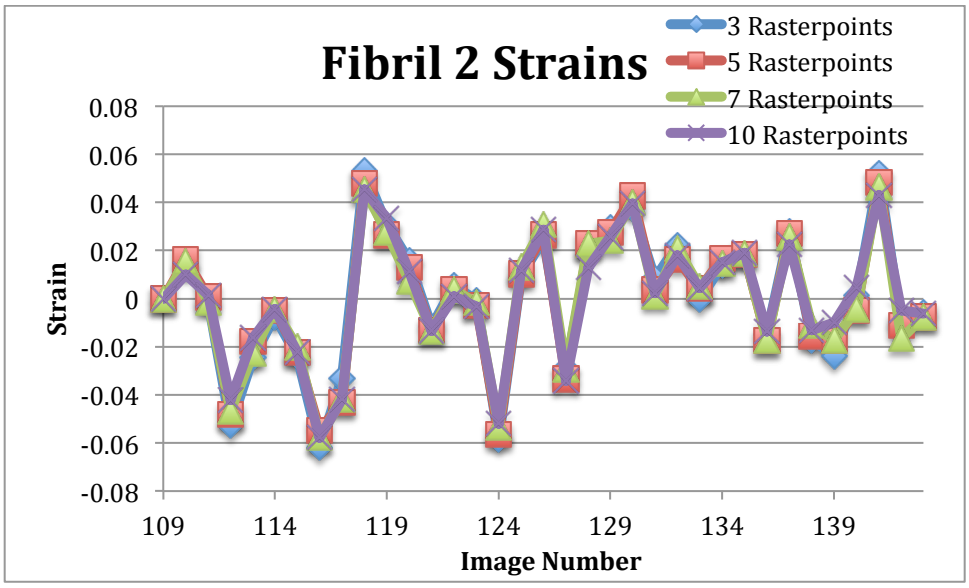

Figure 3.29: A comparison of the strains of four different raster point density analyses on fibril 2

The graphs above depict the length and strain comparison graphs of fibril 2. Fibril 2 was the shortest of the three fibrils. Here too a huge similarity and close correlation was observed between each of the iterations. The similarity between the results of the iterations seemed to be closer than that observed in fibril 1. A possible explanation could be the size of

the fibril. Since the fibril was much smaller than fibril 1, the nonlinearities in the fibril were lesser and thus even 3 raster points could cover most of those nonlinearities in this fibril. As with the previous fibril, there appeared to be a very slight increase in the length of the fibril as the number of raster points increased. The change in length of the fibril seemed to remain constant through all the iterations, which was confirmed by the strain graphs almost completely overlapping over one another.

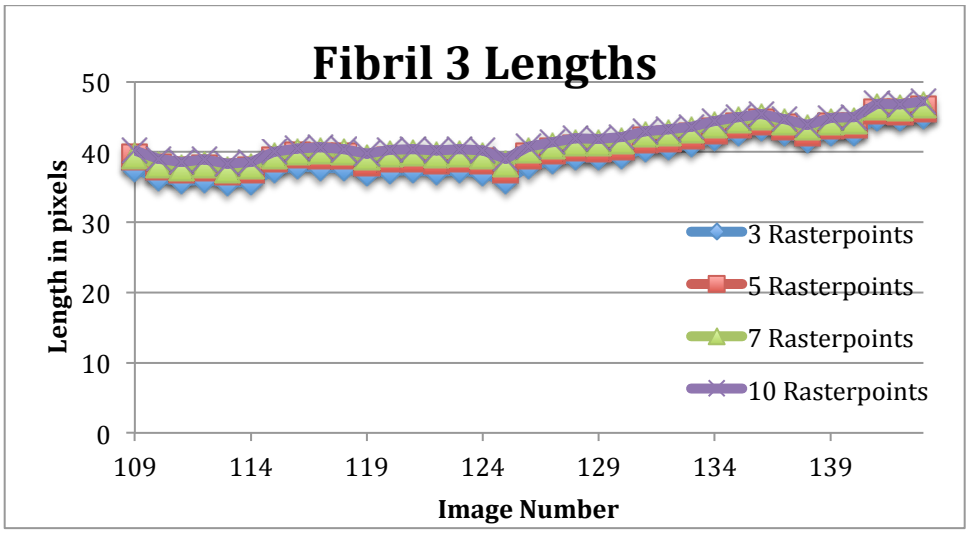

Figure 3.30: A comparison of the lengths of four different raster point density analyses on fibril 3

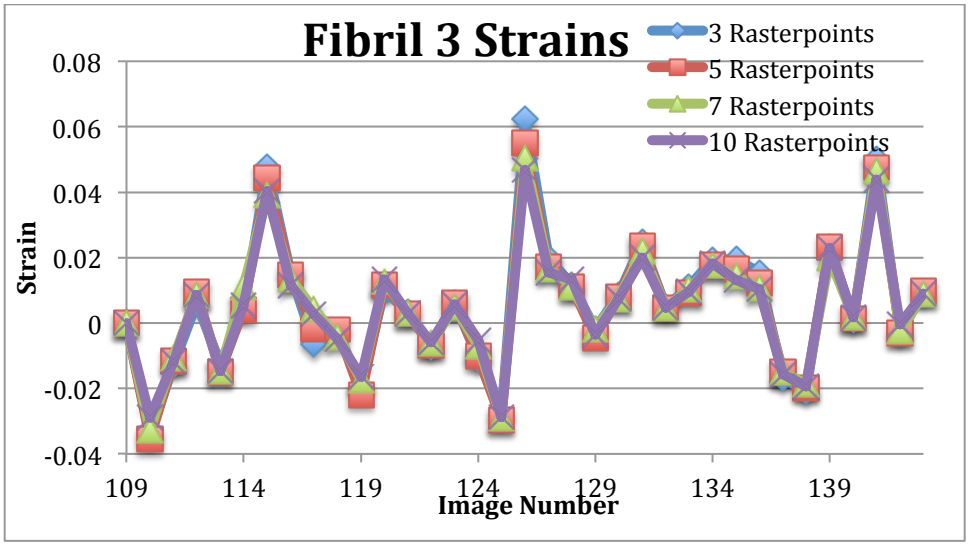

Figure 3.31: A comparison of the strains of four different raster point density analyses on fibril 3

The above graphs depict the length and strain comparison graphs of fibril 3. Fibril 3 had a length that was in between the values of fibril 1 and fibril 2. The results of all the iterations seemed to be very close to one another suggesting that 3 raster points had, largely, considered the nonlinearities in the fibril. Again, as with the other 2 fibrils, we saw a very slight increase in lengths with the number of raster points. Also the change of lengths remained constant through all the iterations, as depicted by the strain graphs, which almost completely overlapped each other.

All these results from this analysis suggest that as the number of raster points that define a fibril increase, the ability of the code to track the nonlinearities of the fibrils increase as well, thus providing a better estimate of the true length of the fibril. However not much change was seen in the strains of the fibril suggesting that even if the length of the fibril wasn't accurate, the algorithm still had the capability to effectively calculate the strains experienced by the fibril.

3.6.5 Images from 72-108 (Segment 3)

Having performed the DIC analysis on images 108-144, to further analyze the functionality of the program, we next analyzed the stack of images taken during the third 12-hour segment of the movie (24-36 hour) i.e. images 73 to 108. Biologically, this segment is more challenging to quantify because many new fibronectin fibrils are still being formed and this causes new features to emerge continuously. Also the motions experienced by the fibrils are larger than those observed in the last 12 hour segment. Thus to improve the efficacy of the tracking, the search window in the function *cpcorr* which is defined by the variable *corrsize* was changed from the default value 5 to a new value of 10. This step was necessary

because the motion between two consecutive images was so large that the fibril features of interest were continuously moving out of the search window, thus leading to erroneous tracking. In some cases this caused the raster points to remain on the fibril but merge with adjacent raster points, again leading to erroneous results. The increase in the size of the search window helped to widen the area around the raster point where the feature being tracked could be found, thus giving better correlation values that lead to more effective tracking. Below are the results of the analysis of the 24-36 hour movie segment with the changed *corrsize*.

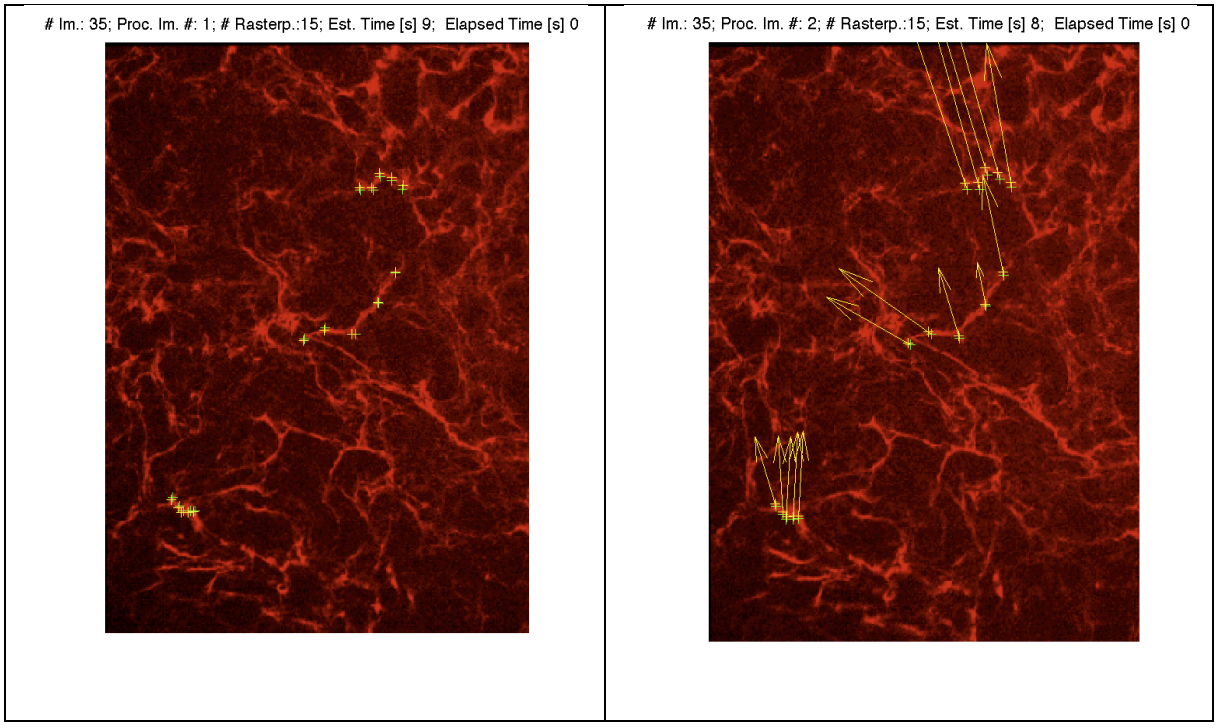

Im.: 35; Proc. Im. #: 3; # Rasterp.:15; Est. Time [s] 8; Elapsed Time [s] 1

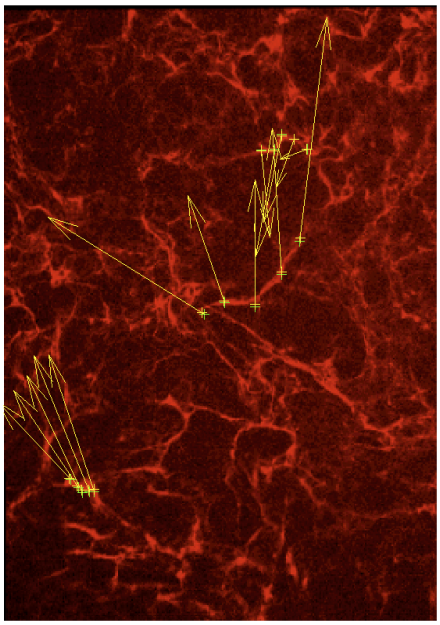

Im.: 35; Proc. Im. #: 4; # Rasterp.:15; Est. Time [s] 8; Elapsed Time [s] 1

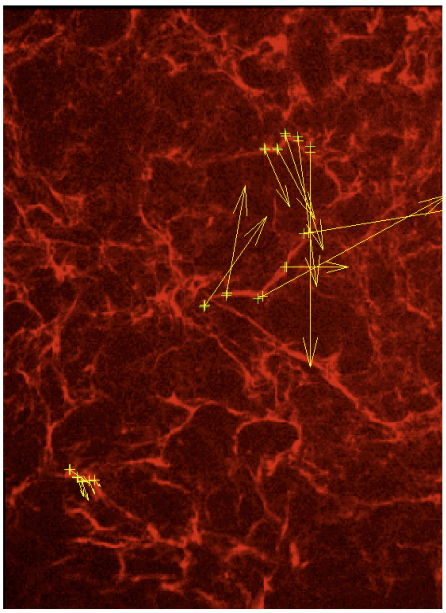

Im.: 35; Proc. Im. #: 5; # Rasterp.:15; Est. Time [s] 8; Elapsed Time [s] 1

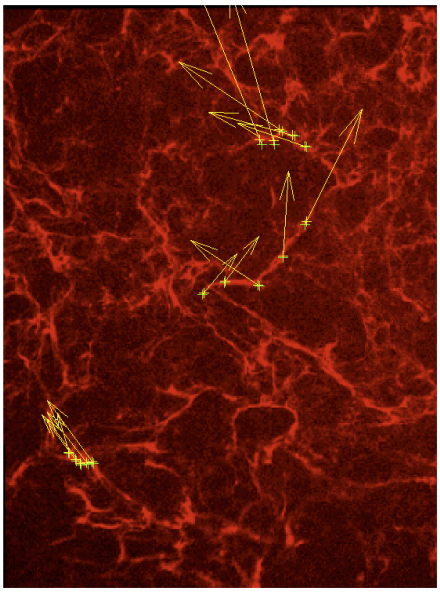

Im.: 35; Proc. Im. #: 6; # Rasterp.:15; Est. Time [s] 8; Elapsed Time [s] 1

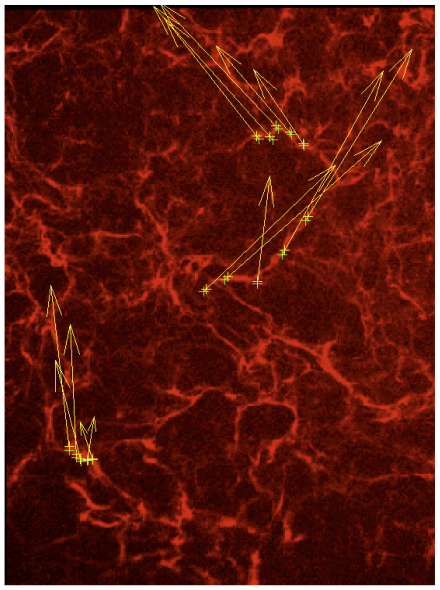

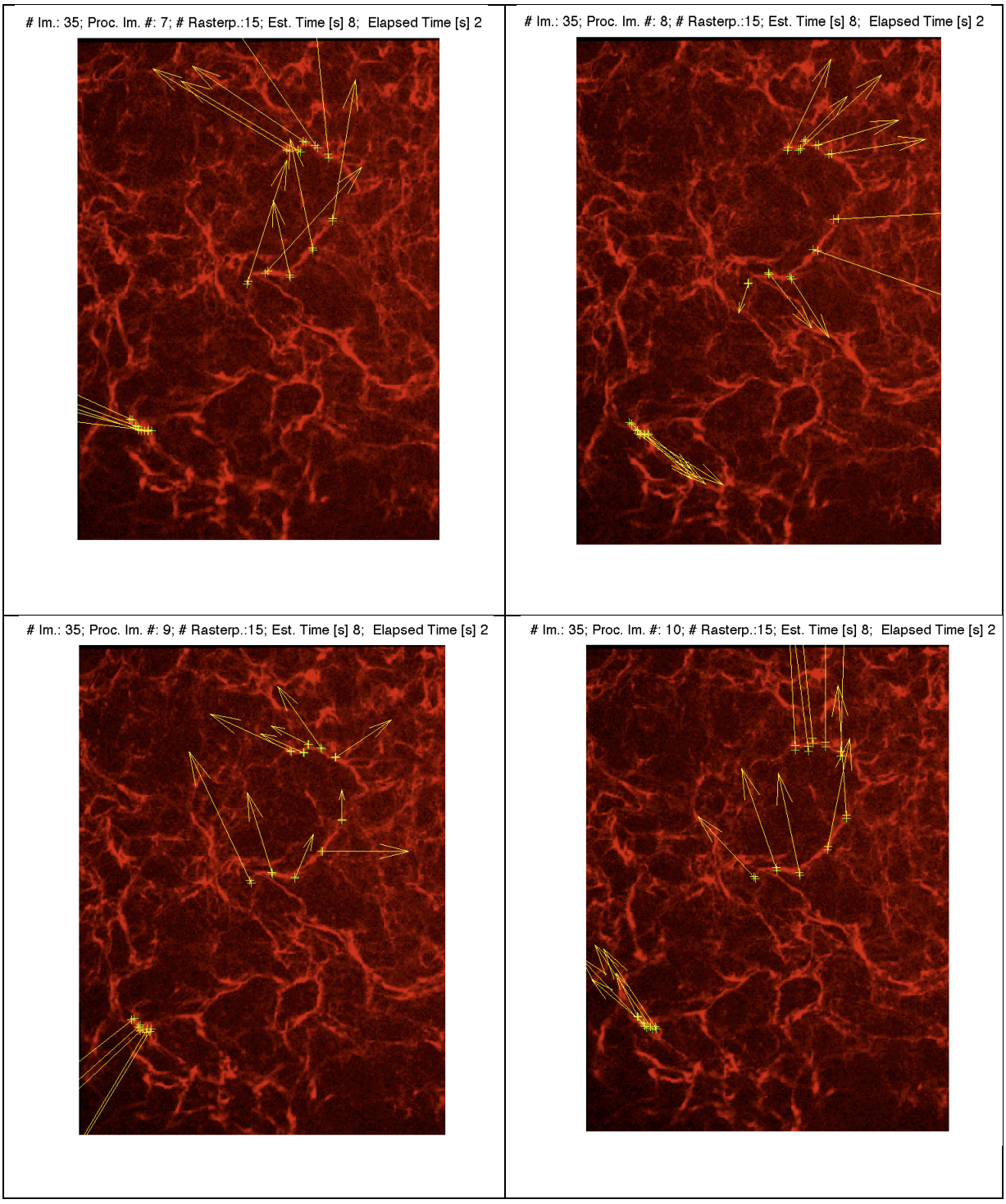
Im.: 35; Proc. Im. #: 7; # Rasterp.:15; Est. Time [s] 8; Elapsed Time [s] 2
Im.: 35; Proc. Im. #: 8; # Rasterp.:15; Est. Time [s] 8; Elapsed Time [s] 2
Im.: 35; Proc. Im. #: 9; # Rasterp.:15; Est. Time [s] 8; Elapsed Time [s] 2
Im.: 35; Proc. Im. #: 10; # Rasterp.:15; Est. Time [s] 8; Elapsed Time [s] 2

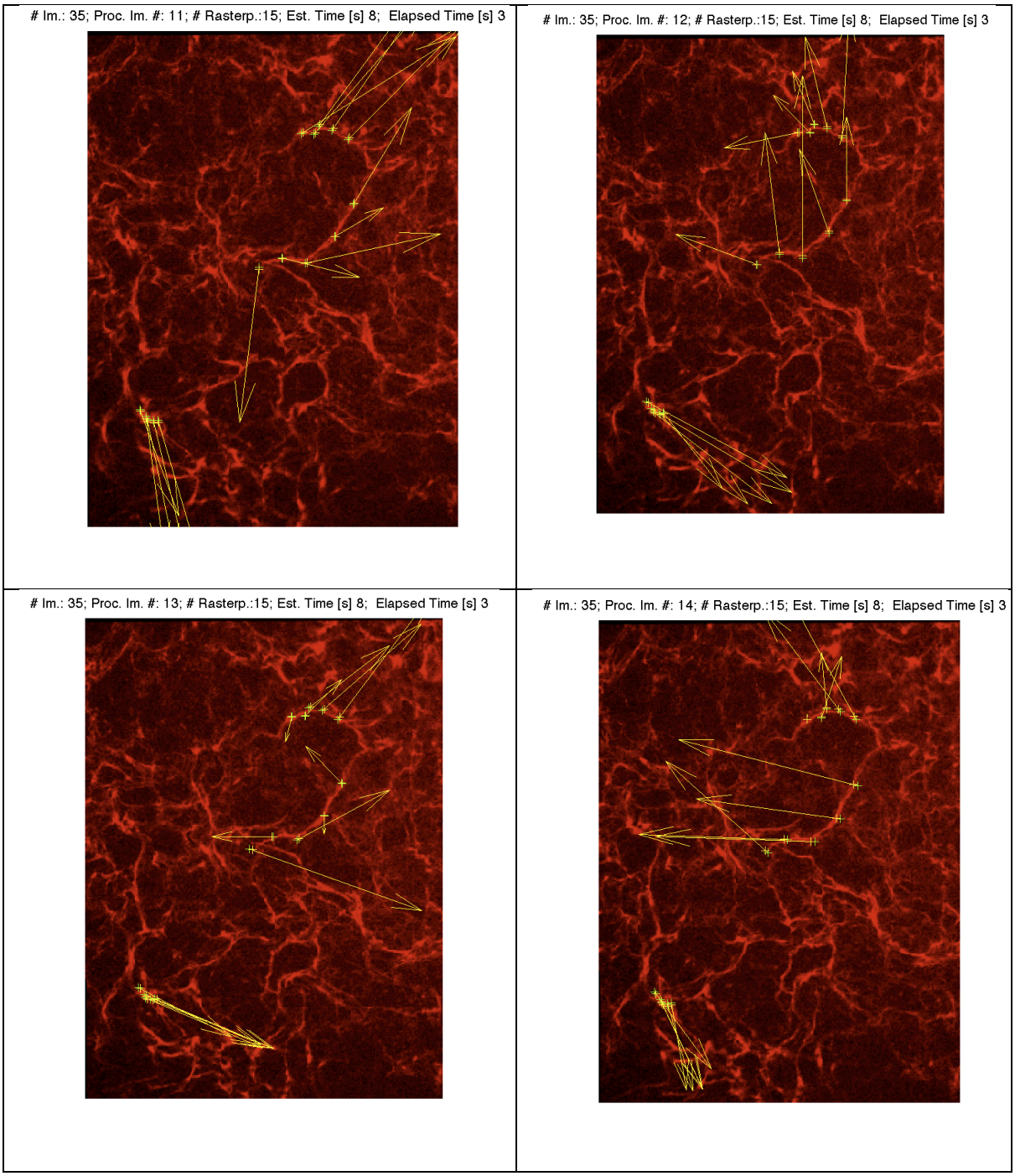
Im.: 35; Proc. Im. #: 11; # Rasterp.:15; Est. Time [s] 8; Elapsed Time [s] 3
Im.: 35; Proc. Im. #: 12; # Rasterp.:15; Est. Time [s] 8; Elapsed Time [s] 3
Im.: 35; Proc. Im. #: 13; # Rasterp.:15; Est. Time [s] 8; Elapsed Time [s] 3
Im.: 35; Proc. Im. #: 14; # Rasterp.:15; Est. Time [s] 8; Elapsed Time [s] 3

Im.: 35; Proc. Im. #: 15; # Rasterp.:15; Est. Time [s] 8; Elapsed Time [s] 3

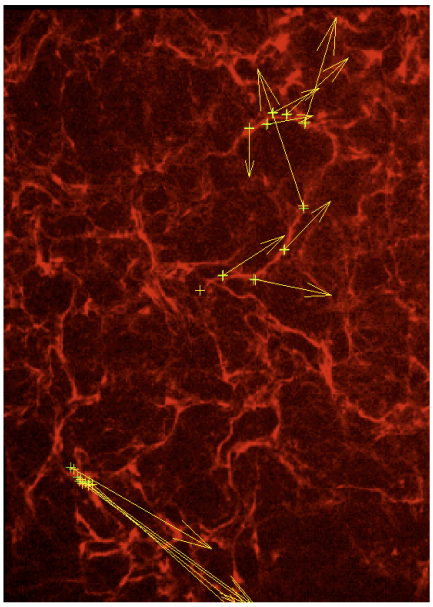

Im.: 35; Proc. Im. #: 16; # Rasterp.:15; Est. Time [s] 8; Elapsed Time [s] 4

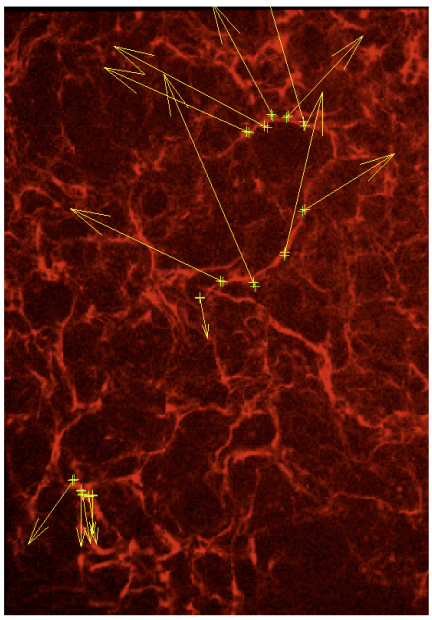

Im.: 35; Proc. Im. #: 17; # Rasterp.:15; Est. Time [s] 8; Elapsed Time [s] 4

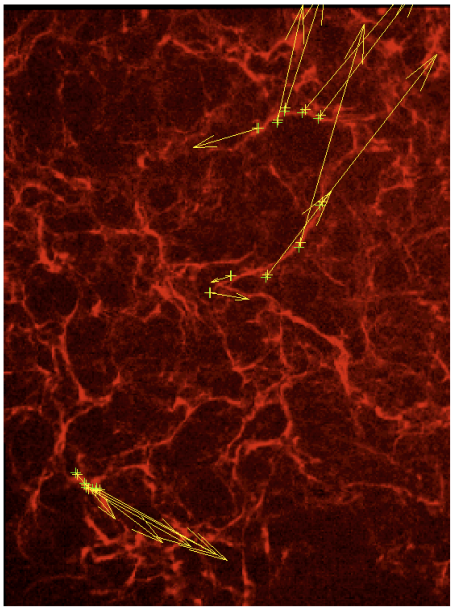

Im.: 35; Proc. Im. #: 18; # Rasterp.:15; Est. Time [s] 8; Elapsed Time [s] 4

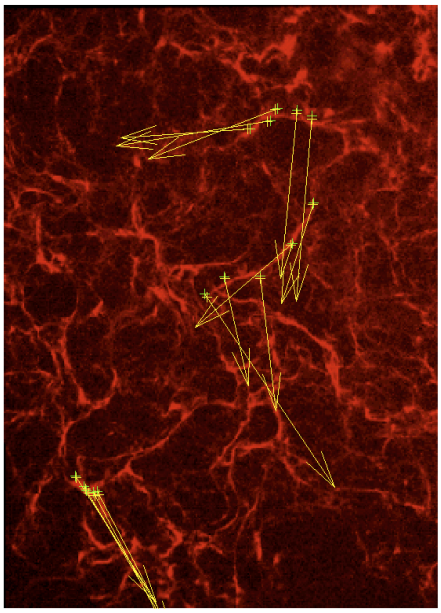

Im.: 35; Proc. Im. #: 19; # Rasterp.:15; Est. Time [s] 8; Elapsed Time [s] 4

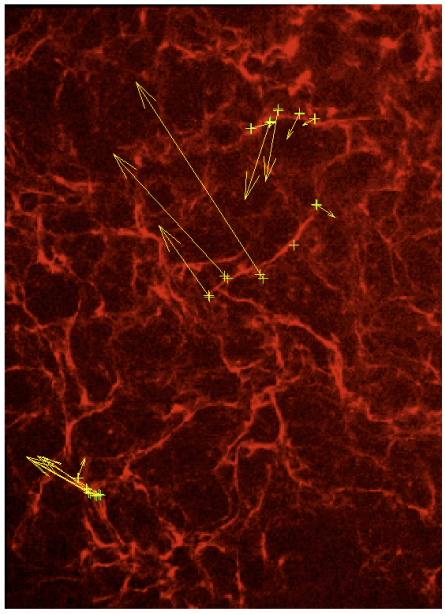

Im.: 35; Proc. Im. #: 20; # Rasterp.:15; Est. Time [s] 8; Elapsed Time [s] 5

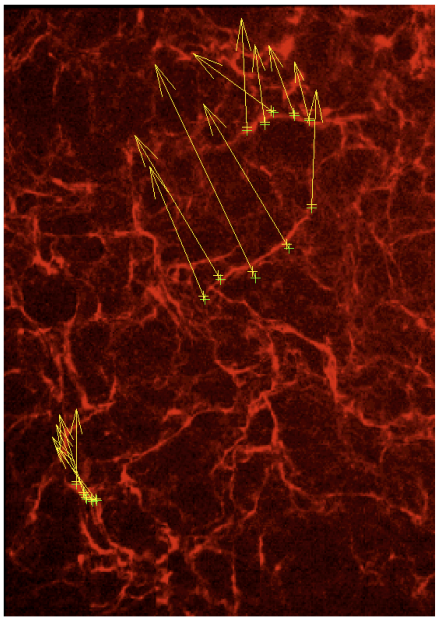

Im.: 35; Proc. Im. #: 21; # Rasterp.:15; Est. Time [s] 8; Elapsed Time [s] 5

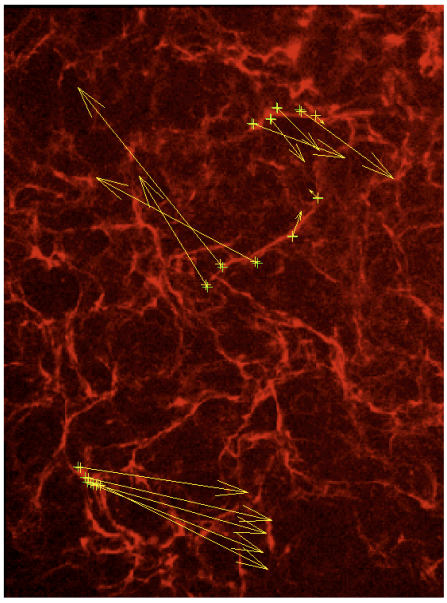

Im.: 35; Proc. Im. #: 22; # Rasterp.:15; Est. Time [s] 8; Elapsed Time [s] 5

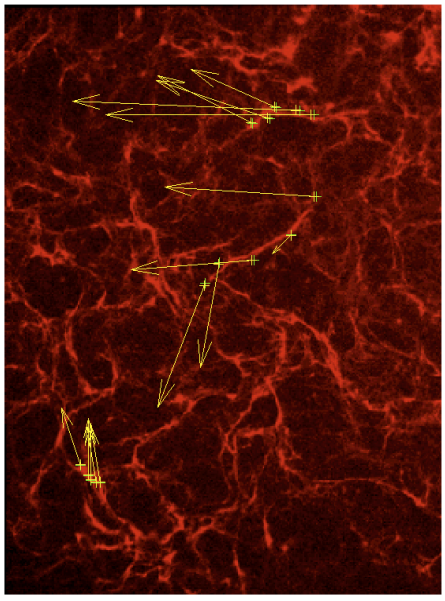

Im.: 35; Proc. Im. #: 23; # Rasterp.:15; Est. Time [s] 8; Elapsed Time [s] 5

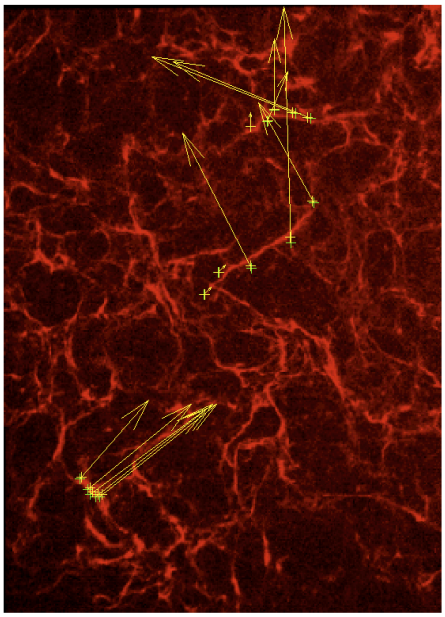

Im.: 35; Proc. Im. #: 24; # Rasterp.:15; Est. Time [s] 8; Elapsed Time [s] 6

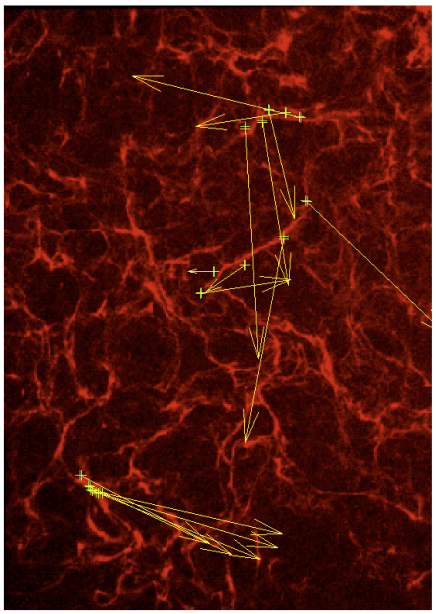

Im.: 35; Proc. Im. #: 25; # Rasterp.:15; Est. Time [s] 8; Elapsed Time [s] 6

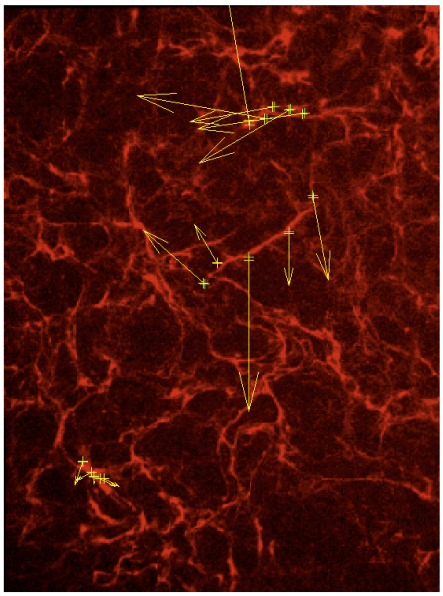

Im.: 35; Proc. Im. #: 26; # Rasterp.:15; Est. Time [s] 8; Elapsed Time [s] 6

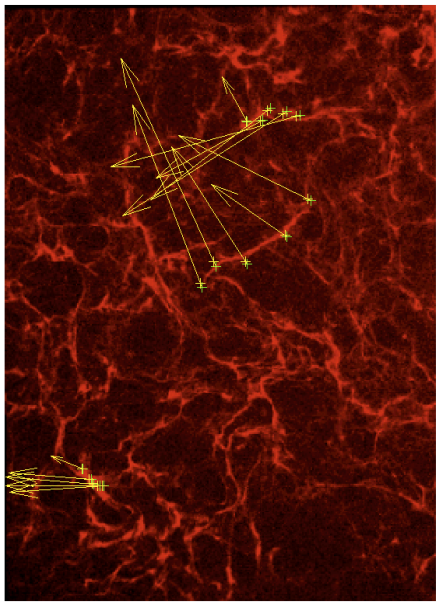

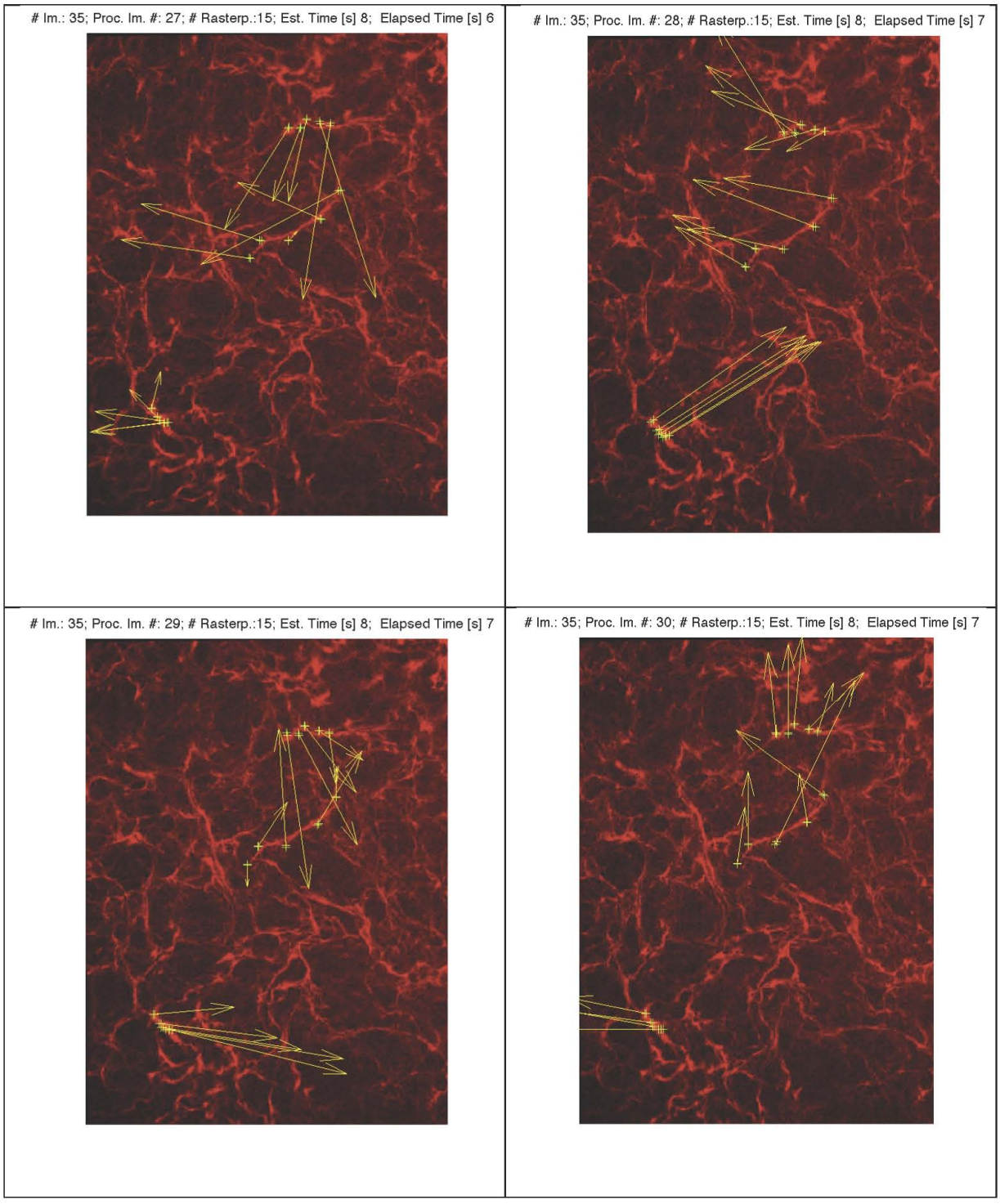
Im.: 35; Proc. Im. #: 27; # Rasterp.:15; Est. Time [s] 8; Elapsed Time [s] 6
Im.: 35; Proc. Im. #: 28; # Rasterp.:15; Est. Time [s] 8; Elapsed Time [s] 7
Im.: 35; Proc. Im. #: 29; # Rasterp.:15; Est. Time [s] 8; Elapsed Time [s] 7
Im.: 35; Proc. Im. #: 30; # Rasterp.:15; Est. Time [s] 8; Elapsed Time [s] 7

Im.: 35; Proc. Im. #: 31; # Rasterp.:15; Est. Time [s] 8; Elapsed Time [s] 7

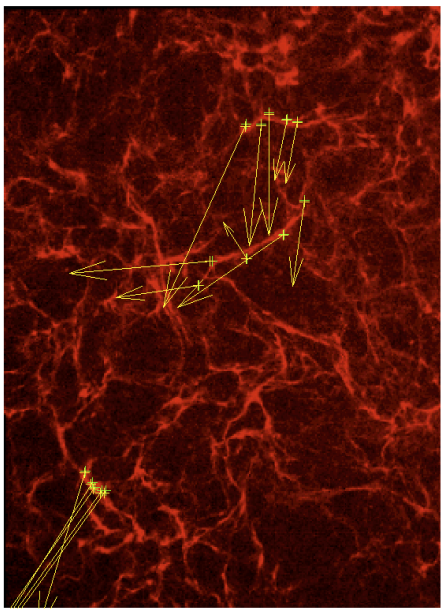

Im.: 35; Proc. Im. #: 32; # Rasterp.:15; Est. Time [s] 8; Elapsed Time [s] 7

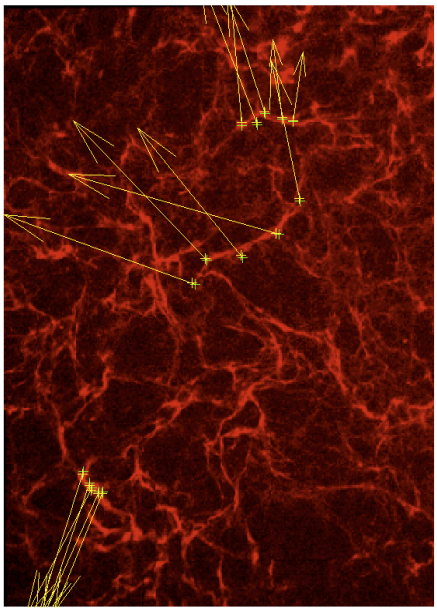

Im.: 35; Proc. Im. #: 33; # Rasterp.:15; Est. Time [s] 8; Elapsed Time [s] 8

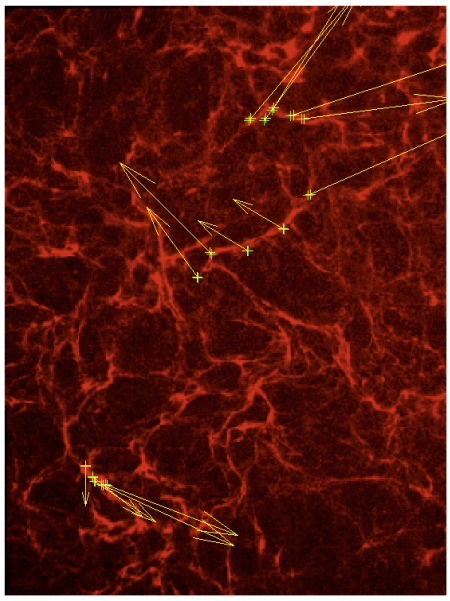

Im.: 35; Proc. Im. #: 34; # Rasterp.:15; Est. Time [s] 8; Elapsed Time [s] 8

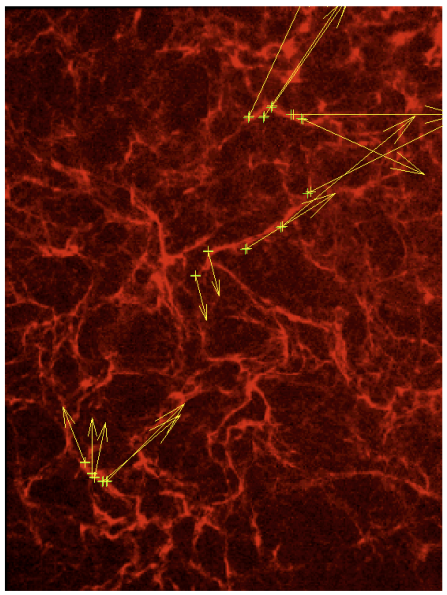

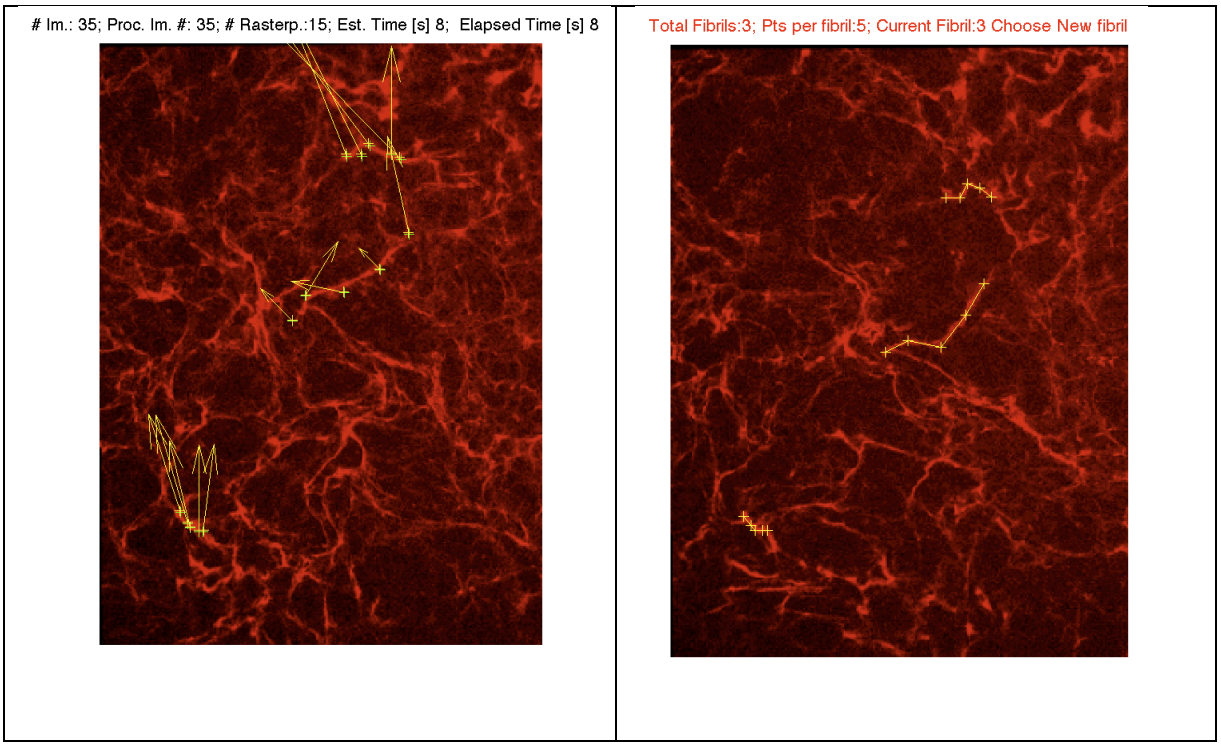

Figure 3.32: The image stack obtained after the execution of automate_image_1.m for images 72-108.

3.6.6 Length and Strain Graphs for Images 72-108

Figures 3.33 to 3.41 depict the graphical representations of the lengths and the strains of the 3 fibrils obtained through the automated DIC analysis in Matlab. The values shown in this graph were obtained from the execution of '*workspline.m*' during which the strain and the total length values are calculated and stored in a folder called '*Sqr_Strain*' as per the fibril they pertain to.

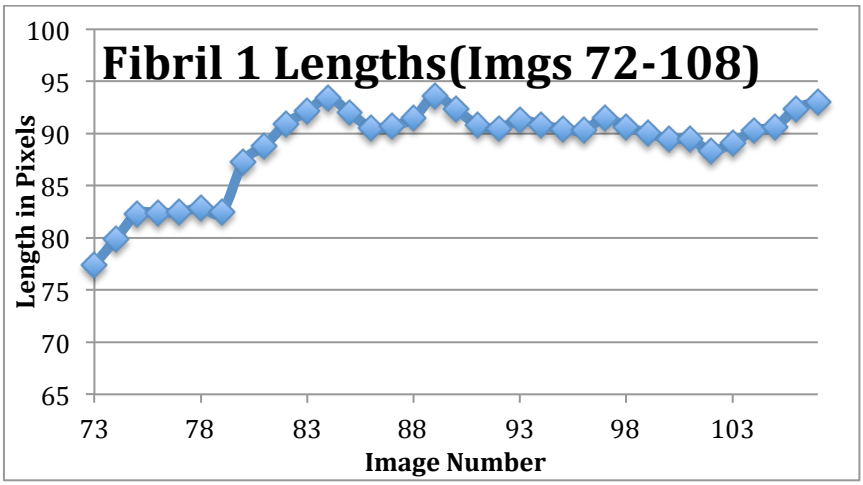

Figure 3.33: A graph depicting the pattern of variation in length of fibril 1

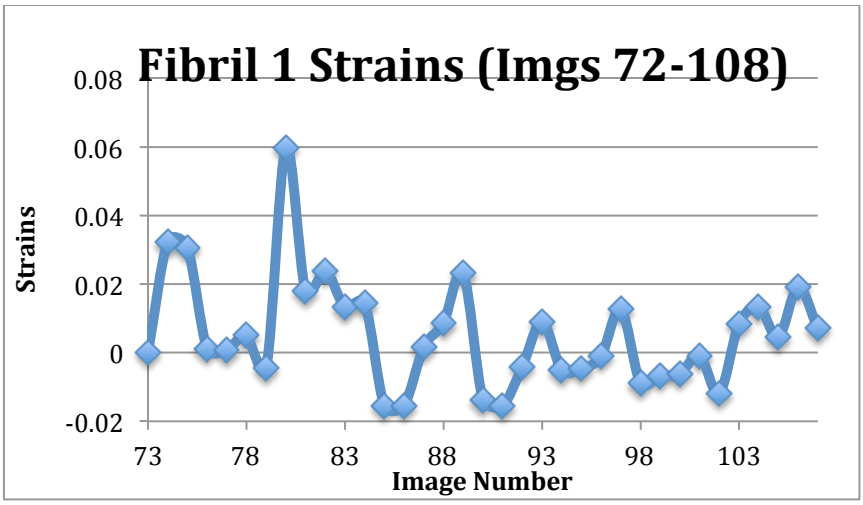

Figure 3.34: A graph depicting the pattern of variation in strains of fibril 1

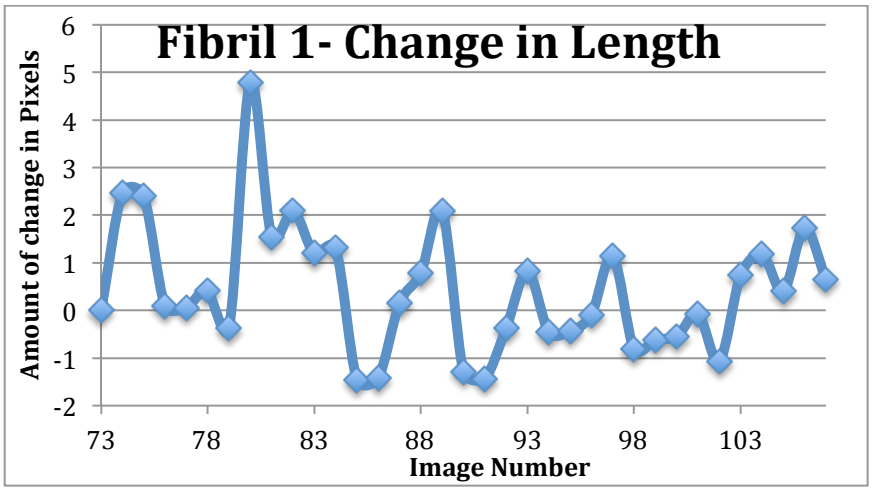

Figure 3.35: A graph depicting the amount of variation in length of fibril 1

The data obtained from the analysis of fibril 1 during the third 12-hour segment shows that the maximal tensile strain experienced by the fibril was 0.0598 at image number 80 and the maximal compressive strain was -0.0155 at image number 85. The average strain was calculated to be 0.0057.

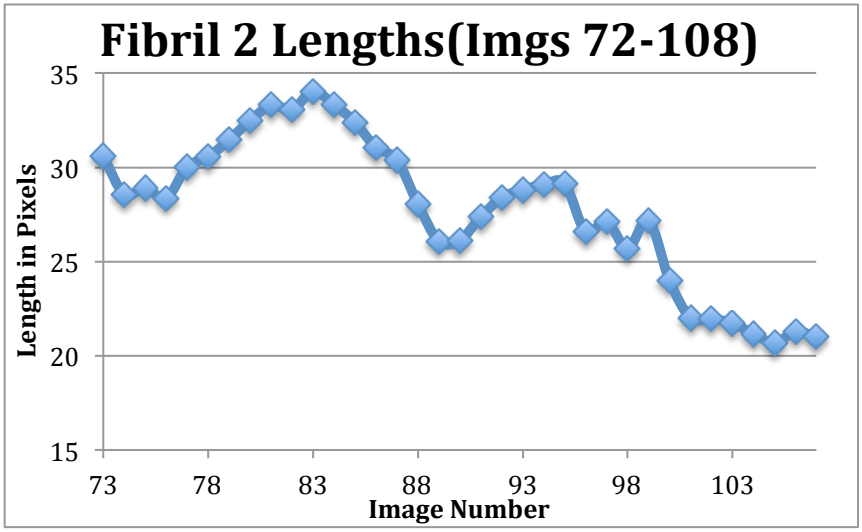

Figure 3.36: A graph depicting the pattern of variation in length of fibril 2

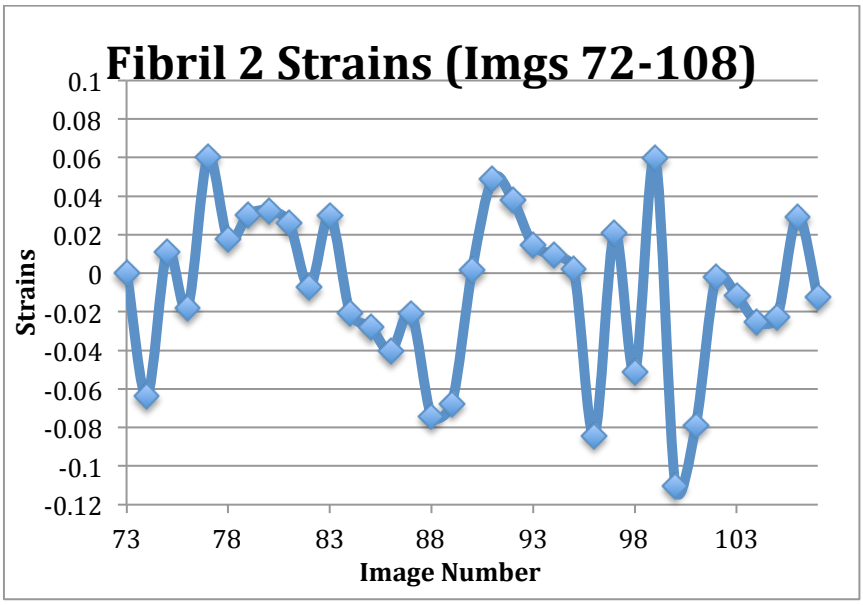

Figure 3.37: A graph depicting the pattern of variation in strains of fibril 2

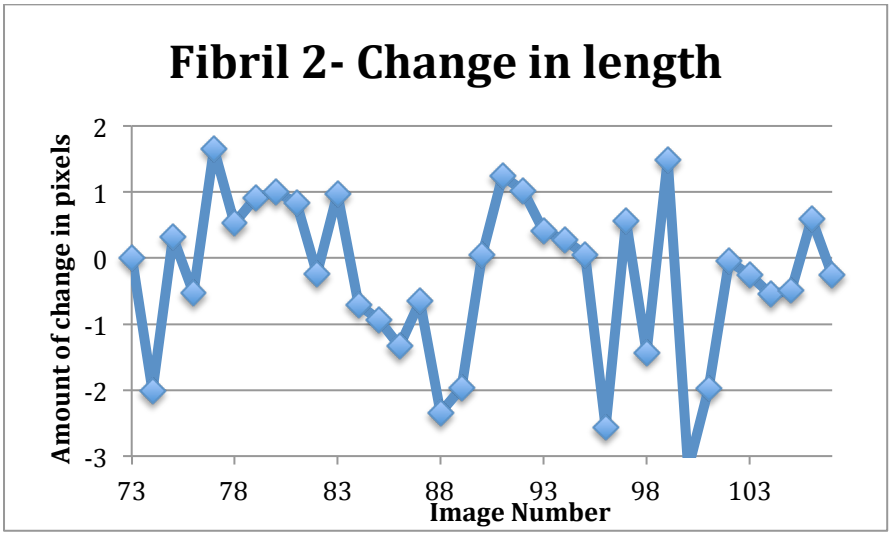

Figure 3.38: A graph depicting the amount of variation in length of fibril 2

The data obtained from the analysis of fibril 2 shows that the maximal positive strain value experienced by the fibril was 0.06 at image number 77 and the maximal negative strain value experienced was -0.1105. The average strain value was calculated as -0.009.

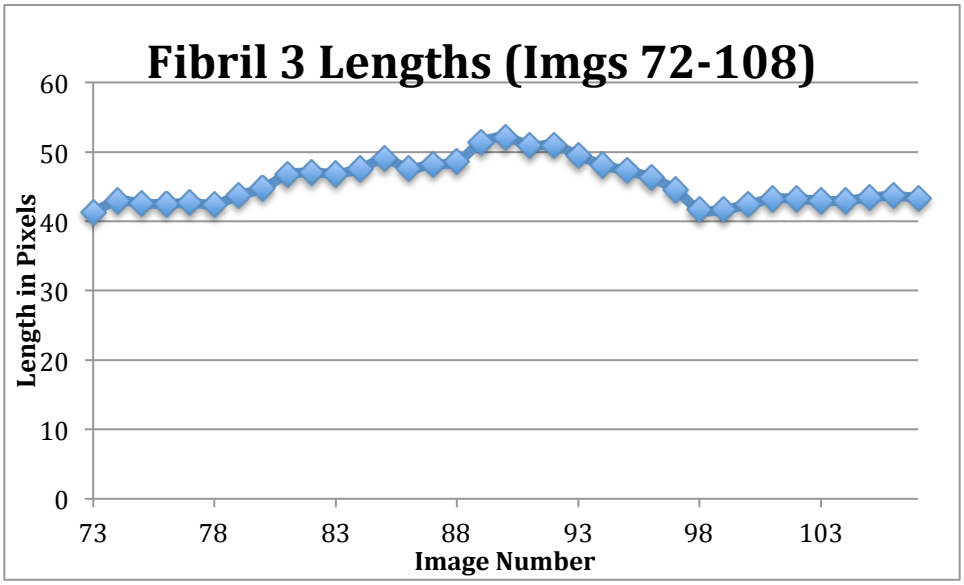

Figure 3.39: A graph depicting the pattern of variation in lengths of fibril 3

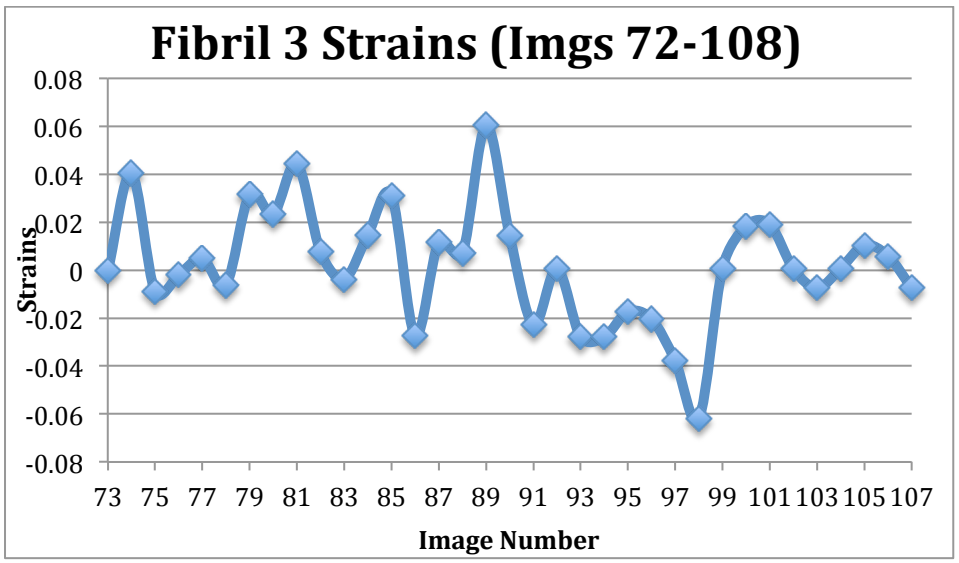

Figure 3.40: A graph depicting the pattern of variation in strains of fibril 3

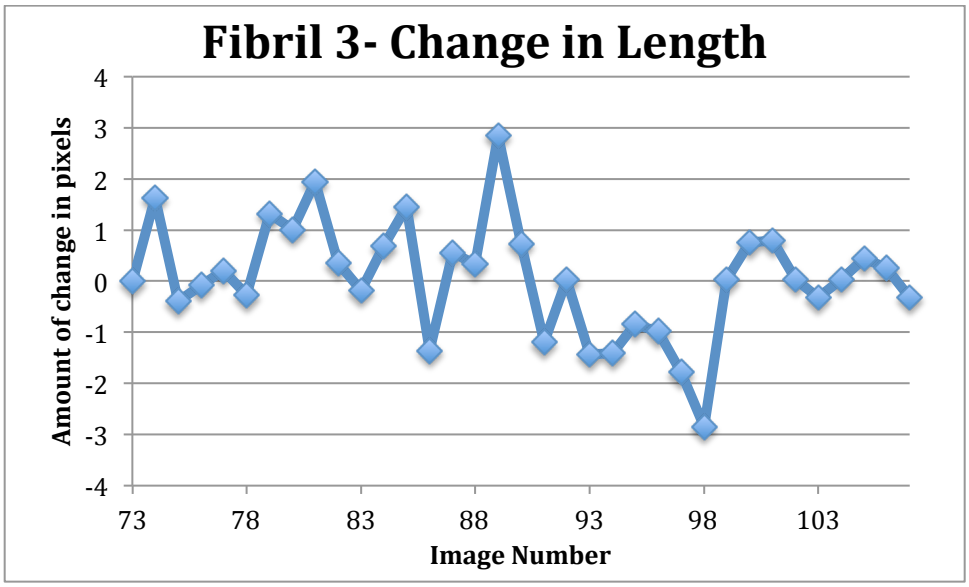

Figure 3.41: A graph depicting the amount of variation in length of fibril 3

The data obtained from the analysis of fibril 3 shows that the maximal tensile strain experienced was 0.0603 at image number 89 and the maximal compressive strain was -0.0619 at image number 98. The average strain value was calculated to be 0.002.

This analysis again shows that each individual fibril shows its own unique pattern of deformation over time and that the fibrils were subjected to both compressive and tensile strains. Furthermore, the raster points on an individual fibril did not necessarily all move in the same direction, at a given time point, suggesting that different regions of the fibril can be deformed in different directions by the underlying cell motions. These findings are similar to what was observed for the last 12 hours of the experiment (refer to section 3.6.1). Comparison of the maximal tensile strains and maximal compressive strains of hours 24-36 and 36-48 show that the variation in the strain values between any two consecutive images is much higher in the third 12 hour segment than in the last 12 hour segment. This suggests that there is a lot more cell motion during the third 12-hour segment in comparison to the last 12-hour segment.

3.6.7 Analysis of Images 108-144 with 20 fibrils

This technique was further used to analyze the behavior of 20 fibrils in the last 12h segment of the movie (36-48h, i.e. images 108-144), in order to quantify the fibril dynamics of a larger sampling of fibronectin fibrils. This larger sample size helps provide a better analysis of overall fibronectin fibril motion and a better indication of how effective the algorithm will be for its final application. Below is the sequence of images obtained after the execution of automate_image.m.

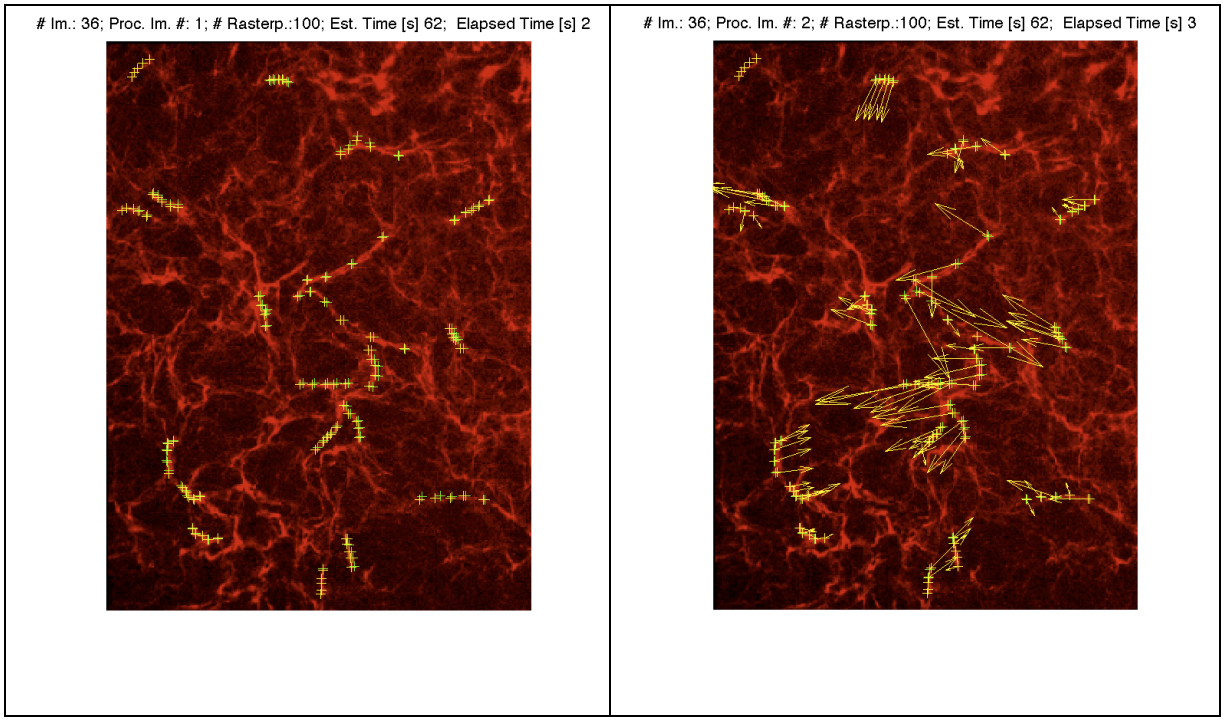

Im.: 36; Proc. Im. #: 3; # Rasterp.:100; Est. Time [s] 50; Elapsed Time [s] 4

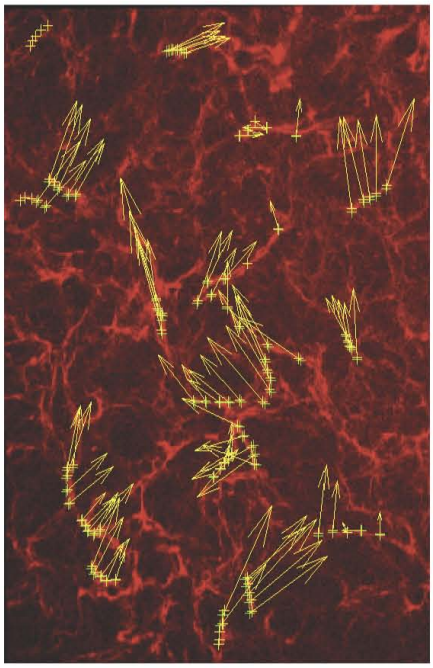

Im.: 36; Proc. Im. #: 4; # Rasterp.:100; Est. Time [s] 43; Elapsed Time [s] 5

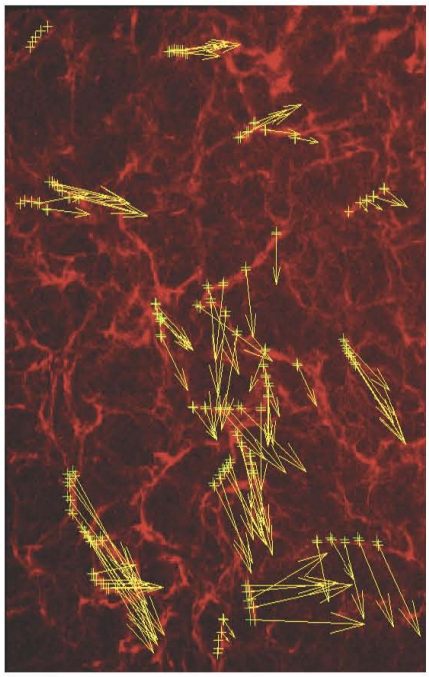

Im.: 36; Proc. Im. #: 5; # Rasterp.:100; Est. Time [s] 38; Elapsed Time [s] 5

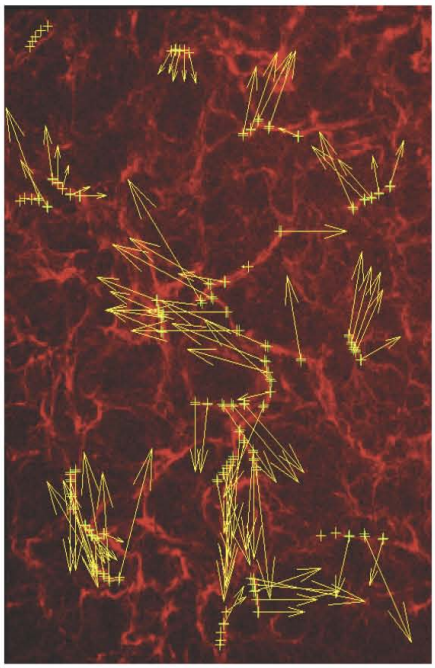

Im.: 36; Proc. Im. #: 6; # Rasterp.:100; Est. Time [s] 35; Elapsed Time [s] 6

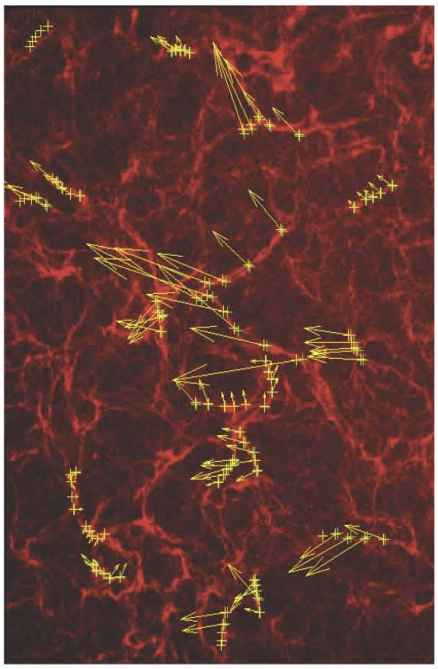

Im.: 36; Proc. Im. #: 7; # Rasterp.:100; Est. Time [s] 34; Elapsed Time [s] 7

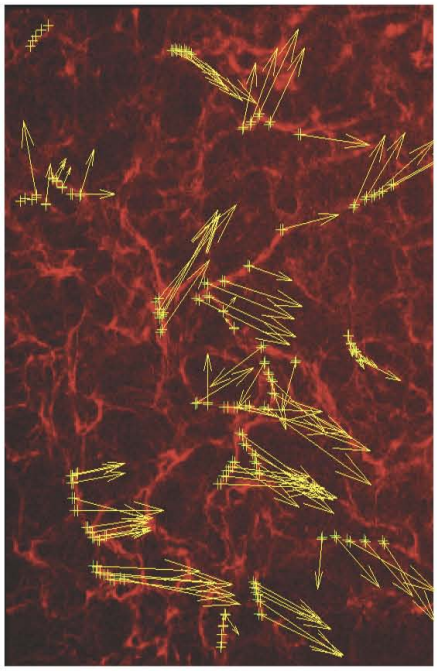

Im.: 36; Proc. Im. #: 8; # Rasterp.:100; Est. Time [s] 33; Elapsed Time [s] 7

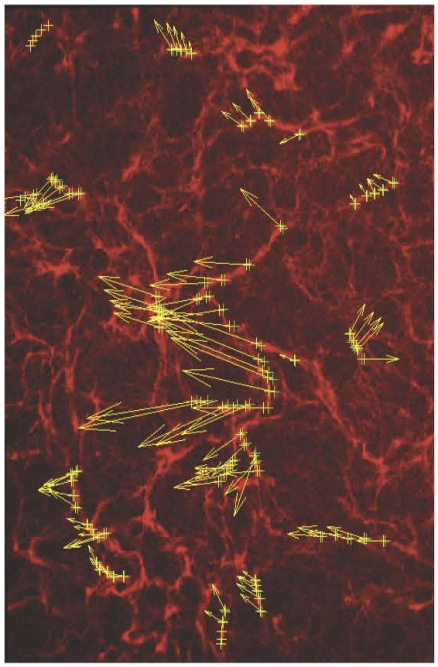

Im.: 36; Proc. Im. #: 9; # Rasterp.:100; Est. Time [s] 31; Elapsed Time [s] 8

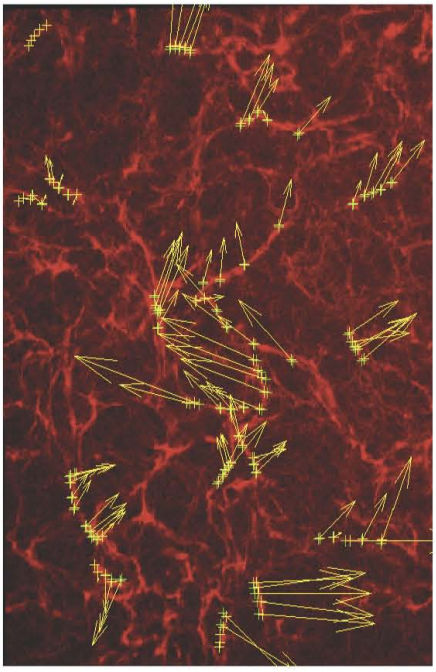

Im.: 36; Proc. Im. #: 10; # Rasterp.:100; Est. Time [s] 30; Elapsed Time [s] 8

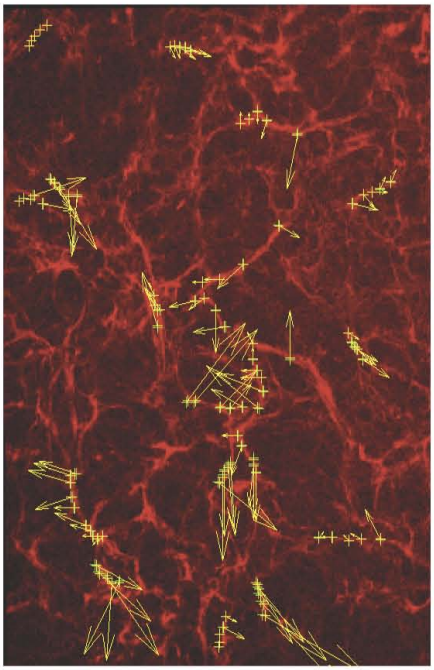

Im.: 36; Proc. Im. #: 11; # Rasterp.:100; Est. Time [s] 29; Elapsed Time [s] 9

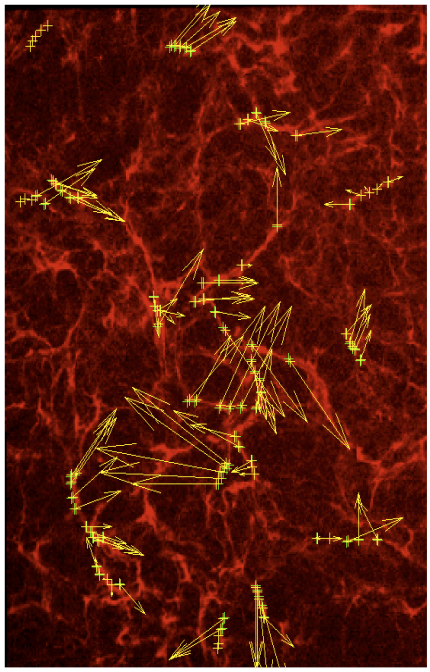

Im.: 36; Proc. Im. #: 12; # Rasterp.:100; Est. Time [s] 29; Elapsed Time [s] 10

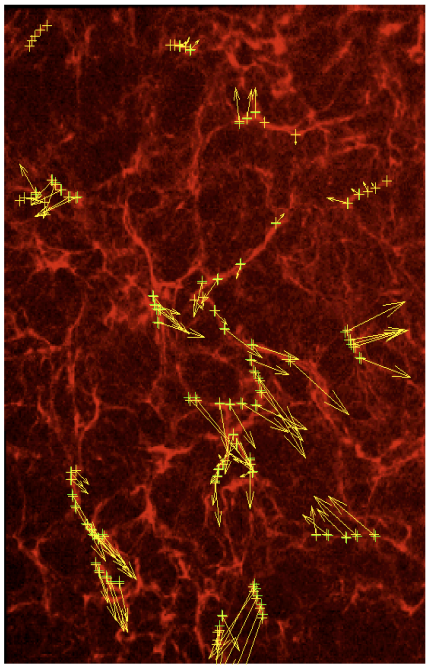

Im.: 36; Proc. Im. #: 13; # Rasterp.:100; Est. Time [s] 28; Elapsed Time [s] 10

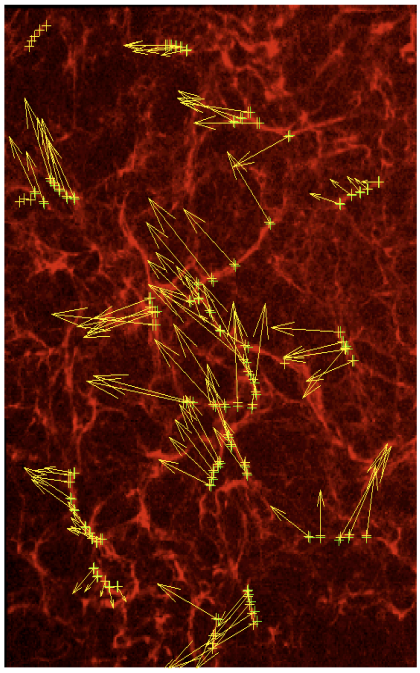

Im.: 36; Proc. Im. #: 14; # Rasterp.:100; Est. Time [s] 28; Elapsed Time [s] 11

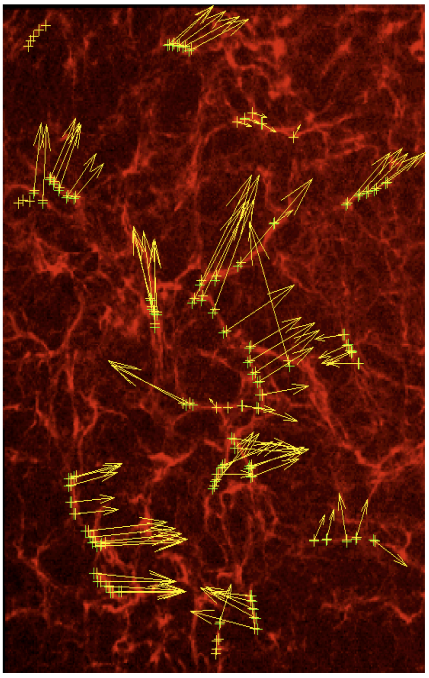

Im.: 36; Proc. Im. #: 15; # Rasterp.:100; Est. Time [s] 27; Elapsed Time [s] 11

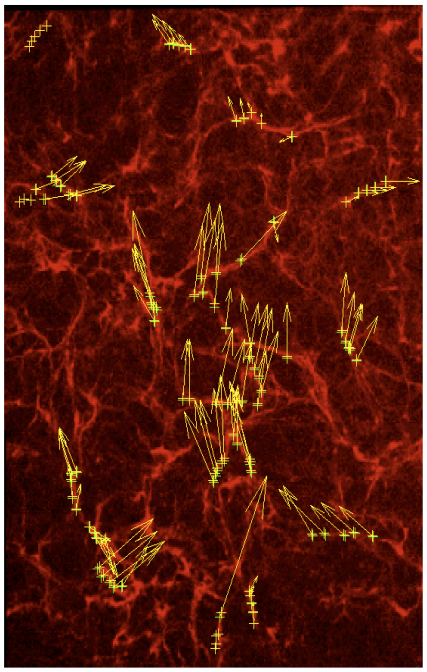

Im.: 36; Proc. Im. #: 16; # Rasterp.:100; Est. Time [s] 27; Elapsed Time [s] 12

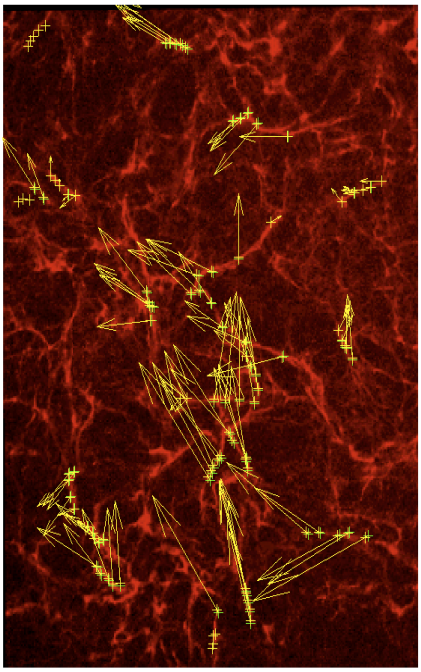

Im.: 36; Proc. Im. #: 17; # Rasterp.:100; Est. Time [s] 27; Elapsed Time [s] 13

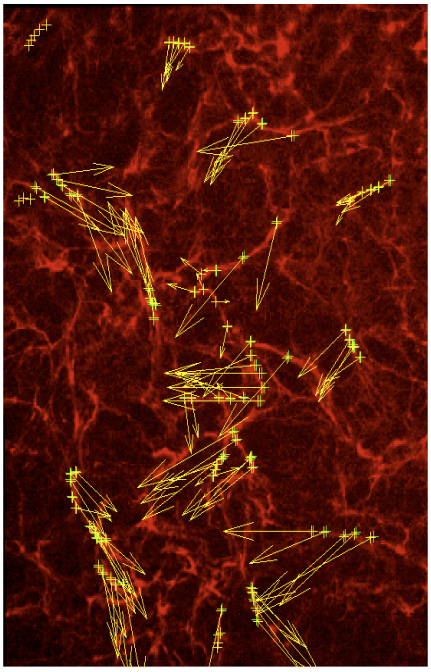

Im.: 36; Proc. Im. #: 18; # Rasterp.:100; Est. Time [s] 26; Elapsed Time [s] 13

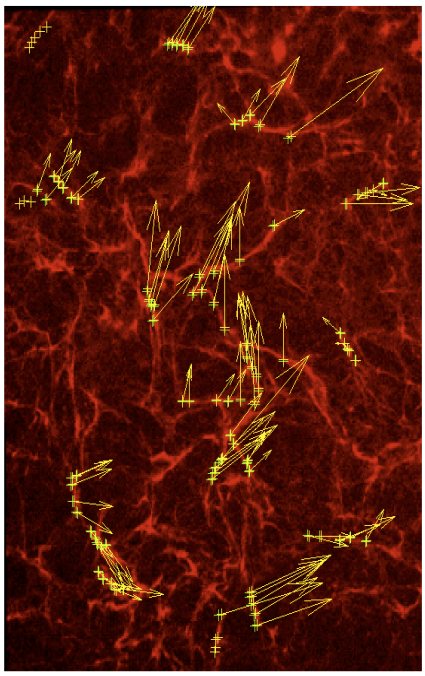

Im.: 36; Proc. Im. #: 19; # Rasterp.:100; Est. Time [s] 26; Elapsed Time [s] 14

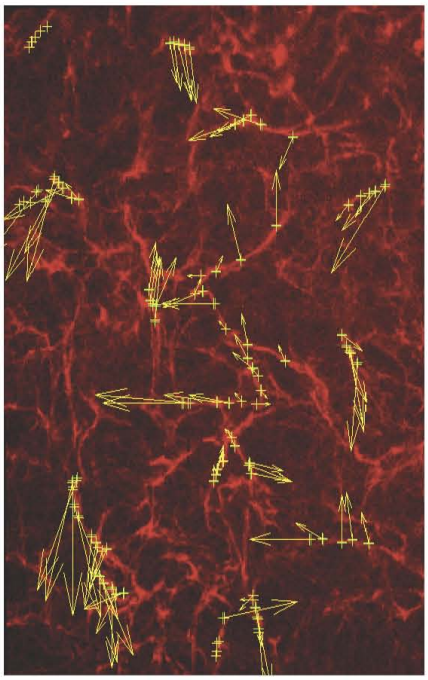

Im.: 36; Proc. Im. #: 20; # Rasterp.:100; Est. Time [s] 26; Elapsed Time [s] 14

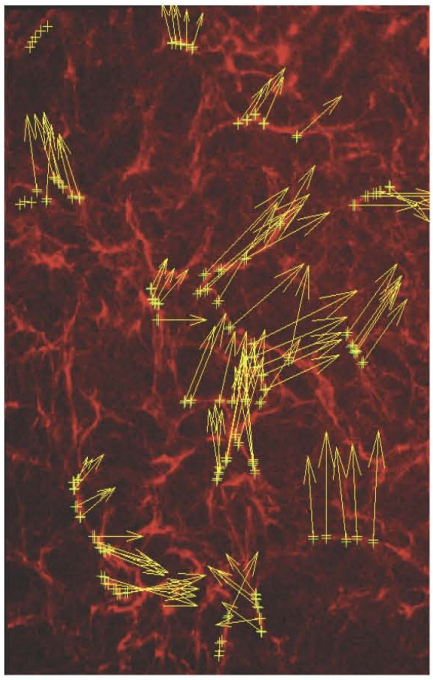

Im.: 36; Proc. Im. #: 21; # Rasterp.:100; Est. Time [s] 26; Elapsed Time [s] 15

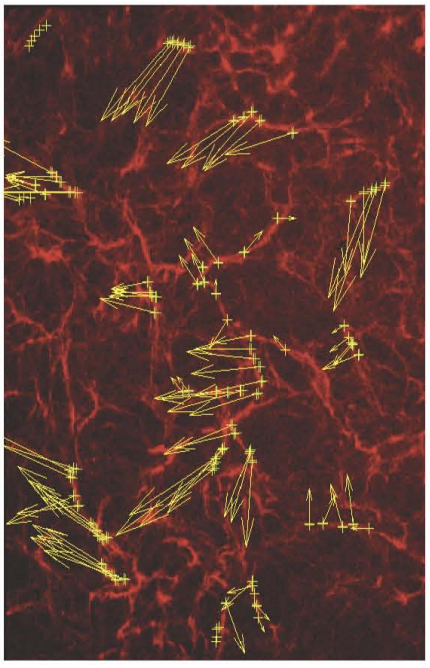

Im.: 36; Proc. Im. #: 22; # Rasterp.:100; Est. Time [s] 25; Elapsed Time [s] 16

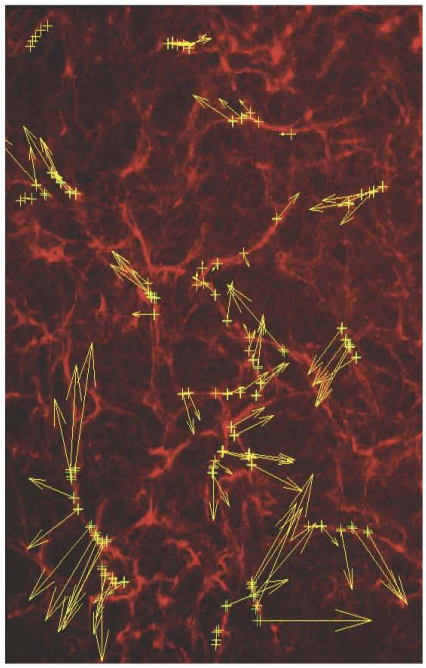

Im.: 36; Proc. Im. #: 23; # Rasterp.:100; Est. Time [s] 25; Elapsed Time [s] 16

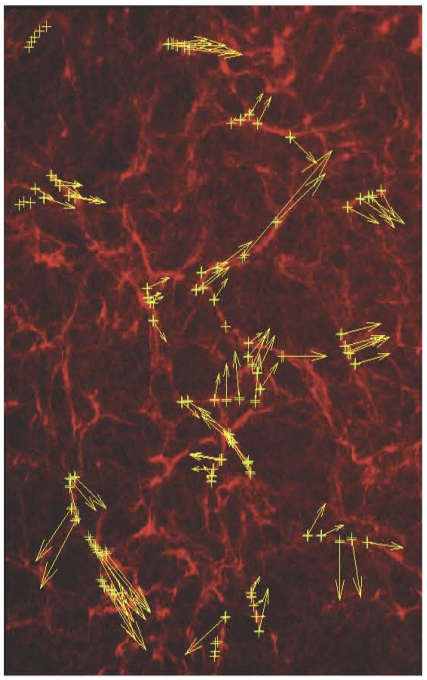

Im.: 36; Proc. Im. #: 24; # Rasterp.:100; Est. Time [s] 25; Elapsed Time [s] 17

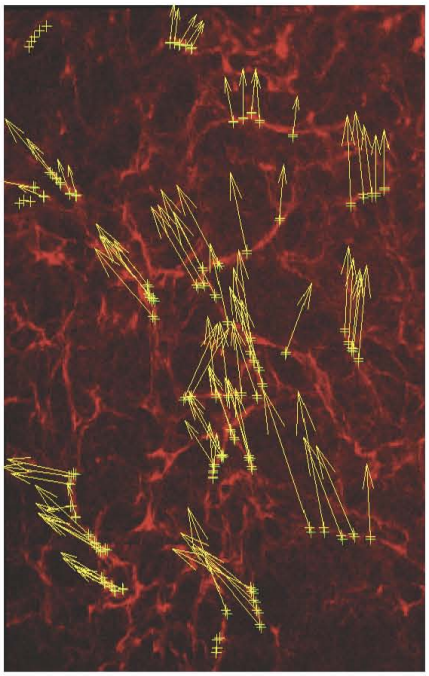

Im.: 36; Proc. Im. #: 25; # Rasterp.:100; Est. Time [s] 25; Elapsed Time [s] 17

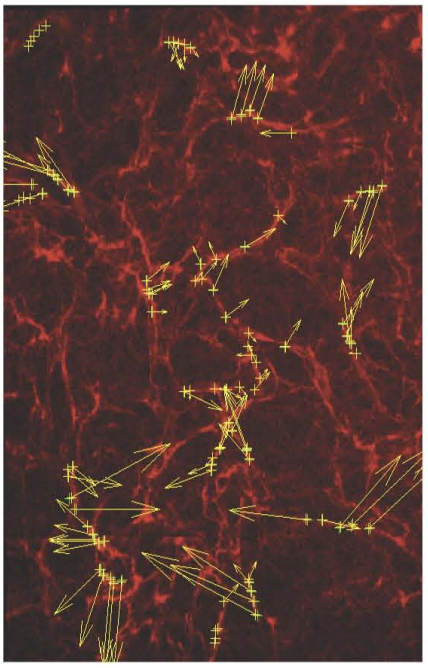

Im.: 36; Proc. Im. #: 26; # Rasterp.:100; Est. Time [s] 25; Elapsed Time [s] 18

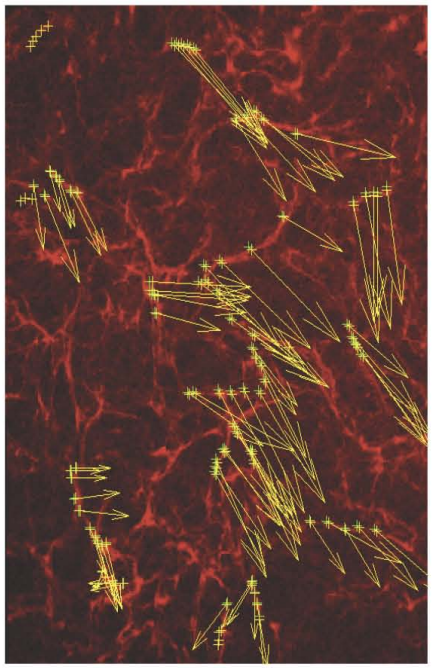

Im.: 36; Proc. Im. #: 27; # Rasterp.:100; Est. Time [s] 25; Elapsed Time [s] 19

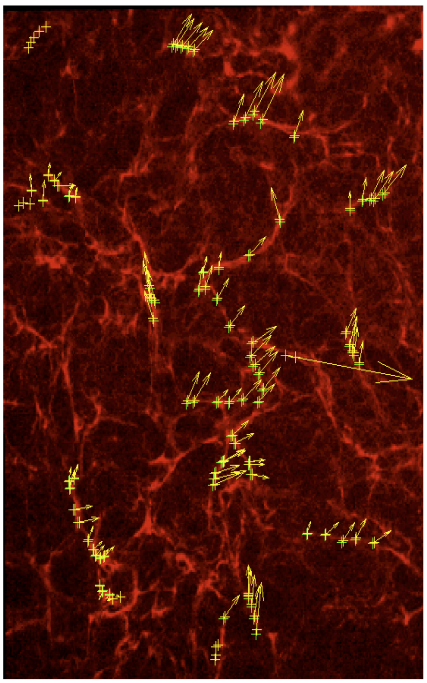

Im.: 36; Proc. Im. #: 28; # Rasterp.:100; Est. Time [s] 25; Elapsed Time [s] 19

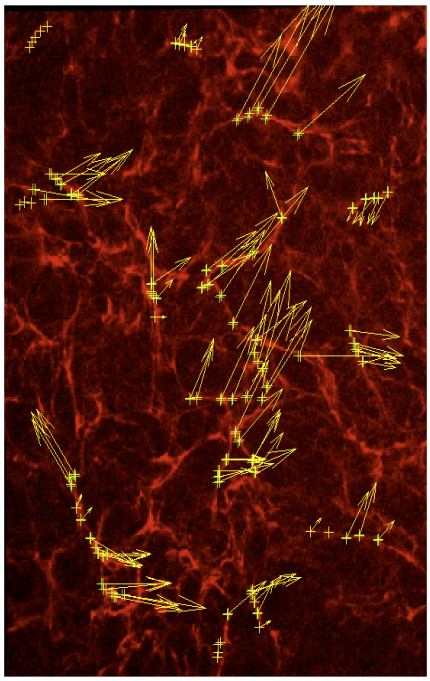

Im.: 36; Proc. Im. #: 29; # Rasterp.:100; Est. Time [s] 25; Elapsed Time [s] 20

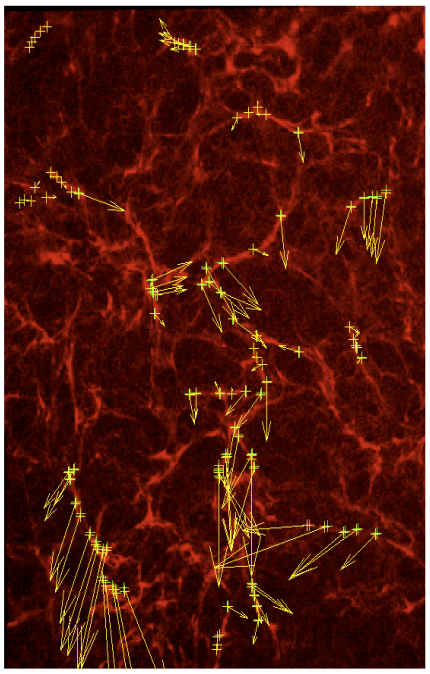

Im.: 36; Proc. Im. #: 30; # Rasterp.:100; Est. Time [s] 24; Elapsed Time [s] 20

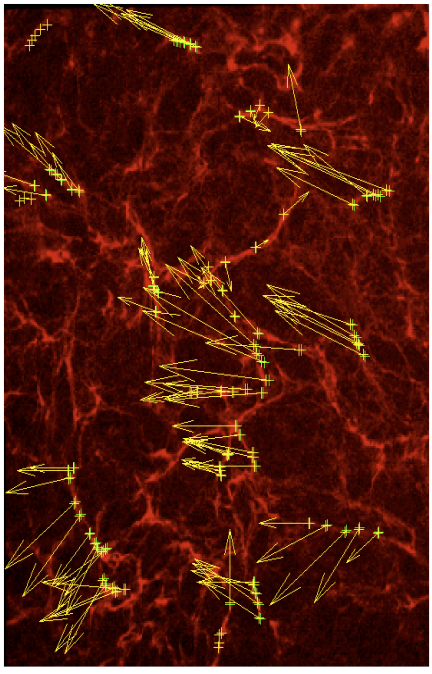

Im.: 36; Proc. Im. #: 31; # Rasterp.:100; Est. Time [s] 24; Elapsed Time [s] 21

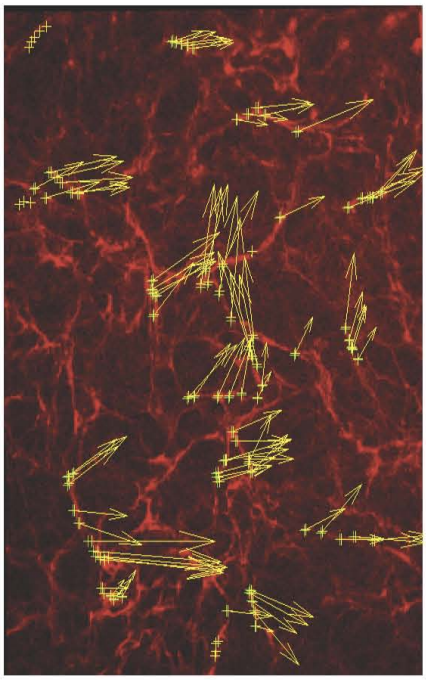

Im.: 36; Proc. Im. #: 32; # Rasterp.:100; Est. Time [s] 24; Elapsed Time [s] 22

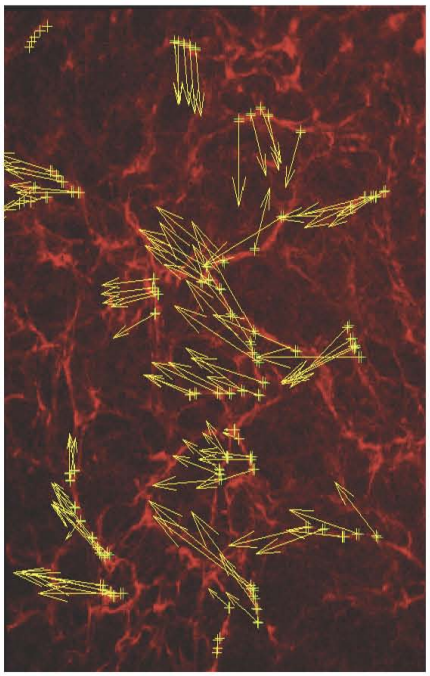

Im.: 36; Proc. Im. #: 33; # Rasterp.:100; Est. Time [s] 24; Elapsed Time [s] 22

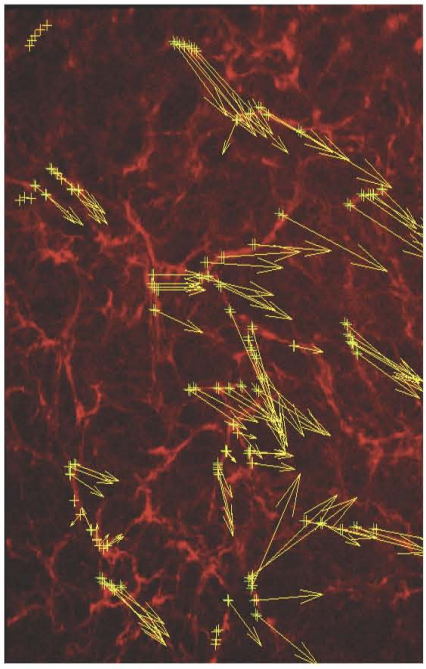

Im.: 36; Proc. Im. #: 34; # Rasterp.:100; Est. Time [s] 24; Elapsed Time [s] 23

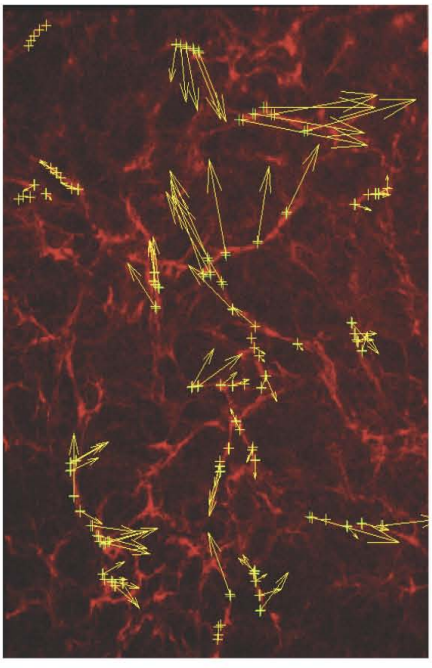

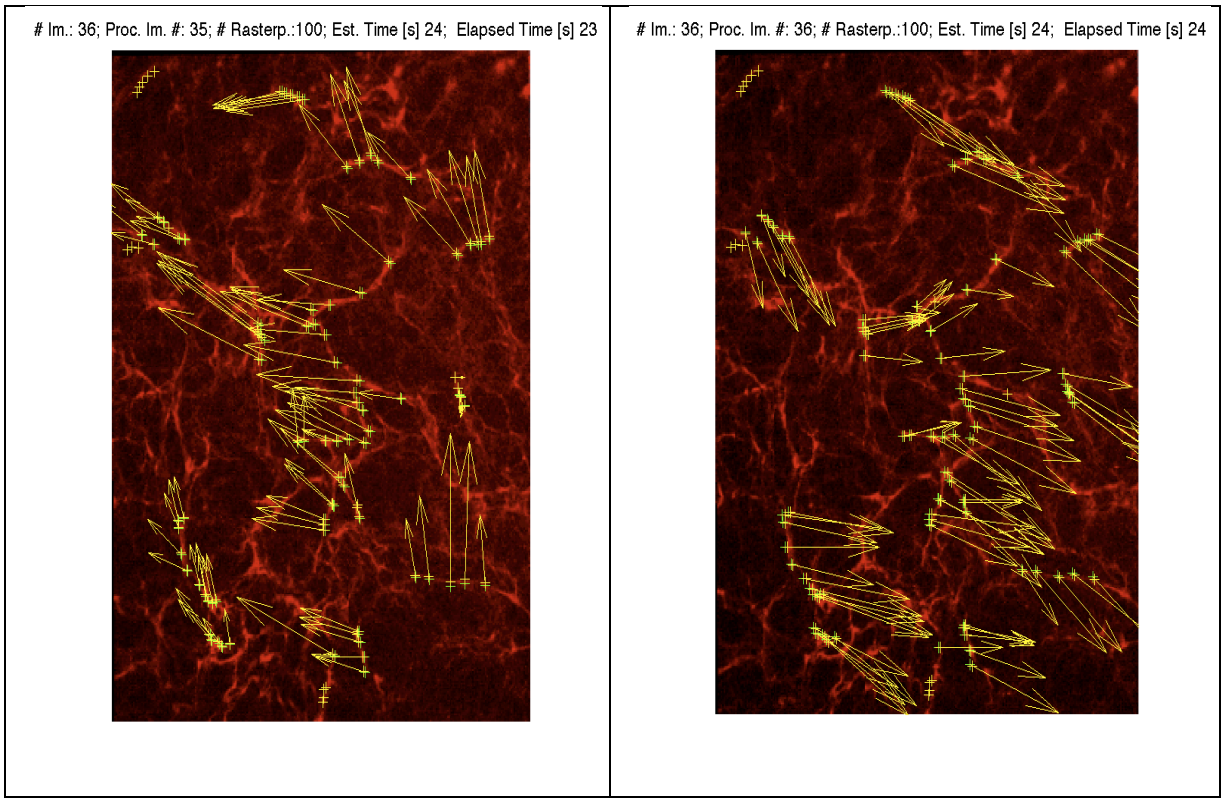

Figure 3.42: The image stack obtained after the execution of automate_image_1.m for images 108-144 analyzing 20 fibrils.

The analysis of 20 fibrils produced similar observations as the previous two analysis of three fibrils, where it was observed that each individual fibril had its own unique pattern of motion and deformation, suggesting that the underlying cell motion was not uniform or unidirectional. Also different parts of an individual fibril experienced motions in different directions causing the fibril to experience both tensile and compressive strains. Figure 3.43 shows the set of graphs depicting the variations in lengths and strains of the 20 fibrils. For ease of comparison all the graphs depicting the lengths have been kept within a constant range of 25 pixels and the graphs depicting the strains have a constant range of -0.18 to 0.36. Based on these results it is observed that each fibril experienced both tensile and compressive

strains. Also the direction and variation of lengths for each fibril seemed non-uniform. It is interesting to note that while a majority of the fibrils showed peak tensile strains in the range +2.8% to +8.5% (+28,000μE to +85,000μE), some individual fibrils showed peak tensile strains as high as +29.9% (+299,000μE). Similarly while the majority of fibrils showed peak compressive strains in the range -3.1% to -8.6% (-31,000μE to -86,000μE), some individual fibrils showed peak compressive strains as high as -17.8% (-178,000μE).

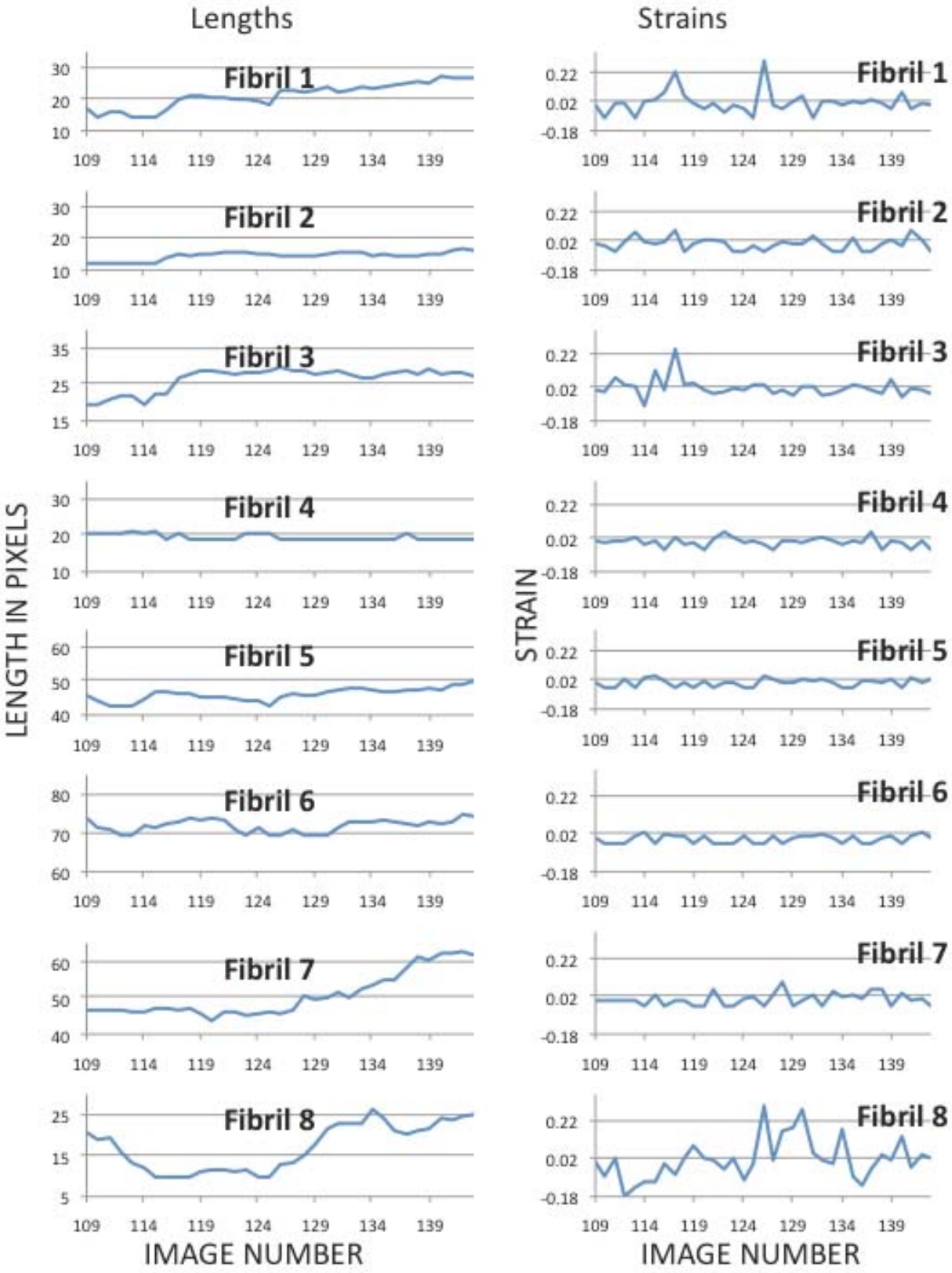
Lengths
Strains
Fibril 1
Fibril 2
Fibril 3
Fibril 4
Fibril 5
Fibril 6
Fibril 7
Fibril 8
LENGTH IN PIXELS
STRAIN
IMAGE NUMBER
IMAGE NUMBER

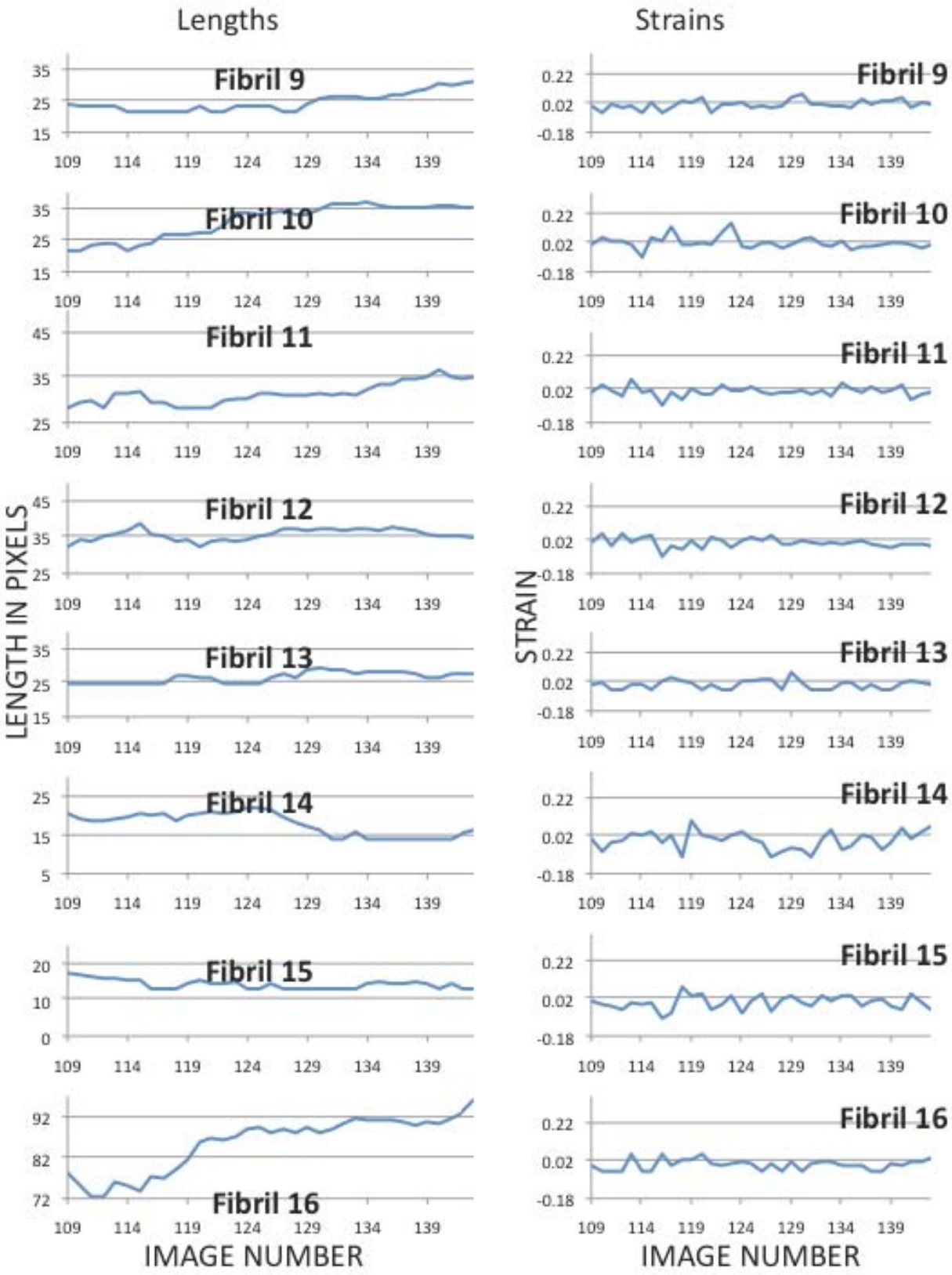
Lengths
Strains
Fibril 9
Fibril 10
Fibril 11
Fibril 12
Fibril 13
Fibril 14
Fibril 15
Fibril 16
LENGTH IN PIXELS
STRAIN
IMAGE NUMBER
IMAGE NUMBER

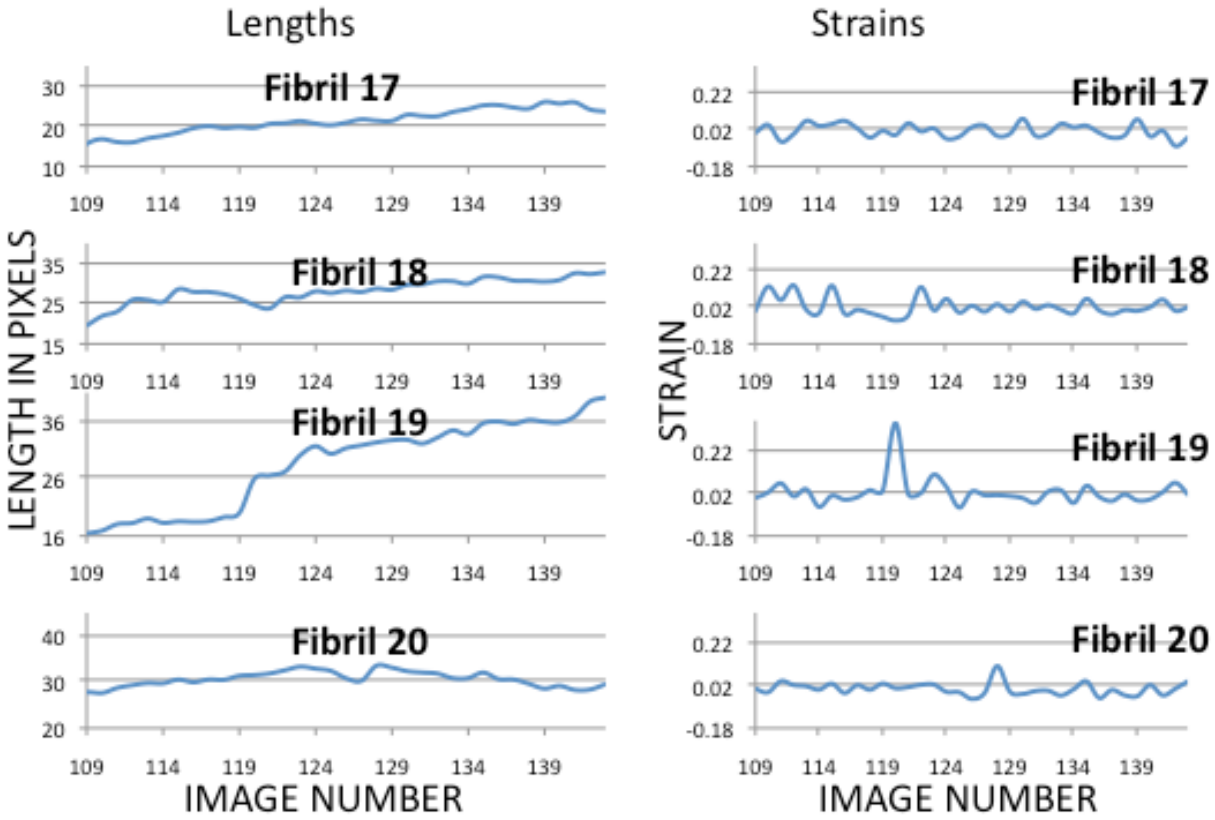

Figure 3.43: A stack of length and strain graphs of 20 fibrils from images 108-144.

Table 3.1, given below, depicts the maximum tensile strains, maximum compressive strains and the average strains experienced by each fibril.

Table 3.1: Maximum Tensile, Compressive and the Average Strains of 20 fibrils

FIBRIL NUMBER	AVERAGE LENGTH	MAXIMUM TENSILE STRAIN	MAXIMUM COMPRESSIVE STRAIN	AVERAGE STRAIN
1	21.152	0.297418	-0.092146	0.017795
2	14.69	0.092284	-0.053656	0.008027
3	26.602	0.246921	-0.090782	0.012322
4	20.115	0.057463	-0.048671	-0.001891
5	46.087	0.047912	-0.032376	0.003020
6	72.167	0.028816	-0.031237	0.000350
7	50.495	0.095966	-0.031600	0.009149
8	17.049	0.299780	-0.178168	0.015961
9	25.082	0.082206	-0.045616	0.007764
10	30.980	0.151595	-0.080271	0.015785
11	31.461	0.077414	-0.076208	0.006929
12	35.656	0.057981	-0.078029	0.00278
13	26.967	0.084794	-0.034477	0.003071
14	18.075	0.098614	-0.091854	-0.004059
15	14.512	0.079272	-0.086309	-0.005905
16	85.624	0.055228	-0.035651	0.00633
17	21.205	0.075844	-0.067953	0.012572
18	28.144	0.134206	-0.060033	0.017143
19	28.555	0.347579	-0.041004	0.029149
20	30.795	0.110091	-0.046002	0.002195

Based on this table, a series of graphs were plotted to analyze the correlation between lengths of the fibrils and the strains experienced by them. Such an analysis would provide

valuable information that may lead to an understanding, and even prediction, of strains a particular fibril might experience solely based on its length. Three such graphs resulted, which are depicted in figures 3.44 to 3.46.

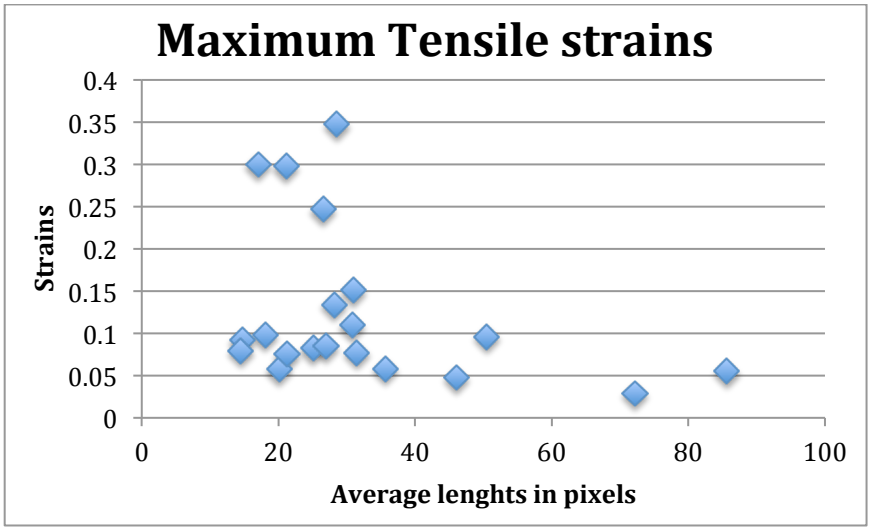

Figure 3.44: A comparison of maximum tensile strains experienced by 20 fibrils as per their average lengths

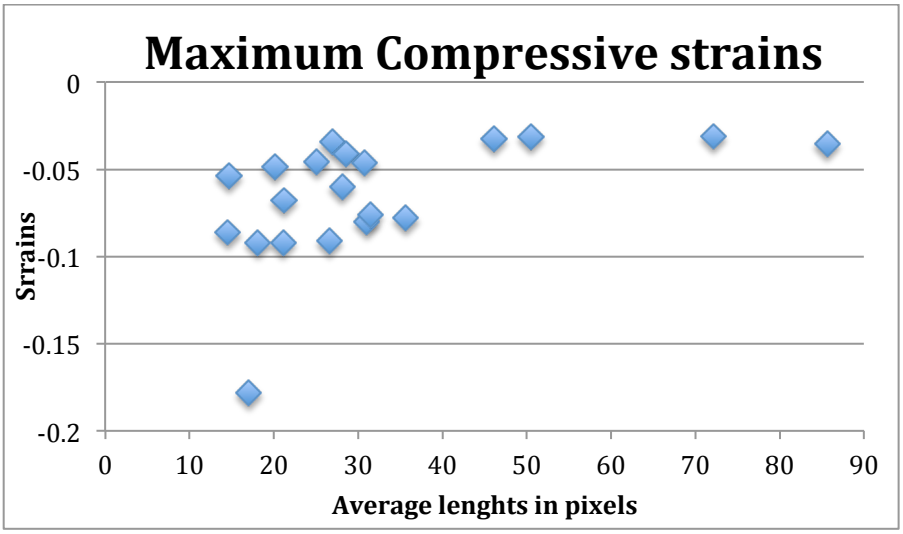

Figure 3.45: A comparison of maximum compressive strains experienced by 20 fibrils as per their average lengths

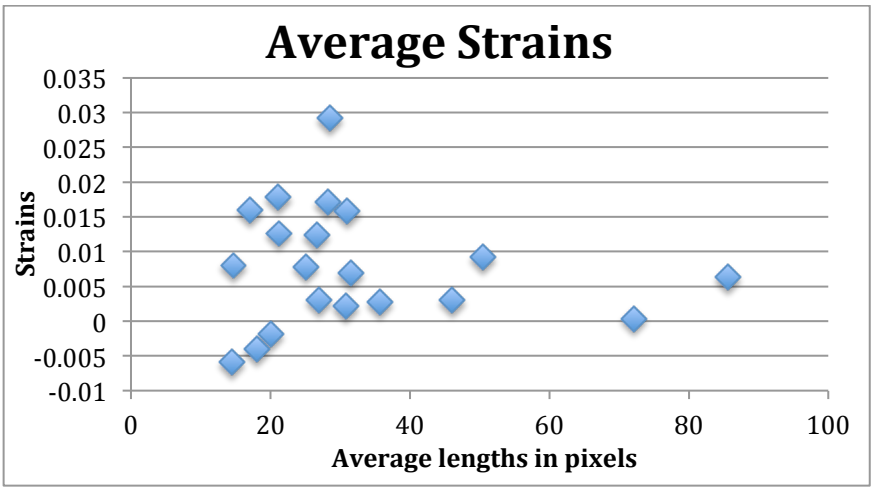

Figure 3.46: A comparison of average strains experienced by 20 fibrils as per their average lengths

The graphs above depict the range of strain values for a particular range of lengths. These are the average lengths of the fibrils calculated over the range of 108-144 images. Figure 3.44 depicts the maximum values of the tensile strains of all the 20 fibrils with their average lengths. Figure 3.45 depicts the maximum values of the compressive strains experienced by all the 20 fibrils along with their average lengths. Figure 3.46 depicts the total average of all the strains experienced by each of the fibrils through all the images and plots them according to the average lengths of the fibrils. The data in these graphs indicate a similar pattern in the density of all the three strains. The strain values for fibrils with lower lengths seem to range from really low values to really high values, but as the length increases, the upper limit of the range seems to go down. While it is too early to make any definitive statements at this point, the above graphs continue to underscore the dynamicity of the entire process.

CHAPTER 4

CONCLUSION AND FUTURE WORK

The aim of this research was to develop an effective method of processing images to calculate the kinematic vectors acting upon the fibrils. The original program, developed by Eberl et al, was thoroughly evaluated where the advantages of this approach was demonstrated. Extensive modifications were then done to this program to tailor-fit it to our requirements. The final results were verified for precision and the comparison graphs were plotted. The strain values were then analyzed to get a better understanding of the biological activity undergone during the phase of the experiment.

Once the tracking efficacy and precision of the results was verified the algorithm was then used to analyze a set of 20 fibrils and calculate the strains acting upon them through the last 12-hours of the experiment. Based on this analysis it was observed that

- there was a lack of uniformity in the deformation of each fibril thus suggesting that each fibril experiences a unique pattern of deformation.
- the fibrils seemed to be experiencing both tensile and compressive strains.

A study of the tensile strain and compressive strain values experienced by the fibrils suggests that during their assembly, fibronectin fibrils are subjected to strains generated by motile osteoblasts that can be as much as two orders of magnitude higher than strains

measured on bone surfaces during normal activity (typically 0.0025) and an order of magnitude higher than strains at the level of the osteocyte. This mechanical stretching of the ECM fibrils by the cells seem to facilitate matrix assembly by exposing cryptic binding sites for ECM modules. They also seem to alter cell behavior through "shedding" of ECM-bound growth factors.

For future work, the algorithm can be further streamlined and made more efficient. There is also ample room to incorporate additional features to better analyze the images. Some of the features that can be added or modified are described below.

1. During the process of modifying the algorithm it was observed that increasing the number of raster points on a fibril helped improve the tracking efficacy of the algorithm. Thus one very good addition to the process would be the ability to dynamically select raster points as per the length of the fibril, especially when multiple fibrils are being processed. While the algorithm does a good job of tracking the motions of fibrils, the current procedure limits the user to have a fixed number of raster points for all the fibrils being processed at a time, irrespective of their lengths. If large disparities exist between the lengths of the fibrils then it may lead to overlapping of raster points, in the case of smaller fibrils, or an incorrect approximation of the length of the fibril, in the case of larger fibrils, thus providing inaccurate results. This can be eliminated by giving the user the ability to assign the number of raster points for every fibril that needs to be processed, based on their length.

2. Another good modification to the process would be to compress the various functions into one single master program while still maintaining ease of usage. The issues that need to be resolved to effectively combine the functions are
    a. Processing the data from each function and saving the results in a way that is still easily accessible by the user.
    b. Shortening the length of the function while still maintaining ease of modification.
    c. Arranging the function in a suitable manner to provide easy additions to the function.
3. The ability to automatically select all the fibrils in a given image would be the next step in automating the entire process. Since every process has different lighting conditions and color-coding, this step would require the user to manually define a few fibrils. The machine would learn from these definitions and select the rest of the fibrils in the image. One of the most important issues to overcome for this addition to be successful is to compensate for varying lighting conditions throughout a given image. Some images tend be brighter in certain sections (usually the centre) while darker in other sections (usually the edges). This would mean the range of RGB values that help define a fibril from its background also keeps varying.
4. Developing a user friendly GUI (Graphical User Interface) would help the user understand and operate the function better, faster and more effectively.

BIBLIOGRAPHY

Bruck, H. A., McNeill, S. R., Suttons, M. A., & Peters, W. H. (1989). Digital image correlation using Newton-Raphson method of partial differential correction. *Experimental Mechanics* , 261-297.

Czirok, A., Rongish, B. J., & Little, C. D. (2004). Extracellular matrix dynamics during vertebrate axis formation. *Dev. Biol. 268* , 111-122.

Czirok, A., Rupp, P. A., Rongish, B. J., & Little, C. D. (2002). Multi-field 3D scanning light microscopy of early embryogenesi. *J. Microsc. 206* , 209-217.

Czirok, A., Zach, J., Kozel, B. A., Mecham, R. P., Davis, C., E., et al. (2006). Elastic fiber macro-assembly is a hierarchical cell motion-mediated process. *J. Cell. Physiol. 207*, 97-106.

Dallas, S. L., Miyazono, K., Skerry, T. M., Mundy, G. R., & Bonewald, L. F. (1995). Dual role for the latent transforming growth factor-beta binding protein in storage of latent TGF-beta in the extracellular matrix and as a structural matrix protein. *J. Cell Biol.131* , 539-549.

Dallas, S. L., Sivakumar, P., Jones, C. J., Chen, Q., Peters, D. M., Mosher, D. F., et al. (2005). Fibronectin regulates latent transforming growth factor-{beta} (TGF{beta}) by controlling matrix assembly of latent TGF{beta}-binding protein-1. *J. Biol. Chem 280* , 18871-18880.

Eberl, C., Thompson, R., & Gianola, D. S. (2006, September 27). *Digital Image Correlation and Tracking*. Retrieved September 1, 2009, from http://www.mathworks.com/matlabcentral/fileexchange/12413

Eils, R., & Athale, C. (2003). Computational imaging in cell biology. *J. Cell Biol. 161* , 477-481.

Filla, M. B., Czirok, A., Zamir, E. A., Little, C. D., Cheuvront, T. J., & Rongish, B. J. (2004). Dynamic imaging of cell, extracellular matrix, and tissue movements during avian vertebral axis patterning. *Birth Defects Res. C Embryo Today 72*, 267-276.

Ghosh-Choudhury, N., Windle, J. J., Koop, B. A., Harris, M. A., Guerrero, D. L., Wozney, J. M., et al. (1996). Immortalized murine osteoblasts derived from BMP 2-T-antigen expressing transgenic mice. *Endocriniology 137*, 331-339.

Jones, E. A., Baron, M. H., Fraser, S. E., & Dickinson, M. E. (2005). Dynamic in vivo imaging of mammalian hematovascular development using whole embryo culture. *Methods Mol. Med. 105* , 381-394.

Kim, K. C., Yoon, S. Y., Kim, S. M., Chun, H. H., & Lee, I. (2006). An orthogonal-plane PIV technique for the investigations of three-dimensional vortical structures in a turbulent boundary layer flow. *Experiments in Fluids* , 876-883.

Kozel, B. A., Rongish, B. J., Czirok, A., Zach, J., Little, C. D., Davis, E. C., et al. (2006). Elastic fiber formation: A dynamic view of extracellular matrix assembly using times reporters`. *J. Cell. Physiol 207*, 87-96.

Lu, H., & Cary, P. D. (2000). Deformation measurements by digital image correlation: Implementation of a second-order displacement gradient. *Experimental Mechanics* , 393-400.

Ohashi, T., Kiehart, D. P., & Erickson, H. P. (2002). Dual labeling of the fibronectin matrix and actin cytoskeleton with green fluorescent protein variants. *J. Cell Sci. 115*, 1221-1229.

Ohashi, T., Kiehart, D. P., & Erickson, H. P. (1999). Dynamics and elasticity of the fibronectin matrix in living cell culture visualized by fibronectin-green fluorescent protein. *Proc. Natl. Acad. Sci. USA , 96*, 2153-2158.

Oreffo, R. O., Mundy, G. R., Seyedin, S. M., & Bonewald, L. F. (1989). Activation of the bone−derived latent TGF beta complex by isolated osteoclasts. *Biochem. Biophys. Res. Commun. 158* , 817-823.

Pankov, R., Cukierman, E., Katz, B. Z., Matsumoto, K., Lin, D. C., Lin, S., et al. (2000). Integrin dynamics and matrix assembly: tensin- dependent translocation of alpha(5)beta(1) integrins promotes early fibronectin fibrillogenesis. *J. Cell Biol. 148* , 1075-1090.

Peltonen J, Larjava H, Jaakkola S, Gralnick H, Akiyama SK, Yamada SS, Yamada KM, Uitto J. (1989). Localization of integrin receptors for fibronectin, collagen, and laminin in human skin. Variable expression in basal and squamous cell carcinomas. *J Clin Invest. 84(6)* , 1916-1923.

Pereira, M., Rybarczyk, B., Odrljin, T. M., Hocking, D. C., Sottile, J., & Simpson-Haidaris, P. J. (2002). The incorporation of fibrinogen into extracellular matrix is dependent on active assembly of a fibronectin matrix. *J. Cell Sci. 115* , 609-617.

Petroll, W. M., & Ma, L. (2003). Direct, dynamic assessment of cell-matrix interactions inside fibrillar collagen lattices. *Cell Motil. Cytoskeleton 55*, 254-264.

Petroll, W. M., Cavanagh, H. D., & Jester, J. V. (2004). Dynamic three-dimensional visualization of collagen matrix remodeling and cytoskeletal organization in living corneal fibroblasts. *Scanning , 26*, 1-10.

Petroll, W. M., Ma, L., & Jester, J. V. (2003). Direct correlation of collagen matrix deformation with focal adhesion dynamics in living corneal fibroblasts. *J. Cell Sci. 116*, 1481-1491.

Sakai, T. (2003). Video-imaging visualization of blood flow dynamics in early chick embryo. *Jpn. J. Physiol. 53* , 385-388.

Seyedin, S. M., Thompson, A. Y., Bentz, H., Rosen, D. M., McPherson, J. M., Conti, A., et al. (1986). Cartilage−inducing factor−A. Apparent identity to transforming growth factor−beta. *J. Biol. Chem. 261* , 5693–5695.

Sivakumar, P., Czorik, A., Rongish, B. J., Divakara, V. P., Wang, Y.-P., & Dallas, S. L. (2006). New insights into extracellular matrix assembly and reorganization from dynamic imaging of extracellular matrix proteins in living osteoblasts. *Journal of Cell Science 119* , 1350-1360.

Sottile, J., & Hocking, D. C. (2002). Fibronectin polymerization regulates the composition and stability of extracellular matrix fibrils and cell−matrix adhesions. *Mol. Biol. Cell 13* , 3546–3559.

Taipale, J., & Keski−Oja, J. (1997). Growth factors in the extracellular matrix. *FASEB J. 11* , 51-59.

Taipale, J., Miyazono, K., Heldin, C. H., & Keski-Oja, J. (1994). Latent transforming growth factor−beta 1 associates to fibroblast extracellular matrix via latent TGF−beta binding protein. *J. Cell Biol. 124* , 171-181.

Zamir, E. A., Czirók, A., Rongish, B. J., & Little, C. D. (2005, june). A Digital Image-Based Method for Computational Tissue Fate Mapping During Early Avian Morphogenesis. *Annals of Biomedical Engineering* , 854-865.

VITA

Aditya Roshan was born in Hyderabad, India on the 22nd of October 1986. He did his schooling in DAV Public School, Hyderabad and graduated from high school in 2004. He then pursued a degree in Electronics and Instrumentation Engineering at CVR College of Engineering, which is affiliated with Jawaharlal Nehru Technological University, Hyderabad and was awarded a Bachelor of Technology in 2008. He joined the Master of Sciences program at University of Missouri – Kansas City in Spring 2009 and graduated in Fall 2011.

During the course of his education he has worked as an Intern at National Small Industries Corporation (NSIC), Hyderabad and Electronics Corporation of India (ECIL), Hyderabad. He has also worked as a Graduate Research Assistant under Dr.Ganesh Thiagarajan, Department of Civil and mechanical Engineering, on the project titled 'Deformation Mapping of Fibronectin Fibrils using the concept of Digital Image Correlation' which was funded and supervised by Dr.Sarah Dallas, Department of Oral Biology. He has presented a poster on this research at the American Society of Bone and Mineral Research (ASBMR) 2011 held in San Diego.